Ultra-fine dark matter structure in the Solar neighbourhood

Daniele Stefano Maria Fantin

"Scientific knowledge is a body of statements of varying degrees of certainty: some are most unsure, some nearly sure, none absolutely certain."

– R. Feynmann

Supervisors:	Prof. Michael R. Merrifield
	Dr. Anne M. Green
Examiners:	Prof. Alfonso Aragon-Salamanca
	Dr. Ed Daw

Abstract

Dark matter plays a fundamental role in theories of the formation and evolution of galaxies. Thus every attempt to model galaxy formation and evolution has to take into consideration the presence of dark halos. Moreover, mergers and accretion appear to be fundamental driving mechanisms in determining the present day properties of galaxies.

The aim of this thesis is to study the ultra-fine distribution of dark matter in the Solar neighbourhood, and to investigate the implications for the current and next generation of dark matter directional detectors. For this purpose we develop a model for halo mergers in a Milky Way-like galaxy. The signals expected in lab-based dark matter detection experiments depend on the phase-space distribution on sub-milliparsec scales. With our numerical technique it is possible to resolve structures produced by minor mergers of subhalos with a larger parent halo. This type of substructure is inaccessible to conventional N-body simulations. When applied in a cosmological context, this method becomes a powerful instrument to reproduce and analyse the complete multiple merger history of a Milky Way-like system.

The results obtained simulating the Galactic halo suggest that the velocity distribution in the solar neighbourhood after an evolution time corresponding to the lifetime of our galaxy ($\simeq 14\,\mathrm{Gyr}$) is smooth. This result suggests the presence of a huge number of dark matter streams that overlap to form a smooth distribution. Nevertheless, the final velocity distribution has overdensities for all the cases that has been analysed. They are generated by a very large number of merger events, but the current generation of detectors have not the angular resolution required to observe these features. A future generation of detectors with a resolution of $\sim 1^\circ$ would start to resolve them, allowing the merger history of the Galaxy to begin to be unravelled using this diagnostic.

Acknowledgements

“All hope abandon, ye who enter. . . ”

– Inferno, Canto III, vv. 1-9

This is the inscription that Dante Alighieri reads when he passes through the gate of the Inferno (Italian for ”Hell”) in his Divine Comedy. In the poem, the Inferno is divided in nine Circles of suffering. My acknowledgements would like to be the “Nottingham parody” of the Inferno. In this few pages I will be your Dante, and I will describe to you what I have seen in these last four years. I hope that, putting together the pieces (people, animals and objects) of this big puzzle, you’ll understand a bit of my experience here in Nottingham. If you don’t manage. . . read them again and switch on the brain. Before starting our travel, please note that any resemblance to real persons and/or to real events is intentional.

Being a poet, let me say one last thing before starting our journey:

I’ve met many people in these 4 years
and somebody I’ll probably forget,
so if your name is not in here,
well...smile and don’t get too upset!

On the gate of “my” Inferno, the inscription is a bit longer:

All hope abandon, ye who enter, of finding something written in “Queen’s” English,
All hope abandon, ye who enter, of reading something “politically correct”,
All hope abandon, ye who enter, of finding a long, boring list of names.

The first Circle of the Inferno is populated by the supervisors and the collaborators. They are mythological and frightening creatures. During the first few meetings they speak a mysterious language, a mix of physics, computer programming and latex commands. Once you leave the office, you think that you are finally free. But it is not true because while you recover and relax a sheet of paper full of indecipherable letters and numbers materialises in your pocket: aiXiv:0906.0666, aiXiv:0609.889111... What are they? A magic formula? A code to communicate with the aliens? No, the code of the door of astronomical research, a place where you'll find an infinite number of papers waiting for you!

Mike is the "boss" and the "guardian" of the Circle. He has given me a lot of freedom (sometimes too much?) and has translated my ItalEnglish in a comprehensible scientific language. There is also "Ironwoman" Anne, recognisable from the strange shoes that she often wears. She is always running or riding or... correcting my thesis. Anne, Mike, thanks for teaching me how to do science: if I'm becoming a scientist it is mainly your fault! Finally I met Frazer, always ready to chat and to explain how "astronomical botany" works, and Andrew Benson, happy to create trees!

The second Circle is composed by the members of my family. It is always difficult to find the appropriate words for describing them. They are always part of my life, even now that they are far away, but it is hard to explain how they support me. Anyway, I'm becoming too philosophical. There is my brother Luca, luckily very different from me, Papà Gianni, who is asking news on my postdoc applications in every phone call (don't worry, the time I'll get the bloody postdoc I'll make you such a surprise that you will have an heart-attack!), and finally my Mamma, with her precious and constant telephone-support.

The department-Circle is a the most dangerous one. Recently it started to be populated by many babies so it is becoming a more pleasant place, but normally it is full of noisy coffee drinkers, football supporters, magicians and of people who work at night or from home. One of them is particularly weird. He wanders in the department pronouncing words that make no sense. If u start to hear "Ohi-Mama-Tortilla-Patata", Pipiripipì Fernando is approaching you and, believe me, you don't want to be on his way if he is looking for a "Pasadita". Fer, please keep in mind that the world is also

populated by bastards!

Few more characters deserve to be mentioned: my new “Girlfriend” Alkistis and her continuous up&down, Boris and Javier, who spend the time organising FIFA+NBA nights, “Gossipgirl” Alessandra with whom I had unforgettable aperitifs at the Staff Club/Mooch, and Riccardo, who helped me during the first period in this humid country.

In the hell I have also found an “angel”. Phil, you have gained the Heaven for saving me from the whims of my computers!

The most friendly of the Circles I’ve travelled through is the housemates’ one. This was very unexpected because my previous experiences have taught me that it is often full of annoying (and sometimes dirty) characters. Well, this time I was particularly lucky. There are Caroline, who has indulged my madness for a long time (but at the end she gave up and decided to spend a whole year in Indonesia), Rosa with her anti-Pope positions (the hell is the right place for you, uahahah!!!) and her hilarious excitement during the “Bang-battles”, Olivier and his very interesting culinary exchanges, and Arianna, the daily drop of honey. The new entries are Yara and the peculiar “divinity” that she always invokes (Coño!), the “anti-empire” Meysalung, who helped me to open my mind to a new culture (but I have to admit that some of her questions are weird!) and “$\mu\alpha\lambda\alpha\kappa\alpha\varsigma$” Mando, who has an enviable skill in selecting movies!

I know that you appreciate my nastyness and the fact that I avoid compliments, so if you don’t want to get shocked. . . don’t read the next three lines. Thanks Maria, “the Landlady”, for your precious, precise and punctual suggestions. In one sentence, for being someone between a mum and a sister: if I have feel “at home” here in England, it is also thank to you!!

Sylvia, I know that right now you are thinking: “and me??!!”. Your place. . . is in the next Circle, which includes all the people who populate (or have populated) Nottingham but not (lucky them!) the Department of Astronomy, plus. . . few others.

Andreas is always riding in it, in a sort of automatic-nervous mood. Sometimes he is tooooo german, but he is always a very good friend. Speaking about very strange characters, there is also “diokane” Spit, the italian “Woody Allen”, who “has broken my balls” by chat every single week during these 4 long years. The other inhabitants of

the Circle are slightly more normal, maybe because they are mostly girls: “Top Class” Karima and her brown curls, the girls of the first year (Adele, the French Caroline, Grace, Georgia, Giulia, Sylvia and Virginie), Andrijana and our “turbulent” friendship, my Portuguese “soulmate” lol Paula, who has defined me as nobody in the world, “the career-girl” Agnese, and Magda, a friend so special that any word to define her is useless.

In this Circle there are also two bunches of fellows.

In the first they are shooting to each other a mix of bullets and “gags”. They are the “Bang-band”: Coolhand, Renegate, The Clown, Rat-Woman, Undead, Weissbier and the new entry Matrioska.

The second one is composed only by “yellow souls”: Francisco, Yi-Hsien Chen (known as Lizard), Niels, “Leon” Lei, Martin, Huang+Judit, the nucleus of one of the best team in the history of the University of Nottingham Intramural League.

In conclusion (and in random order) there are Graeme, “Marko Brooko”, Ruth, “Celery Qiller” Jesus, Super-Amanda, Polish Magda (and her system Gogo), Nathan, Paula, Nara, Martina, Adriano, Graziano, Sam, “Kefiah” Omar, Sotiris, Medina.

The last Circle is the most mysterious, populated by strange creatures that have unconsciously switched on my fantasy (and in some cases my creativity). Here you don’t need any “magic mushrooms” becuase you can easily meet 3-Fingers, the Sea-Lion, Wet-Kiss, Finger-boy, the Red Peacock, the Siren, Sausage Roll and Sporty-Girl.

The journey is finally at its conclusion, but before the end I take the time for two “normal” acknowledgements: thanks to the rabbits of the Tennis Centre, to the squirrels of the Campus and to the fox of Beeston, usual encounters during my late-at-night rides Department-Beeston and. . . thanks to “my” Red Baby: without you my time in England would have been very, very hard!

Contents

List of Figures

List of Tables

Ultra-fine dark matter structure in the Solar neighbourhood

Chapter 1

Introduction

Our current understanding of the Universe relies on the existence of dark matter, the nature of which is still unknown. The most widely accepted idea is that it consists of “cold”, weakly interacting, non-baryonic particles (Cowsik & McClelland 1973; Szalay & Marx 1976), emitting no (or very little) electromagnetic radiation. The term “cold” derives from the fact that this material was non-relativistic at the epoch of matter-radiation equality. Its presence has been inferred only from indirect astronomical and cosmological observations, which I briefly summarise in Section 1.1.

In Section 1.1.1 the pioneering studies of the presence of unseen matter in the Solar neighbourhood (Oort 1932) and in clusters of galaxies (Zwicky 1933) are presented. The first convincing evidence for the existence of dark matter came from the flat, or even rising, optical rotation curves of spiral galaxies, described in Section 1.1.2. The specific case of the rotation curve of the Milky Way is presented in Section **??**. Dark matter is also required to explain the dynamics of galaxy clusters. Section 1.1.4 presents a specific example of this class of objects: the system E1 0657-558, commonly known as the “Bullet” cluster. Cosmology gives us more evidence for the existence of dark matter, and in Section 1.1.5 measurements of the amount of matter present in the Universe are reviewed.

Other explanations have been proposed for the observed mass discrepancy present in galaxies and more generally in the Universe, for example alternative theories of gravity (MOND, Milgrom 1983). In this Thesis we assume that this discrepancy is due to the

presence of dark matter.

1.1 Indirect astronomical and cosmological observations of dark matter

1.1.1 Pioneers in the search for dark matter

The idea that there is more matter present in the Universe than the amount that it is normally possible to observe started to be established as early as the 1930s. In 1932 Oort was the first to highlight the possible presence of dark matter, estimating the total mass gravitating close to the Sun. This amount, based on measurements of the stellar velocity distribution, was almost twice that accounted for by the visible stars in the Solar neighbourhood.

Despite Oort's work, the "discovery" of dark matter is generally attributed to the Swiss astronomer Fritz Zwicky, who estimated the total mass of the Coma Cluster by applying the virial theorem to the measured velocities of eight of its component galaxies (Zwicky 1933). The observation of very large peculiar velocities led to an unexpectedly high value for the mass of the cluster. As Zwicky pointed out, if the total mass was divided amongst the constituent galaxies, each of them would have an average mass of $5 \times 10^{10} M_{\odot}$ (where $M_{\odot}$ is the mass of the Sun), while their average luminous mass was estimated to be only $1 \times 10^{9} M_{\odot}$. This discrepancy clearly shows that these galaxies could not be made up only of stars like the Sun, and an extra contribution was hypothesised in order to maintain the cluster as a gravitationally bound system. These results led Zwicky to the following conclusion:

> *"The average density in the Coma system would have to be at least 400 times larger than that derived on the grounds of observations of luminous matter. If this would be confirmed we would get the surprising result that dark matter is present in much greater amount than luminous matter. "*

A few years later, Smith confirmed Zwicky's results, by applying the same technique to the Virgo cluster (Smith 1936).

1.1.2 Rotation curves in spiral galaxies

Historically, one of the most convincing pieces of evidence for the existence of dark matter comes from the analysis of rotation curves of spiral galaxies. It was in the early 20th century that the rotation of spiral galaxies started to be well established (Slipher 1914; Pease 1918). Assuming circular motion around the galactic centre for the gas and star components, it is possible to deduce the mass distribution of the galaxy by directly measuring the radial variation of the rotational velocity as a function of the distance from the centre. If we consider a galaxy and a test particle at radial distance r from the Galactic centre, according to Newtonian mechanics the circular velocity is given by

$$v_{circ}^2 = \frac{GM(r)}{r} \, , \tag{1.1}$$

where G is the gravitational constant and $M(r)$ is the mass within the radius r (which is assumed to be spherically symmetric).

In 1940, Oort found that the rotation curve of the galaxy NGC 3115 was not in agreement with that estimated from the luminous components. The discrepancy was explained by the presence of a large amount of dust or unseen matter in the outer part of the galaxy:

> *"It may be concluded that the distribution of mass in the system must be considerably different from the distribution of light . . . The strongly condensed luminous system appears embedded in a large more-or-less homogeneous mass of great density. "*

During the 1970s it became evident that most of the rotation curves of spiral galaxies remained roughly flat at large radii, where a Keplerian decline ($v \propto r^{-\frac{1}{2}}$) was expected. Given that most of the luminous matter is concentrated in the bulge and in the disk and assuming that the mass distribution within a galaxy is traced by light, Equation (1.1) predicts an increase of the velocity in the central region of the galaxy, followed by a relatively rapid drop.

The discrepancy between the flatness of rotation curves, observed well beyond the central region of the system, and the expected Keplerian decline was observed by a

number of authors (Freeman 1970; Einasto 1974; Rubin et al. 1970, 1978, 1980, 1982, 1985). It implies that the mass increases linearly with the galactocentric distance:

$$M(r) \propto r \ . \tag{1.2}$$

This result can be explained by postulating the presence of an extended dark matter halo in which the spiral galaxies are located. This idea was originally put forward by Ostriker & Peebles (1973). Figure 1.1 shows the rotation curve of a typical spiral galaxy, in this case NGC 6503 (Begeman et al. 1991), where the contributions of three different components are fitted. The disk and the gas are predominant in the inner region of the system, whereas the dark matter halo starts to dominate the gravitational potential at large radii. Optical rotation curves are not the best way to estimate the size and the mass of a galaxy because in the outermost part of the system the stellar luminosity becomes too faint to be measured, making the determination of their rotation velocity impossible.

From the late sixties, the development of radio telescopes provided a complementary approach for measuring rotation curves. At radio wavelengths it is possible to detect and map the HI 21cm emission line of the extended gaseous disk which surrounds spiral galaxies. HI clouds extend to distances 3 or 4 times larger than the optical disk, so such observations opened the way to the analysis of the kinematics of gas in the outermost parts of galaxies, showing that the rotation curve in the vast majority of cases remains flat even outside the optical disk (Rogstad & Shostak 1972; Bosma 1981).

1.1.3 The rotation curve and the dark matter distribution of the Milky Way

c

It is very difficult to measure the rotation curve of the Milky Way precisely, mainly due to the embedded position from which we observe it (we sit in one of its arms). The rotation curve presented in Figure 1.2 can be decomposed into contributions from three components: the galactic bulge, the disk and the dark halo. The two red lines represent respectively the baryonic component (bulge + disk) and the non-baryonic one (dark

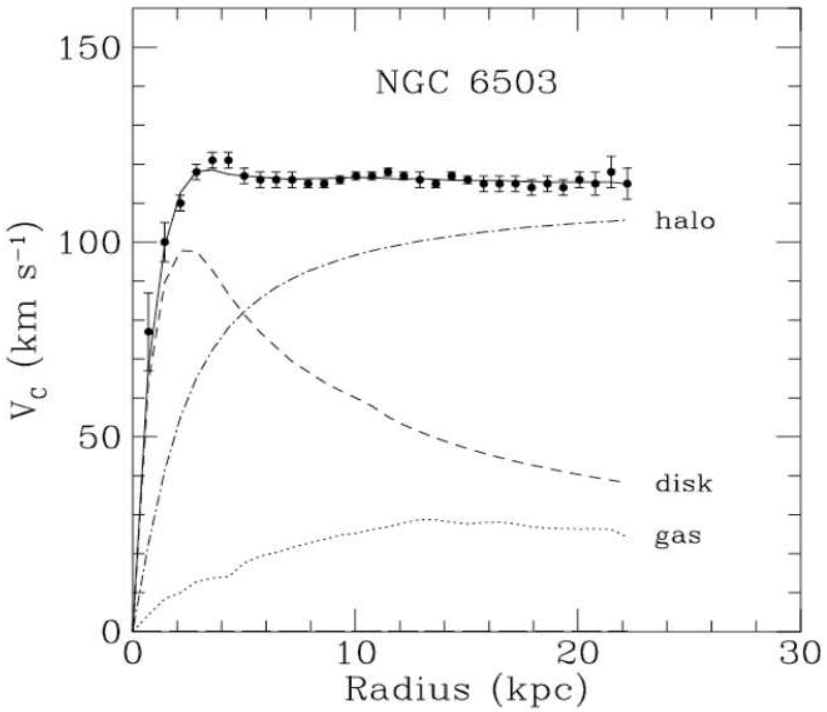

Figure 1.1: Rotation curve of the galaxy NGC 6503. The observations are shown as points, along with the model disk (dashed), gas (dotted) and halo (dash-dot) rotation curves. Their sum in quadrature is represented by the solid curve. From Begeman et al. (1991).

halo). The total, found by summing the components in quadrature, is shown in blue. The large scatter in the data, in particular at large radii, is caused by the embedded position of the Solar System. Nevertheless there is strong evidence for the presence of a dark halo. The Solar System is situated at approximately 8.5 kpc (Groenewegen & Blommaert 2005) from the Galactic centre. This is the galactocentric distance of the Sun assumed in this work, although recent estimates have suggested it may be as small as 7.5 kpc (Nishiyama et al. 2006; Groenewegen et al. 2008). Figure 1.3 presents the rotation curve if the dark halo is described by an isochrone potential. This is the potential selected to describe the Galactic halo of the Milky Way in the model developed in this project. The rotation curve is calculated for a particular set of normalization parameters: $k = GM = 1$ and $b = 1$. The motivations of this choice, together with a detail description of the properties of this potential, can be found in Section 2.3. It is important to notice that the two rotation curves are similar. In other words, the circular velocity at the Solar radius deduced with this set of normalization parameters is consistent with observations.

The measurement of the density of dark matter present in the Solar neighbourhood is

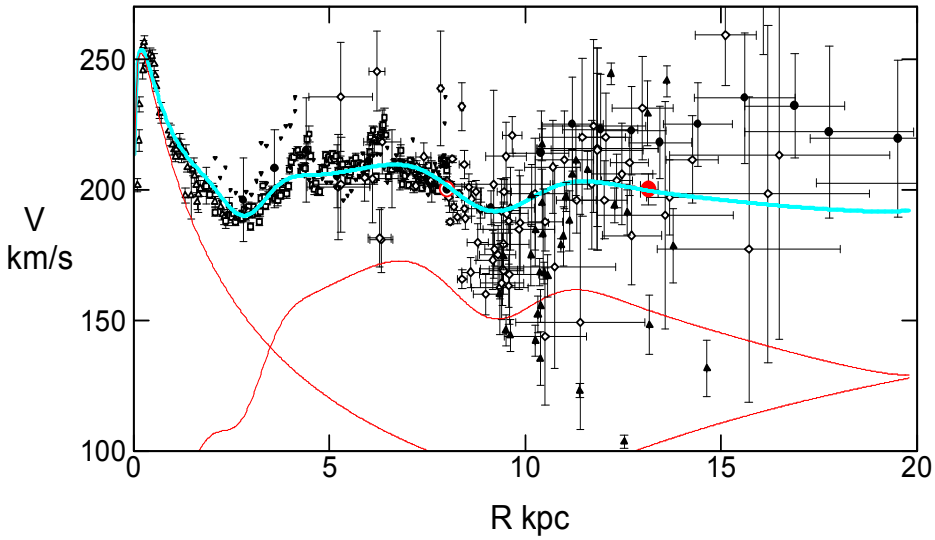

Figure 1.2: Unified rotation curve of the Milky Way reconstructed from the data currently available. The contributions of the three dominant components are also plotted: the two red lines represent respectively the total contribution of the bulge + disk and of the dark halo, whereas the blue thick line is the composite rotation curve. For more details, refer to Sofue et al. (2009).

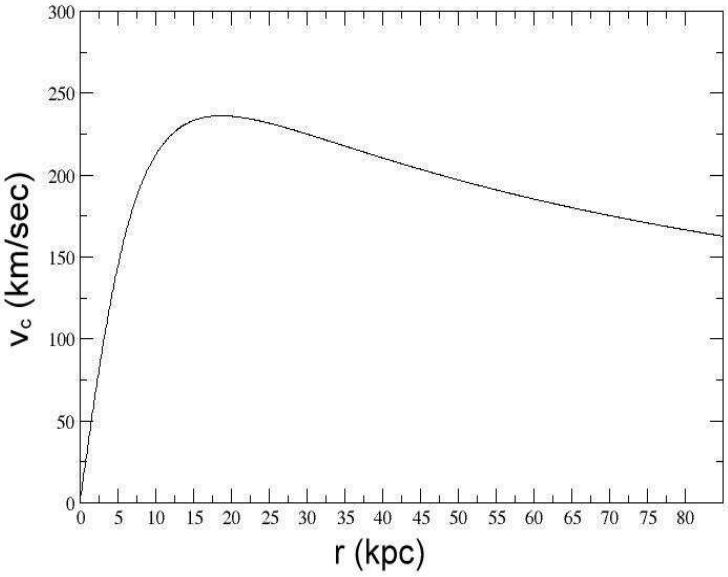

Figure 1.3: The rotation curve of the Milky Way, calculated using the model described in Chapter 2. The potential adopted for the description of the Galactic halo is the isochrone one. Although not intended as a realistic model, this particular potential can be tuned through the quantity $k = GM$ and the characteristic lengthscale b to approximate the rotation curve of the Milky Way, as it is possible to see comparing it with Figure 1.2. In this simulation $k = b = 1$.

particularly important for direct detection experiments. Figure 1.2 suggests that the dark halo component starts to dominate the gravitational potential of the Galaxy at ~ 5 kpc. The local density lies in the range $\sim 0.3 - 0.7$ GeV cm^{-3} (Weber & de Boer 2010). The lower limit is calculated assuming that the Galaxy is composed of a central bulge, a disc and an extended dark matter halo with a cuspy density profile; the upper one considers the additional contribution of dark disks. Due to the large number of free parameters available for the fit of rotation curves, caused mainly by the presence of different components dominating at different scales, the value of the local density ρ_0 is not well determined by such rotation-curve analysis.

1.1.4 Gravitational lensing and mergers of clusters: the special case of the "Bullet" cluster

One of the best places to gravitationally infer the existence of dark matter is clusters of galaxies, because the gravitational lensing technique can be straightforwardly applied to these massive systems. In the recent past, weak gravitational lensing has become a powerful tool to investigate the presence of dark matter in clusters of galaxies and to trace its distribution. This technique takes advantage of the distortion of the image of background galaxies, which is caused by the presence of a massive object between the sources in the background and the observer, to reconstruct the mass distribution of the lensing cluster.

Probably the most famous example is 1E 0657-558, commonly known as the "Bullet cluster". The peculiarity of this system, that is presented in Figure 1.3, is due to the fact that the cores of the two merging clusters passed through each other only ~ 100 Myr ago at a relative velocity of about 4.5×10^3 km sec^{-1}. The cluster is situated in the relatively nearby Universe, at a redshift of $z = 0.296$, which makes it possible to obtain accurate observations in different wavelengths (Clowe et al. 2004, 2006).

During the collision the galaxies, which behave as collisionless systems, are spatially decoupled from the hot intracluster gas, which is slowed down by the action of ram pressure. This process heats the gas to temperatures up to 10^7 K, causing a shock that typically emits at X- rays wavelengths. Clowe et al. (2006) mapped the gravitational

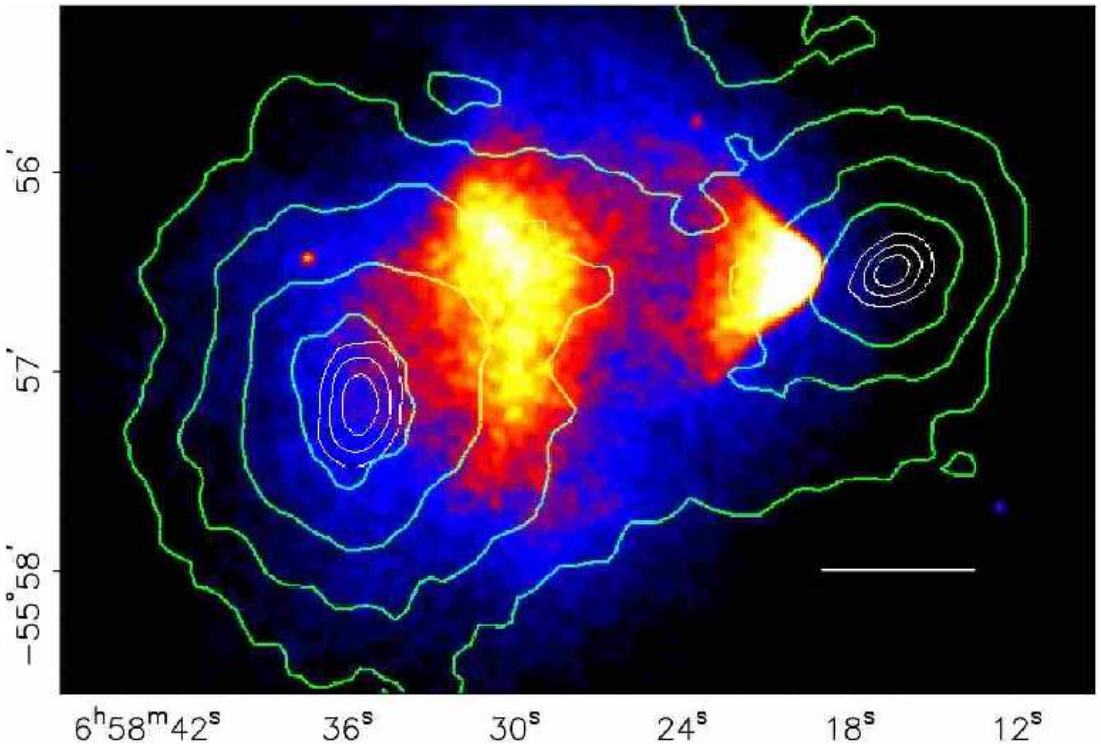

Figure 1.4: Chandra image of the merging cluster 1E 0657-558, with the white bar indicating 200 kpc. The weak-lensing reconstruction is shown in green contours. From Clowe et al. (2006).

potential of this system using weak lensing, and compared it with X-ray observations, obtained using Chandra. As the gas is the dominant component of the baryonic mass, if this was the only source of mass, the gravitational potential should trace the distribution of this baryonic component. However, from the lensing observations, the potential is spatially coincident with the collisionless galaxies, implying that the mass is dominated by a dark massive component, which is collisionless like the galaxies.

1.1.5 Dark matter in the Universe

The abundances of the components of the Universe have been determined with very high precision. The fraction of the *i*th component to the present density of the Universe, ρ_{0i}, is denoted by the density parameter,

$$\Omega_i = \frac{\rho_{0i}}{\rho_{0c}} \,, \tag{1.3}$$

where

$$\rho_{0c} = \frac{3H_0^2}{8\pi G} \tag{1.4}$$

is the present day critical density for which the geometry of the Universe is flat, H_0 is the present-day Hubble parameter and $G = 6.672 \times 10^{-8}$ cm^3 g^{-1} s^{-2} is the gravita-

tional constant. A very accurate value of the abundance of dark matter has been provided by the measurements of the temperature anisotropies of the Cosmic Microwave Background (CMB). The analysis of the WMAP 7-years data (Larson et al. 2010) finds a cosmological dark matter density of

$$\Omega_{CDM} = 0.228 \pm 0.013 \, . \tag{1.5}$$

The theory of nucleosynthesis, combined with high redshift observations of the light element abundances, finds a baryon density of (Tytler et al. 2000, Burles & Tytler 1998, Schramm & Turner 1998)

$$\Omega_b \simeq 0.045 \pm 0.0025 \, , \tag{1.6}$$

in very good agreement with the baryon density from the CMB (Komatsu et al. 2009, Larson et al. 2010):

$$\Omega_b = 0.0449 \pm 0.028 \, . \tag{1.7}$$

The fact that $\Omega_b \ll \Omega_{CDM}$ underlines the point that we live in a universe dominated by dark matter.

1.2 The nature and the detection of dark matter

In the first part of this Chapter the observational evidences for the existence of non-baryonic dark matter in the Universe have been discussed. The most important properties that a well motivated dark matter candidate must satisfy are discussed in Subsection 1.2.1. Weakly Interactive Massive Particles (hereafter WIMPs) are considered one of the most promising dark matter candidates. They are presented in Subsection 1.2.2, while Subsection 1.2.3 focuses on the different detection techniques.

1.2.1 General properties of dark matter

Dark matter has never been observed directly, but what are the requirements for a good candidate?

- It should be stable, or at least must have a lifetime longer than the age of the Universe. This is a consequence of the fact that we still see its gravitational

effect, in the form of the structures that we observe today in the Universe (for more details see e.g. Colless et al. 2001; Dodelson 2003; Tegmark et al. 2006).

- It should be collisionless, in order to form extended halos. Non-negligible self-interaction would lead to the evaporation of dark halos. After each interaction one particle would be ejected from the halo, while the second would move to a smaller radius, to a state of lower energy. The result of this process would be the evaporation of the halo (Hénon 1969).

- It should be optically dark, without strong coupling to photons or to the other particles of the Standard Model. Its interaction with baryons must be weak, since no evidence of interaction has yet been discovered. If dark matter particles were strongly coupled with baryons, then during the formation of a galaxy they would fall, together with the baryons, into the potential well of the system. This mixture of baryons and dark matter would interact, producing photons. Up to now, no evidence of such a signal has been discovered.

- It should be electrically neutral in order to avoid the formation of anomalous charged heavy elements and to not be in disagreement with Big Bang Nucleosynthesis (Olive et al. 2000; Fields & Sarkar 2006).

- Any candidate should have a mass density smaller than or equal to the measured dark matter abundance in the Universe, $\Omega_{CDM} \sim 0.228 \pm 0.013$ (Komatsu et al. 2009, Larson et al. 2010).

1.2.2 Weakly Interactive Massive Particles

The most popular non-baryonic candidates are WIMPs, which arise in many extensions of the Standard Model of particle physics. One of the most plausible candidates, but not the only one, is the lightest neutralino in Supersymmetric models, commonly labelled as χ. WIMPs are compelling for very specific reasons: being stable, weakly interacting and having mass of the order of tens to hundreds of GeV/c^2, if we assume that they are their own anti-particles, an estimate of their relic abundance (Bertone et al. 2005) gives a result very close to the measured cold dark matter abundance [Equation (1.5)]. They

decouple early from ordinary matter (they are not the only candidate to decouple early because axions can decouple as well) and finally, being non-relativistic, they behave as cold dark matter when matter starts to dominate and structures start to form. This seems to be in agreement with observations of large-scale structure.

1.2.2.1 Relic abundance of WIMPs

Shortly after the Big Bang, the Universe was in a very hot and dense state (Lemaître 1931, for further details see Kolb & Turner 1990). WIMPs were in thermal equilibrium and nearly as abundant as lighter particles (photons, quarks, leptons, etc.). Their equilibrium abundance was maintained via rapid interconversion of particle-antiparticle pairs of Standard Model particles:

$$\chi + \chi \rightleftarrows X + \overline{X} \, , \tag{1.8}$$

where X indicates a general particle and $\overline{X}$ its antiparticle. The process occurs when the thermal energy is larger than the rest mass of the particle:

$$k_b T > m_\chi c^2 \, , \tag{1.9}$$

where k_b is Boltzmann's constant and c the speed of light. In other words, due to the fact that WIMPs are massive particles ($m_\chi \sim 100$ GeV/c^2), their momentum after the formalism is small, limiting the final states available in the phase-space.

For quantifying the number of WIMPs in a certain volume, it is convenient to scale out the effect of the expansion of the Universe. This can be done by considering the comoving number density Y_χ, which is the number of WIMPs divided by the entropy density s:

$$Y_\chi \equiv \frac{n_\chi}{s} \, , \tag{1.10}$$

where n_χ is the WIMPs number density. As the space expands, the number density drops. Hence, the comoving number density multiplied by a^3 is static in the presence of expansion:

$$Y_\chi \propto n_\chi a^3 \, . \tag{1.11}$$

In the regime of high temperatures, when radiation dominates, the comoving number of particles is proportional to the third power of the temperature, since $a \propto T^{-1}$:

$$n_\chi \propto T^3 \, . \tag{1.12}$$

As the temperature of the Universe drops the thermal energy of the particles becomes smaller than the WIMP rest mass energy. In these conditions WIMPs are no longer produced, but they can still annihilate

$$\chi + \chi \rightarrow X + \overline{X} \, , \tag{1.13}$$

and the non-comoving number density decreases exponentially

$$n_\chi \propto (m_\chi T)^{-\frac{3}{2}} \exp(-m_\chi c^2/k_b T) \, . \tag{1.14}$$

The temperature at which this happens is determined by $\langle \sigma_A v \rangle$, the thermal average of the annihilation cross-section σ_A and the velocity of the particle v. Freeze-out occurs when the WIMP interaction rate Γ_{fo} is of the order of the Hubble parameter,

$$\Gamma_{fo} = n_\chi \langle \sigma_A v \rangle \ll H \, . \tag{1.15}$$

This sequence of events is illustrated in Figure 1.5, which shows the comoving number density of WIMPs as a function of the dimensionless parameter $x = m_\chi c^2/k_b T$. The solid curve is the equilibrium abundance, and the dashed curves represent the frozen out relic WIMP population for a range of values of $\langle \sigma_A v \rangle$. The present day WIMP density can be estimated as (Jungman et al. 1996; Green et al. 2004; Bertone et al. 2005)

$$\Omega_\chi = \frac{m_\chi n_\chi (a_{fo}/a_0)^3}{(3H_0/8\pi G)} \sim 0.3 \left(\frac{10^{-26} \mathrm{cm^3 s^{-1}}}{\langle \sigma_A v \rangle h} \right) , \tag{1.16}$$

where $h = 0.7$ is the dimensionless value of the Hubble constant. The WIMP cross-section is $\sim 10^{-8}$ picobarn, which corresponds to 10^{-44} cm^2 (Bertone et al. 2005, Ahlen et al. 2010). The larger the annihilation cross-section rate $\langle \sigma_A v \rangle$ is, the later freeze-out occurs, and the smaller the present day WIMP density is.

1.2.3 Detection of WIMPs

There are different approaches for the detection of WIMPs. The first possibility is to produce them in a collider. Colliders can infer the existence of WIMPs, but they will not be able to confirm them as a good cosmological dark matter candidate, as explained in Section 1.2.3.1. This limitation can only be overcome by observing the

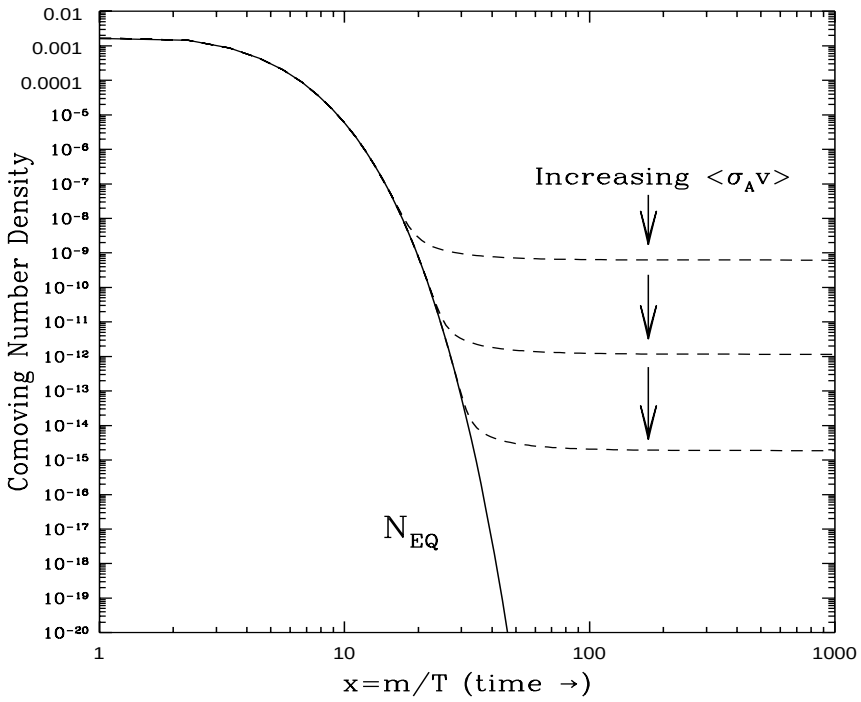

Figure 1.5: The WIMP comoving number density as a function of the dimensionless parameter $x = m_\chi c^2/k_b T$. This parameter decreases with the temperature when a system is no longer in thermal equilibrium. As the Universe expands and cools, the WIMP annihilation ceases and the comoving number density "freezes out". The larger the annihilation cross section, the longer the particles remain in equilibrium and hence the smaller the relic abundance. From D'Amico et al. (2009).

candidate directly (or indirectly) in an astrophysical context. Indirect detection experiments search for the products of WIMP annihilation, whereas direct detection aims to detect the scattering of dark matter particles on atomic nuclei.

1.2.3.1 Colliders

The Large Hadron Collider (LHC) at CERN (European Council for Nuclear Research) is a proton-proton collider and it may be able to produce these heavy particles. The production and detection of WIMPs at the LHC would be a very exciting achievement, but it will not demonstrate the existence of cosmological dark matter. One of the main reasons is the impossibility of proving that the detected candidate is a stable particle. The limit on the lifetime of these hypothetical WIMPs will be very short ($\sim 10^{-8}$ s), whereas the lower limit on the lifetime of a good dark matter candidate must exceed the current age of the Universe (~ 14 Gyr, Kamatsu et al. 2010). Even if it was stable, it would not prove that in the early Universe WIMPs were produced in the right quantity.

This limitation can be overcome by observing the candidate both in direct and indirect astrophysical experiments and comparing the results of the two observations.

1.2.3.2 Indirect detection

Indirect detection is based on the detection of some of the products of WIMP annihilation. This process generates antimatter (such as antiprotons and positrons), neutrinos, γ-rays and, subsequently, synchrotron radiation. We have seen in Section 1.2.2.1 that the annihilation of WIMPs stops in the early Universe, when the density is not high enough to maintain the reaction. Nevertheless, after structures form, the density in particular regions may be high enough for WIMP annihilation to occur. Some locations where WIMP annihilation may occur at an observable rate include the centres of galaxies, dark matter-dominated substructures (e.g. dwarf galaxies) and the cores of dense bodies, such as the Sun or our own planet.
A wide range of experiments is aiming to detect a signal coming from the Milky Way halo (Ellis et al. 1988; Turner & Wilczek 1990; Kamionkowski & Turner 1991; Silk & Srednicki 1984), the Galactic centre (Bergstrom et al. 1998), and dwarf satellite galaxies (Evans, Ferrer & Sarkar 2004; Bergstrom & Hooper 2006). Some of the most recent experiments are the ground-based air Cerenkov telescopes VERITAS, HESS and MAGIC, and the satellites EGRET and Fermi, but they have not yet produced any clear detection.

It is also possible to look for neutrinos produced by WIMP annihilation in the core of the Sun (Srednicki et al. 1987) and of the Earth (Krauss et al. 1986). IceCube (still under construction) and ANTARES are the most recent examples of neutrino telescopes, but no evidence of WIMPs has been found so far.

1.2.3.3 Direct detection

The most convincing evidence that dark matter exists and is composed of WIMPs would be a direct observation through its elastic scattering on nuclei (Goodman & Witten 1985). If dark matter scatters elastically with normal matter, it would generate a nuclear recoil. This interaction can be detected via the energy that is released as

phonons (heat), ionisation, or scintillation.

The WIMP direct detection rate, dR/dE, which is usually expressed as the number of events detected per kg, per day, per keV, depends on the local dark matter density ρ_χ and on the local speed distribution $f(v)$ in the detector rest frame (Jungman et al. 1996, Lewin & Smith 1996):

$$\frac{dR}{dE} = \frac{(m_p + m_\chi)^2}{m_p^2 m_\chi^3}\,\sigma_p\,\rho_\chi\,A^2F^2(E)\int_{v_{min}}^{v_{esc}}\frac{f(v)}{v}\,dv\;, \tag{1.17}$$

where m_p and m_χ are the mass of the proton and the WIMP respectively, σ_p is the scattering cross-section on the proton, A is the mass number of the target nucleus and $F(E)$ is the target form factor. This last term takes into account that the target nucleus is not point-like.

The quantity

$$v_{min} = \left(\frac{E(m_A + m_\chi)^2}{m_A m_\chi^2}\right)^{\frac{1}{2}} \tag{1.18}$$

is the minimum speed which can cause a recoil of energy E, m_A the mass of the target nucleus, and v_{esc} is the escape velocity from the Milky Way. The value usually assumed for this quantity is 544 km s^{-1} (Smith et al. 2007). Note that in Equations (1.17)-(1.18) we set $c = 1$. It is very difficult to give a precise estimate of the local halo density and of the WIMPs' velocity distribution. The establishment of a reliable model for the Milky Way is currently a very active topic of research in astrophysics, but it still represents a significant source of uncertainty. At present the standard halo model assumes that the Milky Way is an isotropic, isothermal sphere with Maxwellian velocity distribution, while simulations produce triaxial, anisotropic halos, with a large amount of substructure. Direct detection probes the ultra-local dark matter distribution on sub-mpc scale, which is the distance covered in one year by a terrestrial detector, as we will explain in detail later in this Chapter. For this reason the possible presence of a significant amount of fine-grained features, such as overdensities and streams, would have important consequences for direct detection. A stream of particles produces a step in the energy spectrum, and the speed of the particles composing the stream can be inferred from the energy at which the feature occurs (Gelmini & Gondolo, 2001).

The recoil energy is very small, on the scale of keV, due to the fact that the velocity of the Sun through the Galactic halo is ~ 220 km s^{-1} (Kerr & Lynden-Bell 1986) and

that the mass of WIMPs is about 100 GeV/c^2. One of the main challenges in direct detection is the suppression of backgrounds that mimic WIMP-induced nuclear recoils. Today's leading experiments have achieved a good rejection of the backgrounds originating from particles which produce electron recoils, such as photons, electrons, and alpha particles. Neutrons are another insidious source of background because the induced nuclear recoils are identical to those induced by WIMPs. Neutrons are produced by natural radioactivity of the detector's components and the surrounding materials, or by high-energy cosmic rays. These backgrounds can be reduced by locating the detectors in deep-underground laboratories, by using radio-pure materials in the construction of the detectors, and by measuring more than one energy channel (ionisation, scintillation and phonons).

Current detectors can be sensitive to one or more of these channels. HDMS, GENIUS, TEXONO and CoGENT have been built to detect the ionisation signal, while DEAP, CLEAN, XMASS, KIMS, and ANAIS look for scintillation. The last category of one-channel experiments is sensitive to phonons and includes CUORE and CRESST-I. Moving to two-channel detection technique: ArDM, ZEPLIN-III and XENON10 are sensitive to both ionisation and scintillation, whereas EUREKA, CDMSII, EIDELWEISS and SuperCDMS are sensitive to ionisation and phonons. Finally CRESST-II is looking for phonons and scintillation. A diagram of these experiments is presented in Figure 1.6.

1.2.3.4 The annual modulation and DAMA

Another search strategy has been used by the DAMA (DArk MAtter) Collaboration. This experiment looks for an annual modulation in the event rate. The origin of the annual modulation is shown in Figure 1.7: the Sun moves through the Milky Way, and consequently through its dark halo, and in the meantime the Earth orbits around the Sun. The result of the Earth's annual motion is an annual modulation of the WIMPs-nucleus scattering rate, with an increase in June and a decrease in December (Drukier et al. 1986). It is not difficult to think of terrestrial backgrounds that might mimic this annual modulation. For this reason the DAMA group has analysed, tested and eliminated many of them, such as the ones due to natural radioactivity. At the same

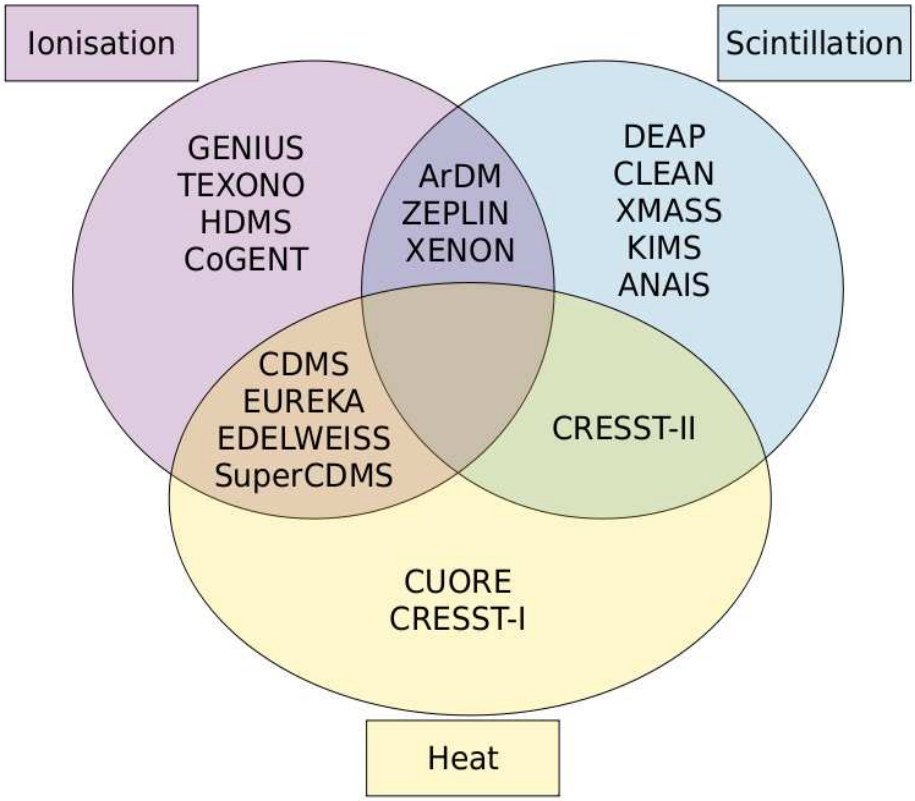

Figure 1.6: Diagram showing some of the direct detection experiments currently ongoing. Current detectors are sensitive to one or more of these signals: ionisation, scintillation and phonons. HDMS, GENIUS, TEXONO and CoGENT detect the ionisation signal, whereas CUORE and CRESST-I look for phonons. The last category of one-channel detectors are sensitive to scintillation: DEAP, CLEAN, XMASS, KIMS, and ANAIS. Two-channel detectors, ArDM, ZEPLIN and XENON are sensitive to both ionisation and scintillation, CRESST-II to phonons and scintillation, whereas EUREKA, CDMS, EDELWEISS and SuperCDMS to ionisation and phonons.

time it is very difficult to detect the modulation because it is expected to be very small (a few % of the mean rate). Nevertheless, since 1996 DAMA has observed an annual modulation signal consistent with what would be expected if WIMPs had been detected (Bernabei et al. 2008b). However, the result is in conflict with the findings of other direct dark matter experiments because the corresponding values of the WIMP mass and cross-section are in portions of the parameter space already excluded by other experiments [See Sandick (2010) for a review of the status of searches].

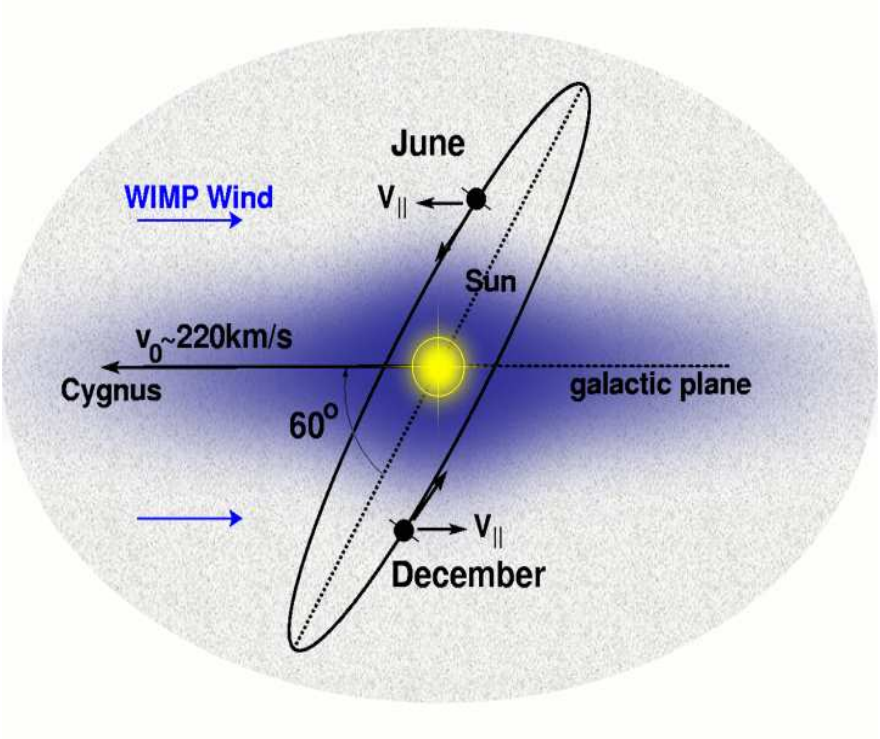

Figure 1.7: Schematic representation of both the directional signal and the annual modulation effect. The Sun moves through the Galactic halo at ~ 220 km s^{-1}. Its motion causes a peak in the WIMP flux along the same direction. The annual modulation effect is caused by the motion of the Earth around the Sun at a speed ~ 30 km s^{-1}. From http://www.hep.shef.ac.uk/research/dm.

1.2.3.5 Directional detection

The first to point out that the recoil event rate could be directional was Spergel in 1988. The main goal of direct detection experiments is to use the direction dependence to discriminate WIMPs from background noise. The WIMP flux is expected to peak in the direction of the motion of the Sun in its orbit around the Galactic centre, while the recoil event rate is consequently expected to peak in the opposite direction. Compared to non-directional detectors, directional ones have the advantage of distinguishing neutron backgrounds from WIMP signals. Recoils from neutrons should be either isotropically distributed, or point towards where radioactive material is present, whereas the WIMP signal is expected to be correlated with the direction of the Sun's motion. A small number of events would be enough to discriminate between an isotropic and an anisotropic WIMPs distribution in the Solar neighbourhood. Using an ideal detector capable of reconstructing the direction of the recoil nuclei, ~ 10 events would prove that WIMPs distribution is isotropic (Morgan et al. 2005), while ~ 30 would confirm that it peaks in the direction opposite to the one of the Solar motion (Green &

Morgan 2010). Currently many experiments are ongoing, such as DRIFT, DMTPC and MIMAC. The angular resolution that has been achieved by these experiments is $\sim 10^{\circ}$ (Dujmic et al. 2008, or see Ahlen et al. 2010 for a complete review). Models of the predicted directional signals usually assume that the WIMP distribution in the Galaxy is predominantly smooth and isotropic, hence the study and modelling of the local distribution in the Milky Way is a key point of the discussion.

1.3 Numerical simulations and alternative approaches to the ultra-local dark matter distribution

If we look at the distribution of galaxies in the Universe, we note that they are not scattered in a random way. Galaxies, groups and clusters of galaxies are linked together in a pattern of sheets and filaments that is commonly known as the "cosmic web". Figure 1.8 shows the distribution of galaxies in the near Universe (out to redshift $z = 0.25$) as observed by the 2-degree Field Galaxy Redshift Survey (2dFGRS, Colless et al. 2001). The structure of the filaments and voids visible in the survey cannot be explained only as the result of the gravitational clumping of the baryonic matter present in the Universe, thus requiring the presence of dark matter. Numerical simulations provide a reliable method of calculating the dark matter distribution on large scales, making robust predictions for its clustering.

This Section gives an overview of the state-of-art of numerical simulations, focusing in particular on Milky Way-like systems, and on the alternative approaches developed to overcome their resolution limits. The broad topic of cosmological simulations is overviewed in Subsection 1.3.1. Subsection 1.3.2 presents the most important simulations of a single Milky Way-like dark matter halo, focusing on the amount of substructure found and on their contribution to the local dark matter distribution. The ultra-fine WIMP distribution in the Solar neighbourhood is described in Subsection 1.3.3. Finally, we present the motivation of this Thesis in Section 1.4, followed by an overview in Section 1.5.

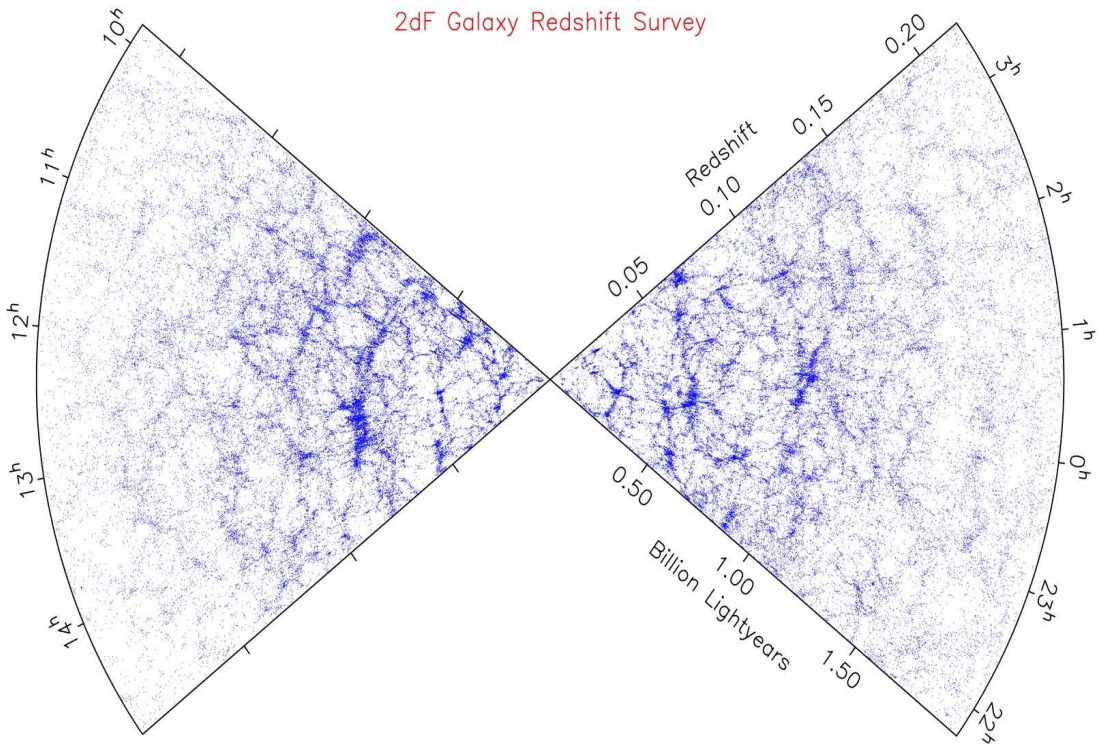

Figure 1.8: The galaxy distribution obtained from the survey 2dFGRS, which determined distances for more than 220,000 galaxies, out to a redshift $z = 0.25$. From http://magnum.anu.edu.au/ TD-Fgg/.

1.3.1 N-body simulations

The richness of structures that we observe in Figure 1.8 originates from the CMB anisotropies, through a complex and highly nonlinear process driven primarily by gravity. During the last 13 billion years, ordinary matter cooled, condensed and fragmented to generate galaxies. Unfortunately observations do not provide a complete picture of the evolution of structures, mainly because they are snapshots of the state of the Universe at a precise epoch. The link between the early, almost uniform Universe shown by the CMB and the large amount of structures that we can observe nowadays has been provided by numerical simulations.

The first N-body simulations showed that non-baryonic cold dark matter is the main driver in the formation of cosmic structures (Peebles 1982, Frenk et al. 1985), and that it is required to match the observed large-scale properties of the Universe. The structures that we can currently observe have been formed hierarchically. The first objects to collapse were small halos: they merged, following a “bottom-up” scheme, and formed systems of increasing size (White & Frenk 1991). Groups and clusters of galaxies formed as halos aggregated into larger systems. The resolution of the cosmo-

logical simulations was not sufficient to resolve the inner parts of the individual dark matter halos.

In the last few years, N-body simulations have provided results over a unprecedented range of scales, from halos similar to those hosting Local Group dwarf spheroidal galaxies to halos corresponding to the largest galaxy clusters (Springel et al. 2005, Boylan-Kolchin et al. 2009). They have also confirmed that many mergers are incomplete because some of the merging halos survive as gravitationally bound subhalos, orbiting mainly in the outer regions within their hosts. This was previously also found by other authors (Moore et al. 1999, Klypin et al. 1999).

1.3.2 Milky Way halo simulations

In the last few years numerical simulations, such as Via Lactea II (Diemand et al. 2008), GHALO (Stadel et al. 2008) and Aquarius (Springel et al. 2008), were able to reproduce the formation and the evolution of a single galactic halo. The goal of these projects was to understand the formation and the structure of a Milky Way-like dark matter halo down to a resolution of about 100 pc. A "Milky Way" halo refers to a $10^{12} M_{\odot}$ system, with no presence of massive close neighbours and no trace of recent major mergers. This new generation of numerical simulations has resolved a incredibly large number of substructures, both gravitationally bound (halos) and unbound (streams). The reason for this huge number of substructures is that not all the subhalos are massive enough to suffer significant dynamical friction, which causes decaying orbits, large mass loss and in some cases complete merging. Tidal stripping removes mass mainly from the outer, less bound regions of subhalos (Ghigna et al. 1998, Diemand et al. 2007), and the substructures often preserve an intact inner, bound region, that is mostly unaffected by mass loss.

A comparison between the three main projects is shown in Table 1.1. The mass resolution of the three simulations, which is the mass of each particle in the simulation, has the same order of magnitude ($10^3 M_{\odot}$) and the softening assumed is of a few parsec. In a system of particles, the gravitational force acting between two particles of masses

Name	Particle Mass (M⊙/h)	Softening (pc)	N°of halos simulated
Aquarius	1.7×10^3	21	6
Via Lactea-II	1.0×10^3	60	1
GHALO	4.0×10^3	40	5

Table 1.1: Summary of the recent simulations of Milky Way-like halos: Aquarius, Via Lactea-II and GHALO. The three columns describe their mass resolution, the softening length and the number of Milky Way-like halos that have been simulated.

M_1 and M_2 is

$$F = \frac{GM_1M_2}{r^2} \ , \tag{1.19}$$

where r is the distance between them. The system reaches a singularity when $r \to 0$. To avoid this, Equation (1.19) is modified by introducing a constant c in the denominator:

$$F = \frac{GM_1M_2}{r^2 + c^2} \ . \tag{1.20}$$

In other words a dimension is assumed for the particles composing the system, while in theory they are point-like. Nowadays more sophisticated softening techniques are assumed in the development of N-body simulations.

The Aquarius Project (Springel et al. 2008) is a Virgo Consortium project that performs high-resolution simulations of Milky Way-like halos ($\sim 10^{12} M_\odot$) in a ΛCDM cosmology. These single halos were firstly selected from a lower resolution version of the Millennium-II Simulation and then re-simulated at various resolutions up to about 1.5 billion particles. The mass resolution is $1.7 \times 10^3 M_\odot$ and the softening is 21 pc. Aquarius finds that 13 % of the total mass is resolved in subhalos, but below 0.1 % of the mass within the Solar Circle (~ 8.5 kpc) is in resolved subhalos. Moreover, all halos have a similar speed distribution. Figure 1.9 compares the speed distribution in a 2 kpc box centred on the Solar position with a multi-variate Gaussian fit. Finally, they argue that the local velocity distribution is smooth and it is created by overlapping of a large number of streams. This point is discussed more in detail in Section 1.3.3.1.

The Via Lactea II simulation (Diemand et al. 2008) has similar properties to Aquarius: it has a mass resolution of $1.0 \times 10^3 M_\odot$ and a softening length of 60 pc. The mass of the Milky Way-like halo that has been simulated was $1.9 \times 10^{12} M_\odot$. The top panel of Figure 1.10 shows the local phase-space density in a cube of 40 kpc, revealing both the presence of hundreds of very concentrated dark matter clumps and of numerous cold streams. Looking at the plot it is possible to note that the dark matter clumps have

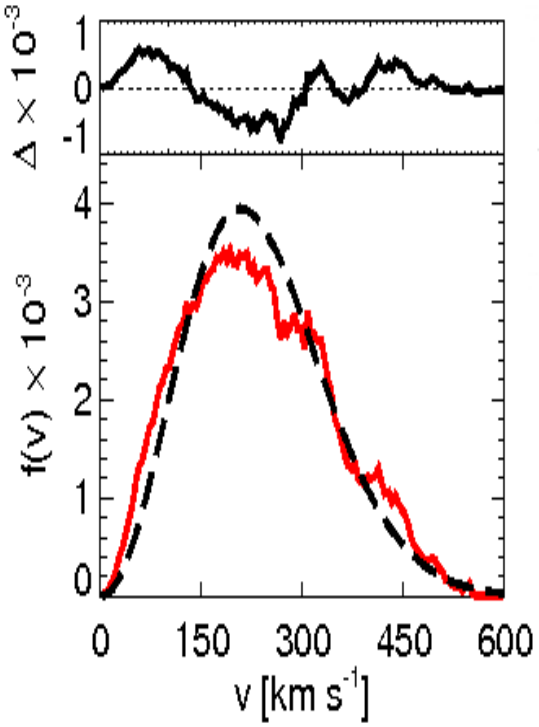

Figure 1.9: Velocity distribution in a 2 kpc box centred on the solar position versus the absolute value of the speed. The red line shows the result of the Aquarius simulation, the black dashed one a multivariate Gaussian model fit. The residuals are shown in the top panel. From Vogelsberger et al. (2009).

high phase-space density. This is caused by their very dense central region and also by the low velocity dispersion of the particles they are made of. On the other hand, the streams are formed of material stripped from accreted and disrupted subhalos. They have a lower phase-space density, almost 10^{-2} times lower than the local one, but despite this they stand out in the phase-space because of their low velocity dispersion, which is about one order of magnitude smaller than that of the background.

GHALO (Stadel et al. 2008) is a series of high resolution N-body simulations of a Milky Way-like dark halo. They are simulations of the same halo at different resolutions, from 10^5 to over one billion particles, with a mass resolution of $4.0 \times 10^3 M_\odot$ and a softening of 40 pc. At redshift zero the simulation resolves over 100,000 orbiting substructures. GHALO shows that the six dimensional phase-space profile is dominated by the presence of the substructures and it does not follow a power law, except in the smooth, inner few kpc. In addition to the gravitationally bound, dense subhalos discussed above, there are structures in the phase-space of CDM halos.

The results of these three simulations broadly agrees, but they disagree over implica-

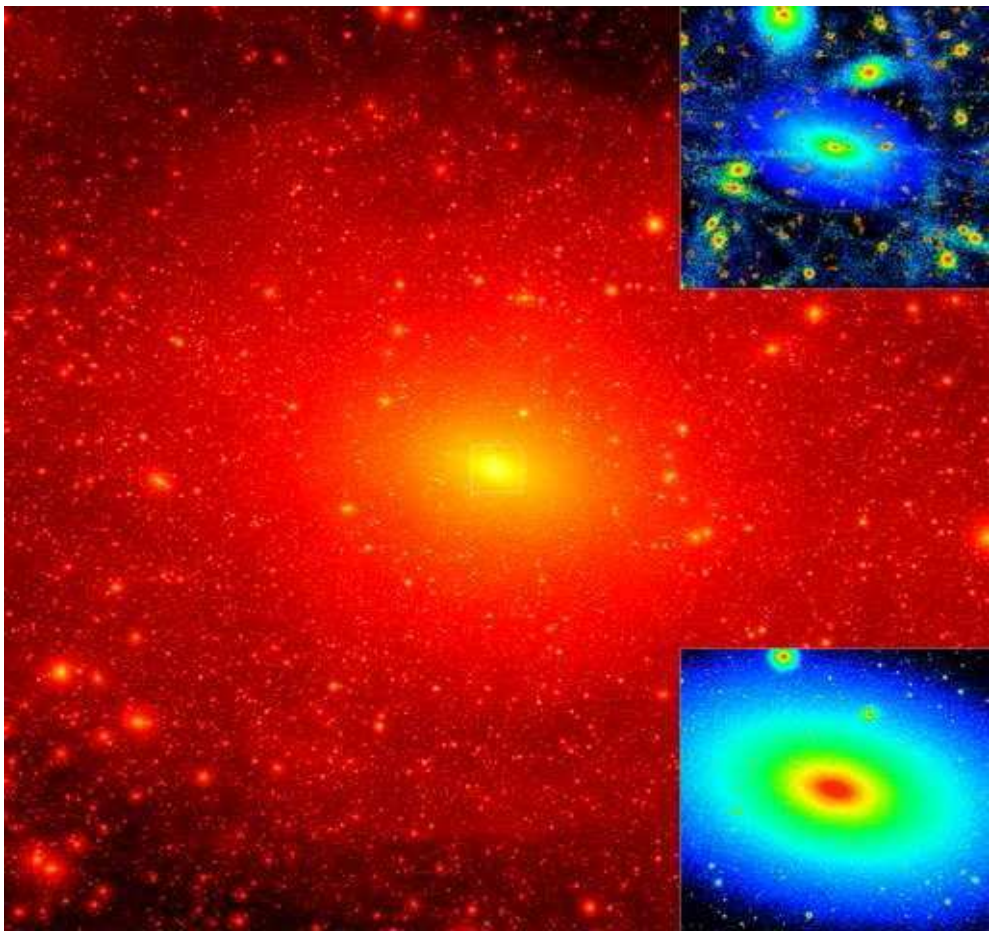

Figure 1.10: Projected dark matter density in Via Lactea II in a 800 kpc cube. The top square focuses on the local phase-space density, the bottom on the local density, both in an inner 40 kpc cube. From Diemand et al. (2008).

tions for indirect detection experiments, such as the contribution of subhalos to the total γ-rays WIMP annihilation signal. It is important to note that the results of these simulations cannot be used to predict the ultra-local distribution, as we will see below.

1.3.3 Ultra-local WIMP distribution in the neighbourhood

Numerical simulations are a remarkable and powerful tool for understanding both the large scale structure of the Universe and the galactic scale. However, they cannot resolve the ultra-fine dark matter distribution, which is crucial for direct detection experiments. The scales relevant for these instruments are the distance that they probe during the experiment's lifetime. If we assume that the Sun's circular velocity around the centre of the Galaxy is $v_\odot \sim 200$ km s^{-1}, the distance covered over an year is

$$\mathrm{r_{det}} \sim \mathrm{v_\odot}\, \tau_{\mathrm{exp}} \sim (200\ \mathrm{km/s})\ (1\ \mathrm{yr}) \sim 0.1\ \mathrm{mpc}\,. \tag{1.21}$$

This distance is six orders of magnitude smaller than 100 pc, which is the best resolution obtainable by state-of-the-art N-body simulations described above. Moreover, WIMPs have very small thermal velocities, allowing the formation of micro-halos with masses down to $10^{-6}M_{\odot}$ (Green et al. 2004). Masses of this order of magnitude are far smaller than the smallest subhalos resolvable, which have mass of order $10^{4}M_{\odot}$. These are insurmountable problems for the conventional simulation techniques, indicating that a completely different approach is required to describe in detail the ultra-fine dark matter distribution probed by direct detection experiments. Finally, there is not even agreement yet on a point as basic as whether this distribution is smooth or not.

1.3.3.1 Mass and velocity distribution

The WIMPs distribution at the Solar radius depends crucially on the Galaxy's merger history and on the presence of substructures in the velocity space. The WIMP velocity distribution is conventionally assumed to be an isotropic Maxwellian distribution with a cut-off at the escape velocity of the Galaxy (Freese et al. 1988), but other examples are present in the literature, such as a multivariate Gaussian (Evans et al. 2000; Helmi et al. 2002). These models rely on the assumption that the Milky Way halo has reached a steady state so that the ultra-local dark matter phase-space distribution is smooth. This would imply that the velocity distribution of the Galaxy is smooth as well. This assumption is questionable: because structures form hierarchically, and the age of the Universe is not large compared with relevant dynamical timescales such as the crossing time, it is not certain whether the ultra-local phase-space dark matter distribution is smooth or clumpy.

Some recent theoretical investigations argued that the ultra-local WIMP distribution consists of a large number of streams, of the order of 10^{5-6} (Helmi et al. 2002; Vogelsberger et al. 2009, Vogelsberger & White 2010). Such a large number of overlapping streams would lead to a smooth local velocity distribution (Moore et al. 2001, Zemp et al. 2009). Moreover, considering that the most prominent streams contribute less than one percent to the local dark matter density, even if the Solar System was located within one of these streams, its signal would not be strong enough to be distinguishable

from the background.

It has also been argued that the ultra-local WIMP distribution consists of a relatively small number of streams (Moore et al. 1999; Stiff & Widrow 2003; Fantin et al. 2008). The most recent accretion events are possibly the most interesting ones. If some of the particles in these subhalos have been stripped by the potential of the Galaxy, the tidal debris will have had little time to mix and therefore be relatively coherent. These streams, composed of high velocity particles, may produce significant features in energy spectrum, even if they constitute only a small fraction of the total local dark matter density (Stiff et al. 2001, Freese et al. 2001). In this case the observed energy spectrum would consist of a number of sloping steps. The positions of steps would depend on the WIMPs mass, on the target nuclei mass and on the unknown speed of the streams, whereas their heights would depend on the WIMP cross-section and on the (unknown) stream density, allowing these physical quantities to be constrained by potentially observable quantities. However, further studies are needed to quantify or exclude the relevance of possible very fine grained features in the local distribution for dark matter detection experiments.

1.3.3.2 Stiff and Widrow method

Stiff and Widrow (2003; hereafter SW) developed an elegant method to calculate the dark matter ultra-local velocity distribution at a single spatial point of the phase-space. They put down a uniform grid of massless test particles at the point of interest (the position of an ideal terrestrial detector) of a dark matter halo. Evolving both the test and the simulation particles backward to the initial time, they calculated the intersection points between the phase-space sheet of the test particles and the initial phase-space distribution. Finally they calculated the distribution function of the test particles at the point of interest. Using this reverse technique they reach a resolution that cannot be reached by N-body simulations. They found that the speed distribution in the Solar neighbourhood, assumed as the position of the detector, is characterised by the presence of a discrete number of peaks. These peaks correspond to streams of particles passing through the detector at different speeds.

The top panel of Figure 1.11 compares the velocity distribution obtained using a classi-

cal forward technique (dotted line) to the reverse method (solid). A forward technique simulates the evolution of a system of particles from a precise moment in the past, chosen as an initial condition, to the present. This technique is not particularly powerful when we are interested in the distribution in a particular location because the number of particles in any given region of space is not statistically significant. In the lower panel the angle between the local bulk motion and each intersection point between the phase-space sheet of the test particles and the initial phase-space distribution is shown. The plots highlight the advantage in using the reverse technique: the distribution function presents very clear peaks, which highlight the presence of streams of particles. These signatures are almost absent using a more conventional forward evolution approach. This can be explained by the fact that with a large volume one obtains a broad distribution and sees little evidence for discrete structures. The reverse method allows one to find the distribution function at a single point, optimising the analysis of the ultra-fine dark matter distribution.

Unfortunately the reverse integration is numerically unstable because of the presence of chaotic motions. This problem requires the introduction of a softening length of 20 kpc [for more detail, see Stiff & Widrow, 2003]. If we compare this value to the distance between the Sun and the centre of the Galaxy (~ 8.5 kpc), we can see that this softening is large enough to radically affect the phase-space distribution imprinting on a terrestrial detector. This technique can be used in conjunction with standard cosmological simulations, but it has not been implemented in a full cosmological context. This improvement would give the possibility to get a better estimate of the dark matter velocity distribution in the Solar neighbourhood.

Recently a new technique for calculating the phase-space distribution function in the neighbourhood of a simulation particle has been developed (Vogelsberger et al. 2008). This technique allows the study of the evolution of a stream's density and the estimation of the fine-grained dark matter distribution in the Galactic halo. A critical question in the development of this technique is the possibility to estimate the number of streams expected in the Solar neighbourhood. To answer to this question recently Vogelsberger and White (2010) have suggested that the picture on ultra-local scales will not be too different from the one presented by N-body simulations. They estimate the presence of about $\sim 10^{12}$ streams and $\sim 10^{6}$ "massive" ones in the Solar position. Therefore

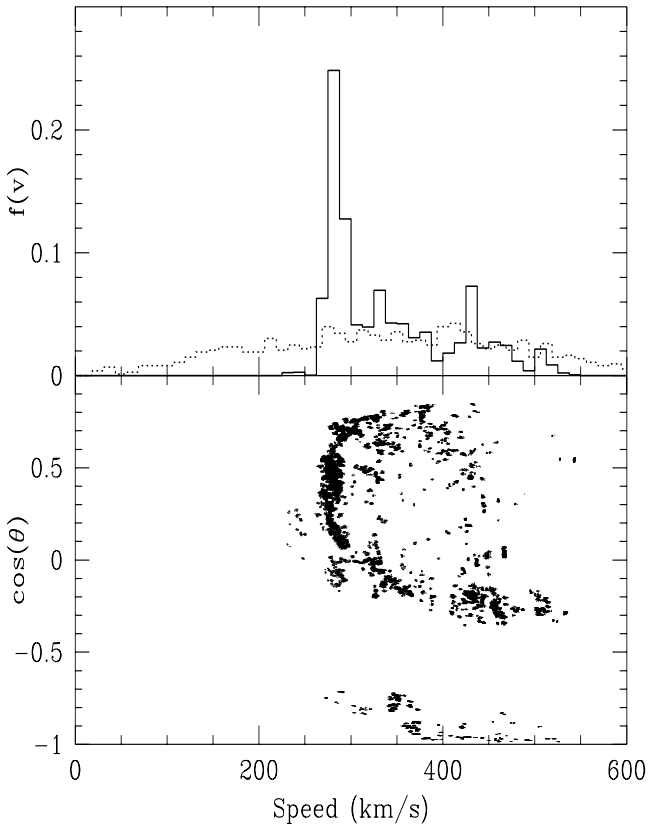

Figure 1.11: Top panel: Comparison between the speed distribution obtained using the reverse technique developed by Stiff & Widrow (solid line), and a conventional forward simulation (dotted). Bottom panel: Distribution of angle measured with respect to some arbitrary direction in the halo. From Stiff & Widrow (2003).

the local velocity distribution is predicted to be smooth, in clear conflict with the SW results.

1.4 Motivations of the Thesis

Mergers and accretion appear to be fundamental driving mechanisms in determining the present day properties of galaxies. In this context, it is particularly interesting to focus on the details at the ultra-fine spatial scales at the late stage of the interaction between a subhalo and a dark matter halo.

Very recently, large simulations of the formation of the Milky Way have resolved a relatively small amount of substructure in the central region of the Galaxy. Unfortunately the scales relevant for terrestrial instruments are of the order of milliparsecs, too small even for the most powerful simulation. To solve this problem alternative approaches have to be designed.

In this Thesis, we develop a model which studies halo mergers in a Milky Way-like galaxy, with the aim of producing the first detailed model of the properties of the ultra-fine dark matter distribution in the Solar neighbourhood. Hence we make predictions of the signal detectable in the current and upcoming generation of directional detectors. With the numerical technique developed in this Thesis, it is possible to resolve structures produced by minor mergers of subhalos with a larger parent halo, which are inaccessible to conventional N-body simulations.

When applied in a cosmological context, using merger trees to describe the history of a Milky Way-like halo, the method becomes a powerful instrument to simulate the velocity distribution in the Solar neighbourhood. The method we have developed is very flexible, allowing us to calculate the evolution of the spatial distribution and to map out the velocity structure at any time and position at arbitrarily-high resolution. Finally we interpret these results in the context of dark matter experiments, trying to provide predictions of useful diagnostic quantities for directional detectors.

1.5 Thesis overview

In this Chapter we have given a brief overview of the astrophysical evidence for the existence of dark matter. We have described the different techniques currently available for detecting it and have discussed some of the experiments currently under way around the globe. Finally, we have described the state-of-art of standard cosmological simulations, focusing in particular on the latest generation of simulations of Milky Way-like halos. Since the relevant scales for direct detection experiments, of the order of mpc, cannot be probed by cosmological simulations, we have also described some alternative approaches developed in the recent past to investigate the ultra-fine dark matter distribution of our galaxy.

In Chapter 2, we introduce the numerical technique that we have developed to simulate the interaction between a Milky Way-like galaxy and a dark matter subhalo. The model investigates the effect on the ultra-local dark matter distribution of mergers in the history of a Milky Way-like dark halo, focusing on the ultra-fine scales probed by current direct detection experiments. The Chapter includes the description of action-

angle variables, the main tool used in the development of the model, and the analysis of the initial conditions. The relevant results obtained using this numerical technique are presented in Chapter 3. In Chapter 4 we put the model in a cosmological context. The final results, presented in Chapter 5, produce a detailed analysis of the ultra-fine dark matter distribution in the Solar neighbourhood, without the computational overhead of a complete numerical integration. Finally, we summarise the method, together with the most significant results, in Chapter 6.

The model and the results presented in Chapters 2 and 3 has been already published as: Fantin et al. 2008.

The work in Chapters 4 and 5 is in preparation for publication as: Fantin et al. 2010.

Chapter 2

Model of a merger between a galaxy and a system of particles

In this Chapter we present the numerical technique we have developed to investigate the effect of mergers on the ultra-fine scales probed by direct detection experiments of DM. Section 2.1 gives a short overview of the goal of the project. We introduce the action-angle variables (hereafter AA) and some of their properties in Section 2.2, while in Section 2.3 we describe the potential we assume for the description of the Galactic dark matter halo. AA are a fundamental instrument for developing the backward-in-time technique our model is based on, which is presented in Section 2.4. Finally Section 2.5 is dedicated to the analysis of the choice of the initial conditions.

2.1 Goal of the model

Aiming to provide a simple approach to understanding the late-stage evolution of a satellite merger, we model the interaction between a unbound systems of particles and a Milky Way-like galaxy. We calculate the ultra-fine dark matter distribution in the Solar neighbourhood using a simplified model for the host halo that expresses the dynamics of the system in AA. Although this simplification is not a completely realistic description of the Milky Way, the model has the great benefit of being analytically solvable. This particular approach makes it possible to carry out an accurate and rapid

calculation of the velocity distribution of the system at any time and at high spatial resolution. This is vital if we want to understand the sub-mpc-scale structure of the Milky Way's halo probed by terrestrial dark matter detectors, a topic that we have discussed in Section 1.2.3. Moreover, it makes possible to perform a detailed analysis of the hypothetical signature of a series of merger events in a terrestrial dark matter detector, without the limitations in resolution usually present in N-body simulations.

Although we have introduced WIMPs because they are one of the most plausible and well-motivated non-baryonic candidate for dark matter, the model we develop is valid for any collisionless cold, dark matter candidate, and it does not depend on the properties of the particular dark matter candidate.

2.2 The Action-Angle variables

Phase-space is a six-dimensional space described by the position and velocity coordinates $\mathbf{x}$ and $\mathbf{v}$. In this space orbits follow particular paths, and the basic structures are orbital tori (Binney & Tremaine 2008). Position and velocity are not always the best options for describing the motion on these tori, and in particular cases the choice of other sets of coordinates, such as the AA $(\boldsymbol{\theta}, \mathbf{J})$, can be more appropriate. The actions are

$$J_i = \frac{1}{2\pi} \oint_{\gamma_i} \mathbf{v} \cdot d\mathbf{x} \qquad (i = 1, 2, 3) \,, \tag{2.1}$$

where γ_i is a closed path around the torus. They are adiabatic invariants of these tori, so called because holding the actions constant define the surfaces of the tori. Actions also generate a set of coordinates, the angle variables, which define a position on any torus. Moreover, actions are constant during changes of the potential that are slow compared to a typical orbital frequency. Now we have a new set of canonical coordinates which defines completely a point in the phase-space: the angles are the coordinates and the actions the momenta. If we consider a dynamical system with a time-independent Hamiltonian H, such as the motion of a dark matter particle on a regular orbit, the

evolution of the system in the AA is given by Hamilton's equations

$$\begin{aligned} \dot{J}_i &= -\frac{\partial H}{\partial \theta_i} = 0 \,, \\ \dot{\theta}_i &= \frac{\partial H}{\partial J_i} \equiv \Omega_i(\theta) \,, \end{aligned} \tag{2.2}$$

where Ω_i are the corresponding angular frequencies and H is constant on any torus. Consequently H, which corresponds to the total energy of the system, is a function of the actions but not of the angles. Integrating Equation (2.2), the evolution of the angles is linear, allowing the solution at any epoch (either forward or backward in time) to be expressed trivially in terms of the initial conditions:

$$\theta_i(t) = \theta_i(t_0) - \Omega_i(t - t_0). \tag{2.3}$$

An important property of the angles is that they are 2π-periodic:

$$\mathbf{x}(\theta_i) = \mathbf{x}(\theta_i + 2\pi) \,, \qquad \mathbf{v}(\theta_i) = \mathbf{v}(\theta_i + 2\pi) \,. \tag{2.4}$$

In conclusion, AA are an extremely powerful and useful instrument to describe the motion of dark matter particles. Nevertheless it is difficult to find an appropriate potential in which it is possible to have analytic expressions for the angular frequencies Ω_i. In the rare cases in which we can obtain those frequencies, Equations (2.2) - (2.4) allow us to determine immediately the evolution of any orbit. Static spherical potentials are one of these rare cases. More details about the AA and their properties can be found in Binney & Tremaine (2008), Gerhard & Saha (1991) and McGill & Binney (1990).

2.3 The isochrone potential

To describe the Galactic halo we adopt the isochrone potential (Hénon 1959)

$$\phi(r) = -\frac{GM}{b + \sqrt{b^2 + r^2}} \,. \tag{2.5}$$

Although not intended as a realistic model for a complex system like the Milky Way, it can be tuned through its mass M and characteristic lengthscale b to approximate a range of systems.

Poisson's equation give us the density distribution of this potential:

$$\rho(r) = \frac{1}{4\pi G r^2}\frac{d}{dr}\left(r^2\frac{d\phi}{dr}\right) = M\left[\frac{3(a+b)a^2 - r^2(b+3a)}{4\pi(a+b)^3a^3}\right] , \tag{2.6}$$

where

$$a \equiv \sqrt{b^2 + r^2} . \tag{2.7}$$

The density of the system at small radii $(r \ll b)$,

$$\rho(r) \simeq \frac{3M}{16\pi b^3} , \tag{2.8}$$

is roughly constant, while at large radii $(r \gg b)$

$$\rho(r) \simeq \frac{Mb}{2\pi r^4} . \tag{2.9}$$

The radial period T_r is defined as

$$T_r = 2\int_{r_1}^{r_2} dr \Big/ \left[2(E - \phi(r)) + \frac{L^2}{r^2}\right]^{\frac{1}{2}} , \tag{2.10}$$

where E is the numerical value of the Hamiltonian, which refers to the energy of an orbit, and r_1 and r_2 are respectively the pericenter and apocenter distances. The pericenter is the point of closest approach of the orbit to the centre of the system, whereas the apocenter is the furthest one. The name isochrone comes from the fact that the radial period depends only on the energy and not on the angular momentum of a particle orbiting in this potential:

$$T_r = \frac{2b}{\sqrt{-2E}}\int_{s_1}^{s_2} \frac{(s-1)}{\sqrt{(s_2 - s)(s - s_1)}}\, ds = \frac{2\pi GM}{(-2E)^{\frac{3}{2}}} . \tag{2.11}$$

Note that in Equation (2.11) we have assumed negative energy because we are dealing with bound orbits, while s is an auxiliary variable:

$$s \equiv \frac{GM}{b\phi} = 1 + \sqrt{1 + \frac{r^2}{b^2}} . \tag{2.12}$$

The isochrone potential is an approximation of the Keplerian one if $b \to 0$, while the limit $b \to \infty$ corresponds to the spherical harmonic oscillator.

The adoption of this potential increases the timescale necessary for the tidal disruption of a satellite which is falling into the Galaxy. The main reason for the increase is that in phase-space the particles of the satellite follow toroidal paths and the actions are

constant on these tori. This does not allow any of the particles composing the system to leave the toroidal path that it is following. This limit remove the possibility of having a "mixing" effect perpendicular to the torus, leaving only the "mixing" effect due to the angle variables, which wrap around the torus. Moreover, we have to take into account that orbits of different angular momentum, but the same energy, have the same frequency. This fact has an impact in increasing the "mixing" time of the system. The consequence of these two effects is an overestimate of the granularity of the system at the present time. In other words, the real dark matter distribution will be smoother than the one predicted by our model. Although this simplified potential provides a less realistic representation of the Milky Way, its qualitative properties are similar to the ones of our galaxy, and it has the great benefit of being analytically soluble, so the dynamics of the merger can be calculated remarkably simply. Thus, the gravitational force does not have to be artificially softened, allowing one to test whether this effect did compromise the SW results, as discussed in Section 1.3.3.2.

2.4 Technique

The model we have developed is based on a backward evolution technique and it is based on Gerhard & Saha (1991) and McGill & Binney (1990). The model is able to simulate quickly and efficiently the present-day fine-scale dark matter velocity distribution in a detector volume located in the Solar System.
The principal steps in constructing this model are:

1. Select initial conditions for the satellite.
2. Choose the present-day detector spatial location $\mathbf{x}$, and a velocity $\mathbf{v}$ of interest.
3. Convert the phase-space coordinates into AA variables.
4. Analytically evolve the AA back to t_0, the time in the past when the satellite fell into the host system.
5. Transform the AA back into Cartesian coordinates.

6. Evaluate the initial phase-space density of the merging satellite at this location, which is also the phase-space density in the present-day detector at velocity $\mathbf{v}$. This is justified by Louville's theorem, which states that the density around a PS point is constant in time.

7. Repeat for a grid of velocities at this location to map out the full velocity distribution observable within the detector.

As mentioned in Section 2.3, we adopt the isochrone potential, introduced in Equation (2.5), for the description of the massive system, assuming $k = MG$ as normalisation for the mass of the system. Because of the assumption of this potential, the best way to express its dynamics in the phase-space is in terms of spherical coordinates (r, θ, φ). Consequently we need the Hamiltonian as a function of the spherical coordinates. Once this is obtained, we can find the relations between this set of variables and the AA variables.

The Hamiltonian of the system is:

$$H(\mathbf{x}, \mathbf{v}) = -\frac{k}{b + \sqrt{b^2 + r^2}} + \frac{v^2}{2} \, . \tag{2.13}$$

To calculate the actions we need to solve Equation (2.1). It is possible to use the Hamiltonian introduced in Equation (2.13) for the transformation between the AA and the phase-space coordinates (Binney & Tremaine 2008) because

$$\boldsymbol{\theta} = \frac{\partial H}{\partial \mathbf{J}} \, ; \qquad \mathbf{v} = \frac{\partial H}{\partial \mathbf{x}} \, . \tag{2.14}$$

These equations express $\boldsymbol{\theta}$ and $\mathbf{v}$ in terms of $\mathbf{J}$ and $\mathbf{x}$. Equation (2.1) becomes

$$J_i = \frac{1}{2\pi} \oint_{\gamma_i} \frac{\partial H}{\partial \mathbf{x}} \cdot d\mathbf{x} \, . \tag{2.15}$$

It is now possible to calculate the values of the actions along curves on which only one of the coordinates varies:

$$\begin{cases} J_\varphi &= \mid L_z \mid , \\ \\ J_\theta &= L - \mid L_z \mid , \\ \\ J_r &= \dfrac{\sqrt{kb}}{\sqrt{-\dfrac{2Hb}{k} - f_l}} \, , \end{cases} \tag{2.16}$$

where L is the magnitude of the angular momentum vector, L_z the z-component of the angular momentum and

$$f_l = \frac{1}{2}\sqrt{\frac{L^2}{kb}} + \sqrt{1 + \frac{L^2}{4kb}} \, . \tag{2.17}$$

Before proceeding further, it is convenient to define some auxiliary variables:

$$a \equiv -\frac{k}{2H} - b \, , \tag{2.18}$$

$$e \equiv \sqrt{1 + \frac{L^2}{2Ha^2}} \, , \tag{2.19}$$

$$\sin\psi \equiv \frac{rv_r}{ae\sqrt{\frac{k}{a+b}}} \, , \tag{2.20}$$

$$\theta_0 \equiv \arctan\left(\frac{\sqrt{L^2 - L_z^2}}{\mid L_z \mid}\right) , \tag{2.21}$$

$$\sin\chi \equiv \frac{\sin\theta}{\sin\theta_0} \, . \tag{2.22}$$

Note that θ_0 is the turning point of the orbit. The quantities a and e do not have a simple geometric meaning, but in the Keplerian limit they reduce to the major axis and the eccentricity, while ψ is the mean anomaly.

Substituting the expression for f_l into Equation (2.16) allows us to rewrite the Hamiltonian as a function of the actions

$$H = -\frac{1}{2(J_r + f_l)^2} \, , \tag{2.23}$$

and leads to the calculation of the orbital frequencies:

$$\omega_\theta \equiv \frac{\partial H}{\partial J_\theta} = \frac{\sqrt{k}}{2(a+b)^{\frac{3}{2}}}\left(1 + \frac{L}{\sqrt{4bk + L^2}}\right) , \tag{2.24}$$

$$\omega_r \equiv \frac{\partial H}{\partial J_r} = \frac{(-2H)^{3/2}}{k} \, . \tag{2.25}$$

Equation (2.25) expresses the well-known property of the isochrone potential: the radial period for a given energy is independent of the angular momentum.

Following Gerard & Saha (1991) and McGill & Binney (1990), it is possible to determine the angle variables. The first is

$$\theta_r = \psi - \frac{ae}{a+b}\sin\psi \, . \tag{2.26}$$

We need to introduce one more auxiliary variable,

$$\Lambda(\psi) \equiv \arctan\left(\sqrt{\frac{1+e}{1-e}}\tan\frac{\psi}{2}\right) + \frac{L}{\sqrt{L^2+4bk}}\arctan\left(\sqrt{\frac{a(1+e)+2b}{a(1-e)+2b}}\tan\frac{\psi}{2}\right), \tag{2.27}$$

to be able to obtain the other two angles. To ensure the continuity of Λ we can add multiples of π to the argument of the arctans:

$$\Lambda(\psi) \longrightarrow \Lambda'(\psi)\ , \tag{2.28}$$

with

$$\Lambda'(\psi) = \Lambda(\psi) + n\pi\ . \tag{2.29}$$

The other two angle variables are

$$\theta_\theta = \frac{\omega_\theta}{\omega_r}\theta_r - \Lambda + \chi\ , \tag{2.30}$$

and

$$\theta_\varphi = \theta_\theta - \frac{\tan\theta}{\tan\theta_0}\ . \tag{2.31}$$

This method shows that in the isochrone potential it is possible to analytically evaluate all the angle variables directly from ordinary phase-space coordinates. Applying Equation (2.3), it is thus possible to determine the evolution of any orbit at any time in a single step. We are interested in determining the position at time t_0 of a particle that is currently located within the detector volume. Once the particle is evolved backward in time, we need to determine its position in the phase-space. As we have seen above, the AA are a very powerful instrument to determine the evolution of a system, but not such a user-friendly tool to describe positions. We need to return to the spherical coordinates, expressing them as function of the AA.

The Hamiltonian can then be expressed in terms of the actions

$$H(\mathbf{J}) = \frac{-2k^2}{(2J_r + L^2 + \sqrt{4bk+L^2})^2}\ , \tag{2.32}$$

For the calculation it is convenient to define the quantity

$$l' \equiv \sqrt{1-\frac{L_z^2}{L^2}} = \frac{\sqrt{J_\theta^2 + 2j_l \mid L_z \mid}}{L}\ . \tag{2.33}$$

Using the auxiliary variables defined in Equations (2.18)-(2.22) and the definition (2.30) it is possible to obtain an expression for the spherical coordinate r,

$$r = a\sqrt{(1-e\cos\psi)\left(1-e\cos\psi+\frac{2b}{a}\right)}\ . \tag{2.34}$$

The definition of the auxiliary function is given by

$$\chi = \theta_\theta - \omega_\theta \Gamma(\psi) + \Lambda(\psi) \ , \tag{2.35}$$

where

$$\Gamma(\psi) \equiv \sqrt{\frac{a+b}{k}}(a+b)\theta_r \ , \tag{2.36}$$

and Λ, given in Equation (2.27), is useful for the calculation of the other spherical coordinates:

$$\sin\theta = \sqrt{1 - \frac{L_z^2}{L^2}} \sin\chi \ , \tag{2.37}$$

and

$$\varphi = \theta_\varphi - \theta_\theta + \frac{\tan\theta}{\tan\theta_0} \ . \tag{2.38}$$

Note that this coordinate does not depend on the actions, which describe the dynamics of the system.

We can finally express the position of the particle at t in the classical phase-space coordinate

$$\mathbf{x} = \begin{cases} r\cos\varphi\cos\theta \ , \\ r\sin\varphi\cos\theta \ , \\ r\sin\theta \ , \end{cases} \tag{2.39}$$

and

$$\mathbf{v} = \begin{cases} v_r\cos\varphi\cos\theta - v_\theta\cos\varphi\sin\theta - v_\varphi\sin\varphi \ , \\ v_r\sin\varphi\cos\theta - v_\theta\sin\varphi\sin\theta - v_\varphi\cos\varphi \ , \\ v_r\sin\theta + v_\theta\cos\theta \ . \end{cases} \tag{2.40}$$

The calculation of the conjugate momenta

$$p_\theta = \frac{Ll'\cos\chi}{\cos\theta} \ , \tag{2.41}$$

$$p_r = \sqrt{\frac{k}{a+b}}\frac{ae\sin\psi}{r} \ , \tag{2.42}$$

is essential to determine the components of the velocity in the spherical coordinates

$$v_r = p_r \ , \tag{2.43}$$

$$v_\theta = \frac{p_\theta}{r} \ , \tag{2.44}$$

$$v_\varphi = \frac{L_z}{r\cos\theta} \ . \tag{2.45}$$

The method described above explores the distribution of the particles at one single point of the phase-space, that we associate with a detector in the Solar neighbourhood. Once we have defined the velocities of the particles passing through this point at redshift zero, we are able, using the backward-in-time technique and the properties of the AA, to track the motion of these particles and to determine whether they come from a particular region of the phase-space. Unlike a conventional N-body approach, the gravitational force does not have to be artificially softened, and the phase-space can be explored rapidly and accurately, without the computational overhead of numerical integration.

2.5 Initial conditions

To see whether a particular velocity in the present-day detector translates back to a point in the phase-space populated by the infalling subhalo, we need to specify the boundary conditions of the detector and the subhalo. These are:

- The position of the detector today, r_0.
- The infall time of the satellite, t_i.
- The location of the satellite in the phase-space $(\mathbf{r_{sat}}, \mathbf{v_{sat}})$ at t_i.
- The initial velocity dispersion of the subhlalo, σ_v.
- The initial spatial extent of the subhalo, σ_s.

Note that all quantities at the present time are identified by a "zero" subscript. The detector is assumed to be placed in the Solar neighbourhood, at a distance $r_0 \simeq 8.5$ kpc from the Galactic centre. The quantity t_i identifies the time in the past, corresponding to a redshift z, at which the satellite falls into the Milky Way's halo.

2.5.1 Multivariate Gaussian distribution for the satellite velocity distribution

To complete the model, we need to specify the initial dark matter phase-space distribution of the merging halo. The simplest representation that provides enough freedom to explore the dependence on the properties of the merging halo is provided by a bivariate Gaussian,

$$f(\mathbf{r},\mathbf{v}) \propto \; e^{-[(\mathbf{r}-\mathbf{r_{sat}})^2/2\sigma_s^2)]} e^{-[(\mathbf{v}-\mathbf{v_{sat}})^2/2\sigma_v^2]} \; . \tag{2.46}$$

The backwards-in-time technique allows us to pinpoint efficiently those particles from the initial merging satellite that are to be found passing through an arbitrarily-small detector today, and by choosing the grid of velocities appropriately we can map out the velocity structure with any resolution that we desire. In the choice of the extremes of the grid we must take into account the existence of the escape speed

$$v_{\rm esc} = \sqrt{2 \mid \phi(r) \mid} = \sqrt{\frac{2k}{b+\sqrt{b^2+r^2}}} \; . \tag{2.47}$$

If the kinetic energy exceeds the absolute value of the potential energy, a particle can escape from the gravitational field of the system. Imposing the physically-motivated limit $v < v_{\rm esc}$ it is possible to focus only on the particles trapped within the potential well.

2.5.2 Satellite's initial position in the phase-space

The phase-space position of the satellite at time t_i is one of the crucial aspects of the model. Reasonable values have to be chosen: a too large distance r_{sat} will reduce the number of orbits that the satellite has completed up to now. Consequently the effect of the tidal disruption would be underestimated. On the other hand, if the satellite were modelled as starting to fall from a too small distance, the high efficiency of the stripping process would quickly disrupt the satellite, with the net result of a smooth distribution and an overestimation of the tidal effects.

A similar analysis has to be carried out for the initial velocity of the satellite v_{sat}. The assumption of a value too close to the escape velocity of the system would increase the probability for the satellite to pass through the Galaxy halo without being tidally

perturbed. The consequence would be a underestimation of the dark matter velocity distribution in the phase-space.

2.5.3 Satellite's initial size and velocity dispersion

Estimates of the initial velocity dispersion and of the spatial extent of the subhalo are provided by the virial theorem

$$M_{vir} = \frac{r_{vir}\sigma_v^2}{G} \, , \tag{2.48}$$

and by the definition of virial mass

$$M_{vir} = \frac{4}{3}\pi\Delta_{vir}\rho_{crit}r_{vir}^3 \, , \tag{2.49}$$

where the virial overdensity Δ_{crit} is defined as the density relative to the mean density within r_{vir} relative to the critical density. The virial radius is the radius of a volume within which the mean density is Δ_{vir} times the critical density ρ_{crit} at that redshift (Bryan & Norman 1998), and where ρ_{crit} is

$$\rho_{crit} = \frac{3H^2(z)}{8\pi G} \, . \tag{2.50}$$

Equation (2.50) defines the density of the system relative to the critical density for the closure of the Universe. Assuming $r_{vir} = c\,\sigma_s$, with the concentration parameter $c = 10$ (Bullock et al. 2001; Benson 2005), it is possible to obtain credible estimates of the spatial and velocity dispersions in Eq. (2.46).

In conclusion, the technique we have developed allows us to quickly calculate the velocity distribution at any time at high spatial resolution at a certain location. By scanning the velocity-space, we can map out the sub-mpc-scale structure of the Milky Way's halo and obtain qualitative but useful insights into the likely signature of a halo merger event in a small terrestrial dark matter detector.

Chapter 3

Results for a single merger interaction

In this chapter we describe the results obtained using the numerical technique described in Chapter 2. The model simulates the interaction between a Milky Way-like galaxy and a single dark matter subhalo. Such an experiment is not intended to describe quantitatively the merger history of the Milky Way, but it can offer useful qualitative insights into the likely signature of a halo merger event in a terrestrial dark matter detector.

The Chapter is organised as follows: Section 3.1 is dedicated to the description of the dynamics of the interaction in phase-space, while Section 3.2 describes how the choice of the initial conditions has been made. The relevant results are presented in Section 3.3. We conclude with Section 3.4, where these results are summarised.

3.1 Motion of a system in the phase-space

To understand the distribution of the velocities of the dark matter particles composing a system and to have a more detailed picture of its evolution, it is useful to look at its representation in phase-space. Phase-space is a multi-dimensional space where all the possible states of a physical system are represented and each of them corresponds to a unique point. By “state”, we do not simply mean the positions of all the objects composing the system, but also the velocities, or momenta. In fact both the position and the momentum of the components of the system are necessary in order to determine

its future behaviour. When every state occupied by particles is plotted, its shape in this multidimensional space can elucidate qualities of the system that might not be obvious otherwise. It is also important to point out that the phase-space does not show the path of the particles composing the system, but rather a distribution of velocities and positions at a fixed time. This means that it changes and evolves with time, as each individual particle travels with time.

As discussed in Section 1.2.3.3, the WIMP direct detection rate depends directly on the local speed distribution. This quantity is defined as the number of particles per unit volume of the velocity space, once a particular spatial position has been selected. Before the formation of cosmic structure, the distribution of dark matter in the Universe was almost homogeneous. The phase-space evolution of the model we develop is presented in Figure 3.1-3.2. It is possible to visualise it in the phase-space as a 3-d sheet. After the gravitational collapse and the formation of a series of dark halos, the sheet would be folded up. The components of the system, both dark matter particles and stars, lie on the peaks of this folded surface. If we cut the 3-d sheet with a plane that represents the detector, then we can see that the velocity distribution function at that particular location will be characterised by velocity-peaks. An example of these peaks is presented in Figure 3.3a.

For our purposes we define the axis connecting the Sun and the centre of the Milky Way as x, and the Galactic plane as (x, y). At the beginning, the distribution of the particles is a vertical line because we initially assume that they are all located at $x = 1$. This distance identifies the Solar position in the Milky Way (8.5 kpc from the Galactic centre), and it also corresponds to the position where the grid of particles is set. In Figure 3.1a we plot the evolution of a subhalo, which fall into the Galactic halo on radial orbit, in the phase-space (x, v). The spatial and velocity dispersions of the subhalo are $\sigma_s \simeq 2.0\,\text{kpc}$ and $\sigma_v \simeq 60$ km s^{-1} respectively [see Equation (2.46)], corresponding to a mass of the order of $10^9\,M_\odot$. One spatial-unit corresponds to 8.5 kpc and one velocity-unit to 570 km s^{-1}. The scales of the plots are different to highlight the features present in the phase-space. The different colours are snapshots taken for a sequence of consecutive times: 0 Myr (red line), 15 (black), 30 (green), 45 (blue), 60 (violet) and 75 Myr (brown line). The aim of the plot is to give an overview

Fig. 3.1a: 0 Myr (red) $< t <$ 75 Myr(brown)

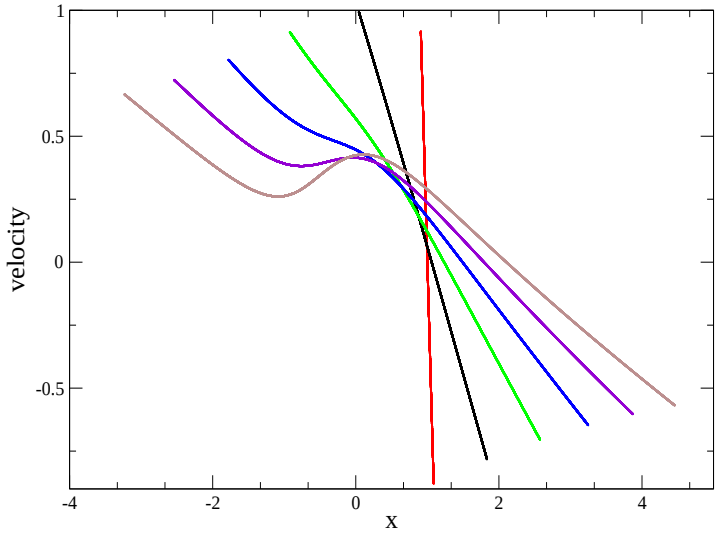

Fig. 3.1b: 150 Myr(black) $< t <$ 225 Myr(brown)

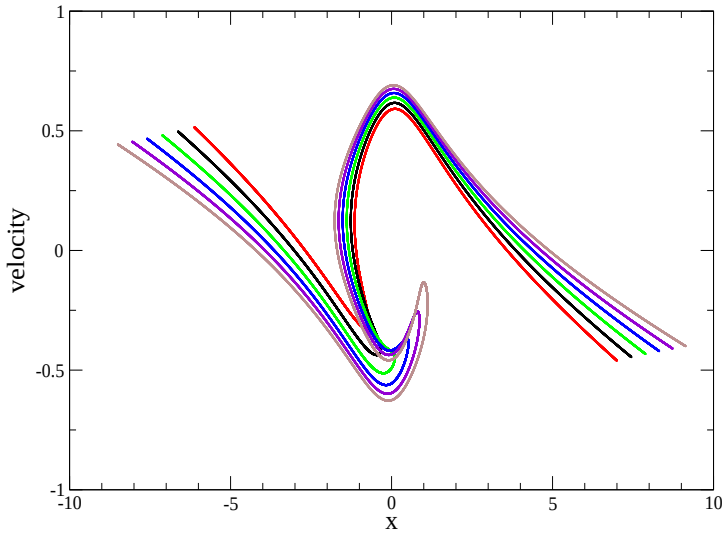

Figure 3.1: Series of snapshots showing the evolution of a satellite in the phase-space (v, x), where x is one of the spatial coordinates. Figure 3.1a shows the evolution from 0 Myr (red line) to 75 Myr (brown line), through four timesteps: 15 (black), 30 (green), 45 (blue) and 60 Myr (violet), while Figure 3.1b shows the evolution for 150 (black line), 165 (red), 180 (green), 195 (blue), 210 (violet) and 225 Myr (brown line). We consider a configuration composed by a satellite initially at $\mathbf{r}_{sat} = (-45, 0, 0)$ kpc, with velocity $v_{sat} \simeq 0$ km s^{-1} and initial phase-space distribution function given by Equation (2.46). The spatial and velocity dispersions are $\sigma_s \simeq 2.0$ kpc and $\sigma_v \simeq 60$ km s^{-1} respectively, corresponding to a mass of the order of $10^9\, M_\odot$. The scales of the plots are different to highlight the features present in the phase-space. One spatial-unit corresponds to 8.5 kpc, whereas $v = 0.1$ to 57 km s^{-1}.

of the evolution of the system for a short period of time. As a comparison, the satellite completes an orbit in about 900 Myr. As the system evolves, the distribution starts to bend and fold. The structures that we observe in Figure 3.1a are due to the deformation that the subhalo is suffering as it approaches the central region of the Galaxy. The evolution continues from 150 Myr (black line) to 225 Myr (brown) (Figure 3.1b), and at the last timestep the loop is almost complete. For a longer evolution time the system continues to follows a wrapped path. It is interesting to note that because each point in the phase-space lies on exactly one phase trajectory, these trajectories can never intersect. The presence of these complex structures is evident in Figure 3.2a and in Figure 3.2b, which describe respectively the distribution of the system after 0.8 Gyr and 13.6 Gyr. At these timesteps the subhalo has covered 1 and 15 orbits respectively. This last time corresponds to the age of the Universe (Komatsu et al. 2010).

3.2 Choice of the initial conditions

As discussed in Section 2.5, the initial conditions of the model are the position of the detector today, the evolution time of the system, the location of the subhalo in the phase-space at that time, the initial velocity dispersion of the merging satellite and its initial spatial extent. It can be useful to make a rough estimate of the typical values for some of these quantities, in particular for the quantities describing the internal properties of the subhalo. Substituting in Equations (2.48) - (2.49) the values already assumed for the concentration parameter ($c = 10$) and for the virial overdensity ($\Delta_{vir} \simeq 200$) (Bullock et al. 2001; Benson 2005a,b), the relations for the velocity dispersion σ_v and for the initial spatial extent of the merging system σ_s become

$$\begin{aligned} M_{vir} &= 1.50 \times 10^{7} (\sigma_s/\mathrm{m}) \, (\sigma_\mathrm{v}/\mathrm{ms}^{-1})^2 \quad \mathrm{kg} \, , \\ M_{vir} &= 8.25 \times 10^{-24} \, (\sigma_s/\mathrm{m})^3 \quad \mathrm{kg} \, . \end{aligned} \tag{3.1}$$

Values of σ_v and σ_s for the range of masses $10^6 M_\odot$-$10^{12} M_\odot$ are tabulated in Table 3.2.

These estimates are roughly in agreement with observations (Peñarrubia et al. 2008, Cenarro & Trujillo 2009) and they can be used as realistic initial conditions for the merging satellites.

Fig. 3.2a: $t \simeq 0.8$ Gyr

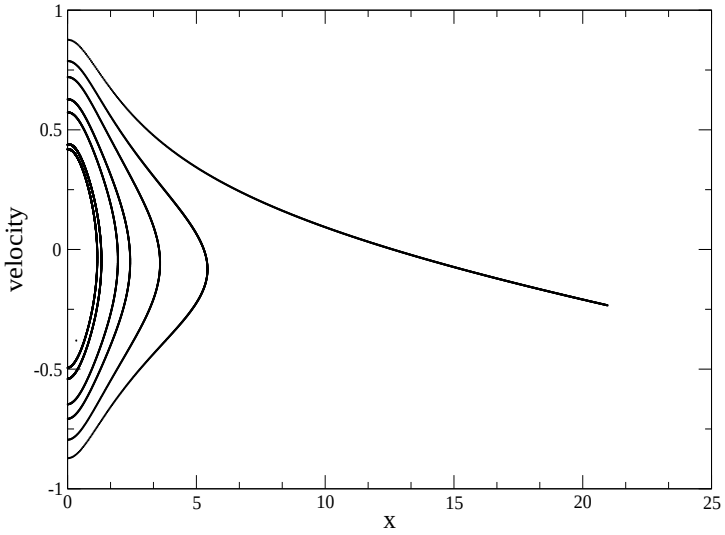

Fig. 3.2b: $t \simeq 13.6$ Gyr

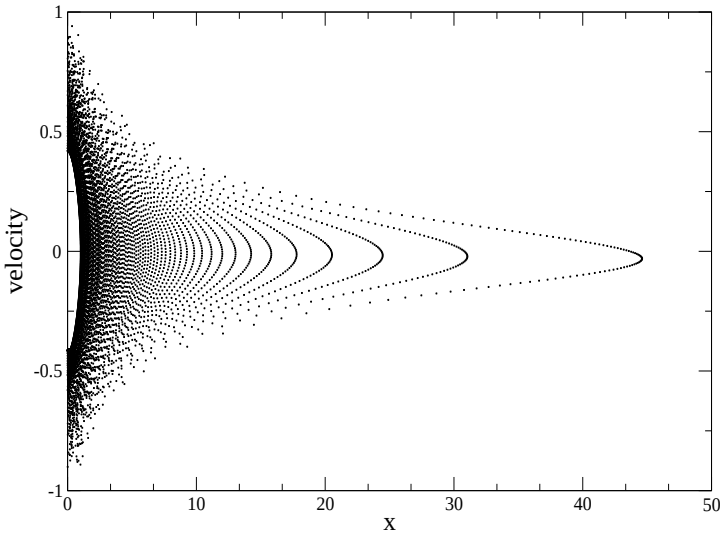

Figure 3.2: Series of snapshots showing the evolution of a satellite in the phase-space (v, x). Figure 3.2a: the configuration of the systems at 0.8 Gyr. Figure 3.2d: the configuration of the systems at 13.6 Gyr. We consider a configuration composed by a satellite initially at $\mathbf{r}_{sat} = (-45,\, 0,\, 0)$ kpc, with velocity $v_{sat} \simeq 0$ km s^{-1} and initial phase-space distribution function given by Equation (2.46). The spatial and velocity dispersions are $\sigma_s \simeq 2.0$ kpc and $\sigma_v \simeq 60$ km s^{-1} respectively, corresponding to a mass of the order of $10^9\, M_\odot$. The scales of the plots are different to highlight the features present in the phase-space. One spatial-unit corresponds to 8.5 kpc, whereas $v = 0.1$ to 57 km s^{-1}.

$M_{vir}(\mathrm{M}_\odot)$	$\sigma_v(\mathrm{km\,s^{-1}})$	$\sigma_s(\mathrm{pc})$
10^{10}	122.5	4.0×10^3
10^9	56.8	1.8×10^3
10^8	26.4	860
10^7	12.3	400
10^6	5.7	185

Table 3.1: Three-dimensional velocity dispersion and spatial dispersion of merging satellites with a range of masses 10^6 - $10^{12} M_\odot$, calculated using Equation (3.1).

3.3 Results

3.3.1 Velocity distribution

We first consider a satellite with the initial conditions described at the end of Section 3.2 and initial phase-space distribution function given by Equation (2.46). The spatial and velocity dispersions are respectively $\sigma_s \simeq 2.0\,\mathrm{kpc}$ and $\sigma_v \simeq 60$ km s^{-1}, corresponding to a mass of the order of $10^9\, M_\odot$. These parameters are chosen to describe a cold and concentrated satellite, as expected in reality. The system merges into the parent galaxy on a radial orbit along x from a distance $\mathbf{r}_{sat} = (-45,\, 0,\, 0)$ kpc. By using the reverse AA evolution technique presented in Chapter 2, the present-day velocity distribution function at the detector's position, $r_0 \simeq 8.5$ kpc, can be calculated.

Figures 3.3 - 3.4 present the distribution function of v_x at four increasing times: 1.4, 7.2, 13.6 and $136\,\mathrm{Gyr}$. These four timesteps are chosen as an illustrative representation of the evolutionary history of the system, from an early time (Figure 3.3a), after only one and a half orbit around the Galactic centre, to a late time, that describes the satellite in the distant future (Figure 3.4b) and corresponds to 150 orbits. The other two timesteps correspond to a number of orbits equal to 8 (Figure 3.3b) and 15 (Figure 3.4a) respectively.

In Figure 3.3a two peaks are evident: one has positive speed, the other negative. Both of them are produced by groups of particles passing through the detector position. The most prominent is due to the passage of the main body of the satellite, the smaller is part of the tail, a remnant of a previous orbit. From the distribution of the peaks it is possible to get an idea of the current stage of the evolution and of the history of its interaction. At this early stage it is easy to conclude that the satellite, which

Figure 3.3a: $t \simeq 1.4$ Gyr

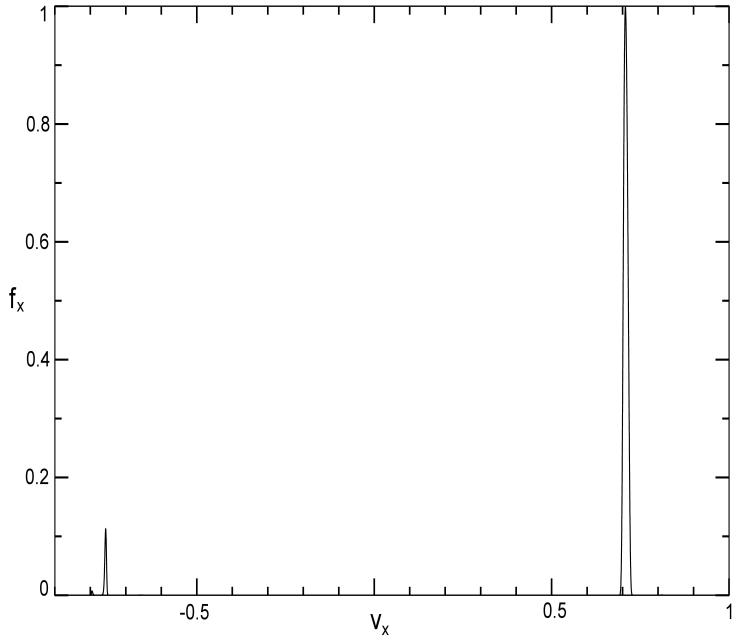

Figure 3.3b: $t \simeq 7.2$ Gyr

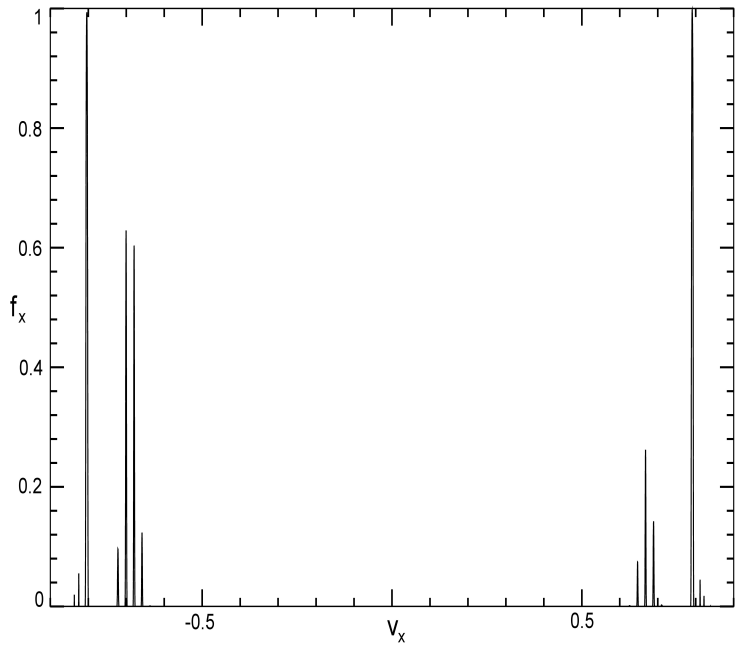

Figure 3.3: The distribution function of the velocity v_x at the Solar position. Two evolution times have been considered: $t \simeq 1.4$ Gyr (Figure 3.3a), $t \simeq 7.2$ Gyr (Figure 3.3b). The initial conditions are the same as used in Figure 3.1. One velocity-unit corresponds to 570 km s^{-1}.

Figure 3.4a: $t \simeq 13.6$ Gyr

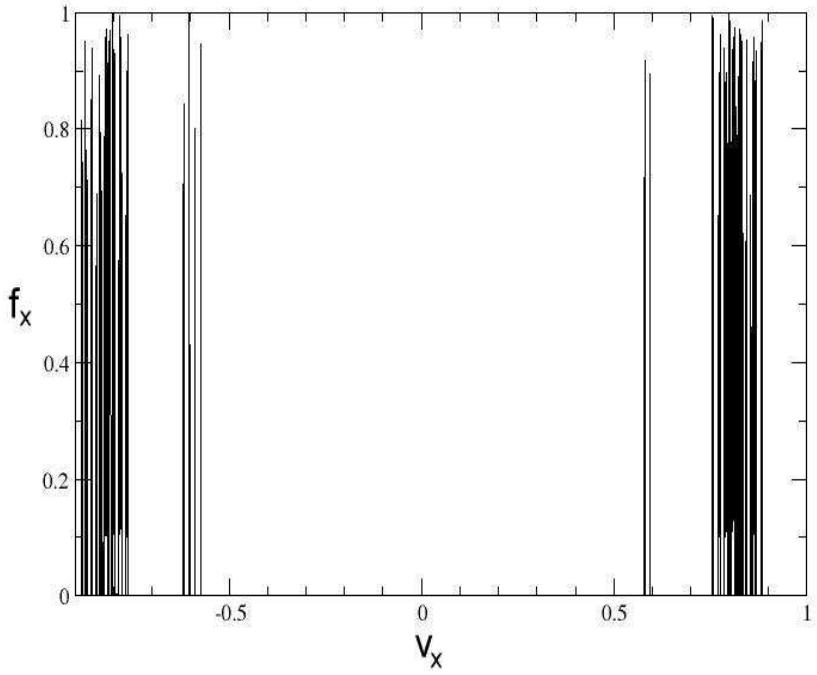

Figure 3.4b: $t \simeq 136$ Gyr

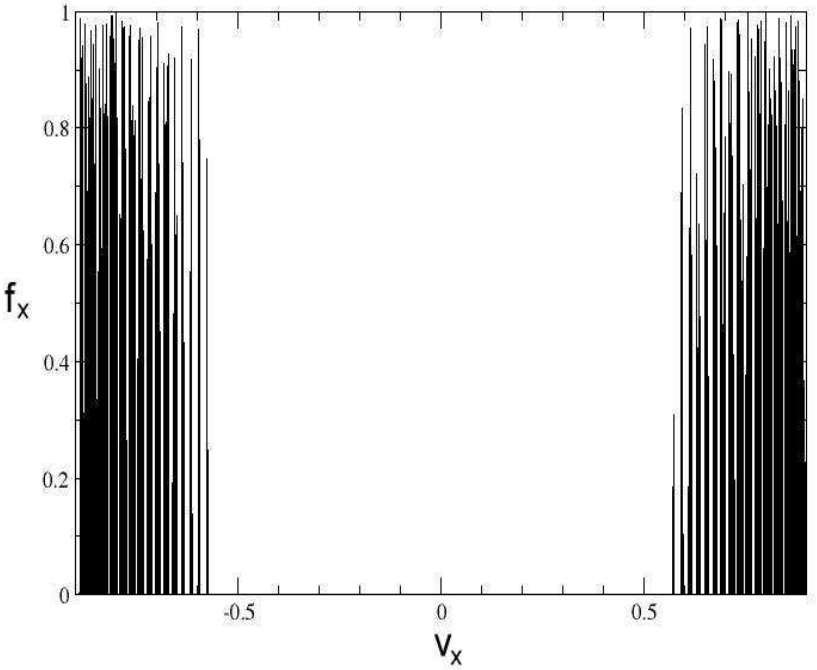

Figure 3.4: The distribution function of the velocity v_x at the Solar position. Two evolution times have been considered: $t \simeq 13.6$ Gyr (Figure 3.4a) and $t \simeq 136$ Gyr (Figure 3.4b). The initial conditions are the same as used in Figure 3.1. One velocity-unit corresponds to 570 km s^{-1}.

has performed only a few orbits around the Galactic centre, is still fairly coherent. Nevertheless, the disruption due to the action of phase mixing starts to be effective, as demonstrated by the presence of peak at negative v_x.

The evolution of the merger after the first timestep, until the system reaches the age of the Milky Way, is shown in Figures 3.3b and 3.4a. As expected, the satellite gets strongly disrupted under the action of tidal forces and the particles spread out in phase-space. As a consequence, a large number of streams start to overlap and the velocity distribution is composed of an increasing number of peaks. Figure 3.5 zooms into the dense forest of peaks present in the region $0.55 < v_x < 0.9$ of Figure 3.4a. The star-like points correspond to the particles of the simulation, that was performed using the backward technique. To highlight the structure of the peaks a logarithmic scale on the y-axis has been assumed. This set up allows us to highlight that the peaks are not forming a single, dense forest, but they are concentrated around particular values of v_x. Each of these values describes the passage of a stream of particles in the detector position. These streams has been generated by the gravitational disruption of the satellite which is falling into the Galaxy.

Finally, the configuration of the satellite does not change drastically if the evolution time is increased by an order of magnitude. In Figure 3.4d the system is 136 Gyr old, but the distribution of the peaks is not completely homogeneous, even at a stage of the evolution when the system is expected to be almost completely relaxed.

3.3.2 Forward evolution: phase-space distribution

To illustrate the power of the reverse AA evolution technique, we carried out simulations using the more conventional approach of evolving a satellite composed of 10^5 particles forward in time. The system has the same initial conditions as the configuration assumed for the backwards model: it starts to fall into the Milky Way from $\mathbf{r}_{sat} = (-45, 0, 0)$ kpc, with zero initial velocity. It has a spatial dispersion of $\simeq 2.0$ kpc and a velocity dispersion of $\simeq 60$ km s^{-1}, corresponding to a mass of $M = 10^9\, M_\odot$. Figures 3.6 and 3.7 show the histograms of the speed distribution of the subhalo calculated at evolution times of $\simeq 1.4$ Gyr, that corresponds to one and a half orbit around the Galactic centre, and $\simeq 2.5$ Gyr ($\simeq 3$ orbits). To understand the differ-

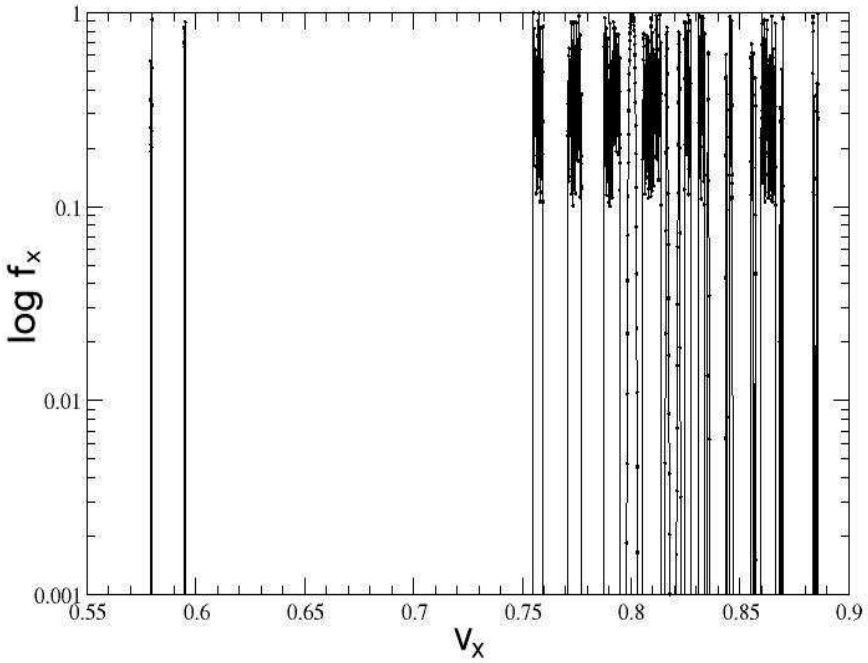

Figure 3.5: Zoom in the region $0.55 < v_x < 0.9$ of Figure 3.4a. The Figure shows the logarithm of the distribution function of the velocity v_x at the Solar position at $t \simeq 13.6$ Gyr. The initial conditions are the same as used in Figure 3.1. One velocity-unit corresponds to 570 km s^{-1}. The stars corresponds to particles of the simulation performed using the backward technique.

ence between the techniques it is useful to compare Figures 3.3a and 3.6. The systems have the same age, $\simeq 1.4$ Gyr, and they evolve from the same initial conditions. The only difference between them is that Figure 3.3a has been obtained performing the backwards technique, while Figure 3.6 using a forward one. As expected, they present the same peaks, but since the vast majority of particles in the forward evolution end up nowhere near the detector, the sampling of the peaks in this case is extremely poor. This is the reason why the peaks visible in Figure 3.6 are composed only of few particles, out of the 10^5 particles that were composing the satellite at the beginning of the evolution. This example provides a simple illustration that forward evolution is not the best technique for calculating the velocity distribution at a single point. The problem becomes even more severe at later times, as is possible to note in Figure 3.7. The particles now populate a larger volume of phase-space, making reverse techniques a very powerful instrument to investigate the ultra-fine structure of dark matter at a precise point in the phase-space. The comparison of the results obtained using the forward

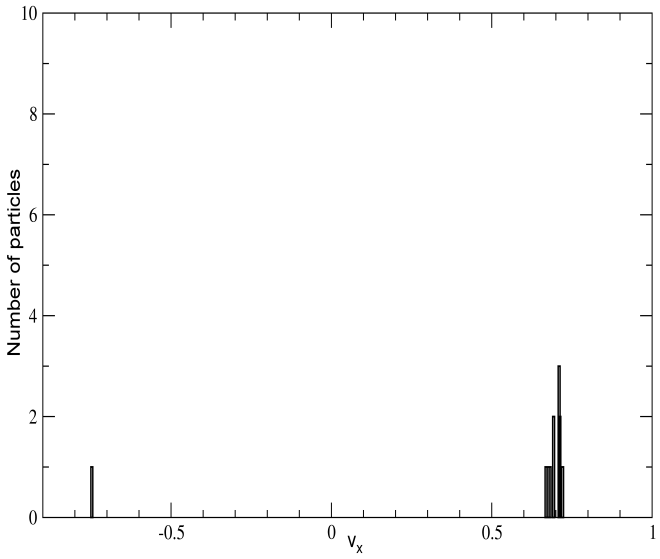

Figure 3.6: Histogram showing the distribution of the x-component of the velocity for a satellite with the same configuration as Figure 3.3, calculated after an evolution time $t \simeq 1.4\,\mathrm{Gyr}$ by evolving the coordinates of 10^5 particles forward in time. One velocity-unit corresponds to 570 km s^{-1}. The plot can be compared to Figure 3.3a, which describes the same system using a backward model. One velocity-unit corresponds to 570 km s^{-1}.

and the backward techniques clarifies the different philosophies behind the two types of technique: the forward evolution is very useful if we want to have a global picture of the distribution of the particles in the whole phase-space, but it becomes useless if we are interested in analysing the dynamics of the system at a precise point.

Nevertheless, the forward evolution can provide complementary information by showing the disruption process to which the satellite is subjected. Figure 3.8 is composed of thirteen snapshots at different timesteps of a satellite composed by 10^5 particles, and it shows the distribution of the selected particles from the beginning of the merger (black points) to a time of 882 Myr (purple), which corresponds to the time at which an orbit has been almost completed. The plot highlights the distortion that the subhalo suffers during a whole orbit, due to the presence of strong tidal forces. The dense and compact object present at the beginning of the simulation starts to be disrupted very early by the strong gravitational field of the Galaxy. This is evident because the range of speeds of the particles composing the system starts to increase: even if the subhalo is compact, the tidal forces acting on it are able to stretch their distribution. The particles composing the front part of the subhalo will be accelerated more than those in the tail, increasing the range of speeds the particles have. This happens as soon as it starts to reach the internal part of the Galaxy. The strength of the gravitational force decreases

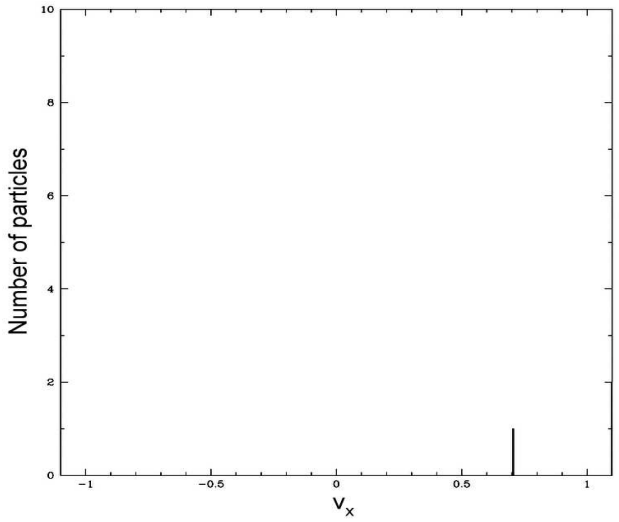

Figure 3.7: As Figure 3.6, for $t \simeq 2.5\,\mathrm{Gyr}$.

once the subhalo start to leave the central region, but the net effect at the end of the first orbit is the production of a more dispersed configuration.

Figure 3.9 shows the distribution in the (x, v_x) space of a satellite composed of 10^5 particles after 2.5 Gyr ($\simeq 3$ orbits around the Galactic centre) from the beginning of the interaction. The initial conditions are the same as we assumed for the previous simulations. The plot highlights the strength of the disruptive process the subhalo is subjected to: at this stage of the evolution the original satellite has been already disrupted by tidal forces and phase mixing and the distribution of the particles is almost homogeneous along the radial orbit the satellite is covering. If we focus on the detector's position, which in the plot corresponds to $x = 1$, the peak of Figure 3.7 arise from particles that are coming only from the regions labelled with circles. The plot illustrates once more how a classical forward-numerical simulation is not appropriate for our purposes because after a few orbits only a very small number of particles is located at a specific position. This number decreases as the system evolves, and the possibility to observe features in the velocity distribution rapidly tends to zero. To have a significant number of particles contributing to the velocity distribution in the detector position we would have to increase the total number of particles of the simulation enormously, with a consequent huge increase of the computational time required.

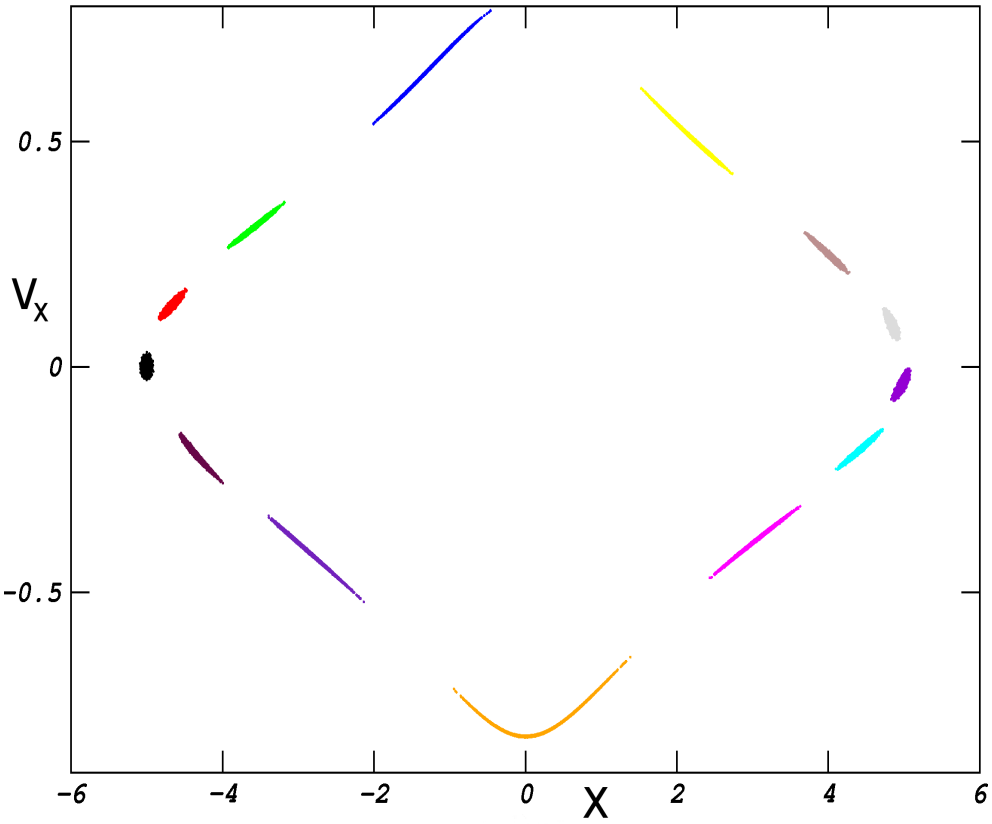

Figure 3.8: Compilation of thirteen simulations reproducing the evolution of the distribution of a subhalo. The thirteen snapshots describe the evolution of the subhalo in the phase-space (x, v_x) during a single orbit around the centre of the Galaxy. The evolution is represented from the beginning of the merger ($t = 0$ yr, black points) to an age of 882 Myr (purple), corresponding to the time at which an orbit is almost complete. The system, described by an initial velocity dispersion $\sigma_v \simeq 60$ km s^{-1} and an internal spatial dispersion $\sigma_s \simeq 2.0$ kpc, starts to fall into the Milky Way's dark halo from a distance $\mathbf{r}_{sat} = (-45, 0, 0)$ kpc with zero velocity. These are the same initial conditions assumed in the previous simulations. One spatial-unit corresponds to 8.5 kpc, whereas $v = 0.1$ to 57 km s^{-1}.

3.3.3 Evolution of the interaction

A further indication of the flexibility of the backwards approach is provided by Figure 3.10. This multiple figure shows the dependence of the results on the two important driving parameters, the internal velocity dispersion of the merging sub-halo, and its initial orbit. Each panel depicts the simulated phase-space velocity distribution in a terrestrial detector after 13.6 Gyr for a different set of initial conditions: $\sigma_v = 6$ km s^{-1} for the top row, $\sigma_v = 60$ km s^{-1} for the middle and $\sigma_v = 600$ km s^{-1} for the bottom one, while from the left to the right we impose a change in the type of orbit performed by the satellite, moving from a circular to a radial orbit. The three values of the three-dimensional velocity dispersion ($\sigma_v = 6, 60, 600$ km s^{-1}) roughly correspond to sub-halos of mass $\simeq 10^6 M_\odot$, $\simeq 10^9 M_\odot$ and $\simeq 10^{12} M_\odot$ respectively, and they

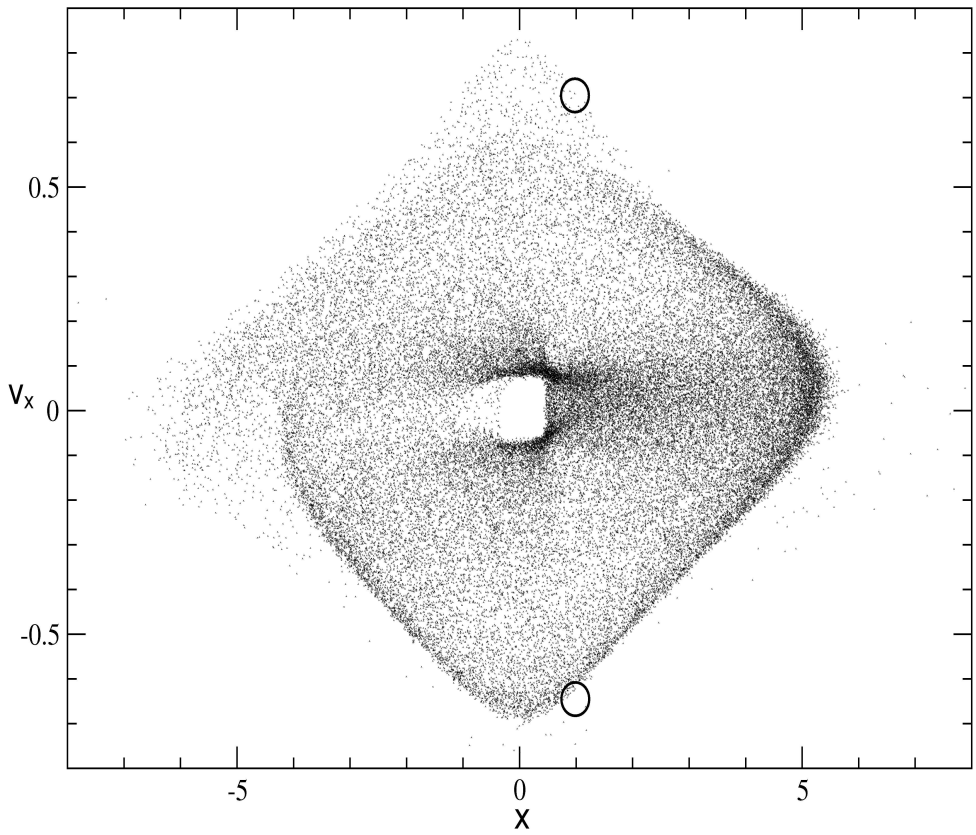

Figure 3.9: Configuration of the satellite in (x, v_x) after 2.5 Gyr. The same initial conditions as Figure 3.3a have been assumed. Two black circles pinpoint the regions corresponding to the origin of the peaks in Figure 3.7. One spatial-unit corresponds to 8.5 kpc, whereas $v = 0.1$ to 57 km s^{-1}.

have been chosen to represent a wide range of systems. The spatial dispersion is the same for every simulation: $\sigma_s \simeq 2.0\,$kpc. It is interesting to note that because of the analytical nature of the orbit integration, the time necessary to perform this calculation was the same as that for a shorter timescale, with no loss of precision in the results. As this figure illustrates, although there are interesting differences in the details as these parameters are varied, the generic properties of multiple discrete peaks remains. The distribution function of the component of the speed in the direction of the merger depends on the merging halo's parameters: a high velocity dispersion ($\simeq 600$ km s^{-1}) creates more peaks in the velocity distribution because the subhalo gets disrupted by the gravitational potential of the Galaxy more quickly. The velocity dispersion is in fact a measure of the amount of random motion of a system. A high value corresponds to a "hot" system, while a system with the low value of σ_v is "cold" and less stripped by the Milky Way. The result, in terms of the velocity distribution function, is the presence of a smaller number of peaks. Regarding the timescale of the disruptive process, it gets longer for denser satellites. It is also evident that the time required for the satellite to

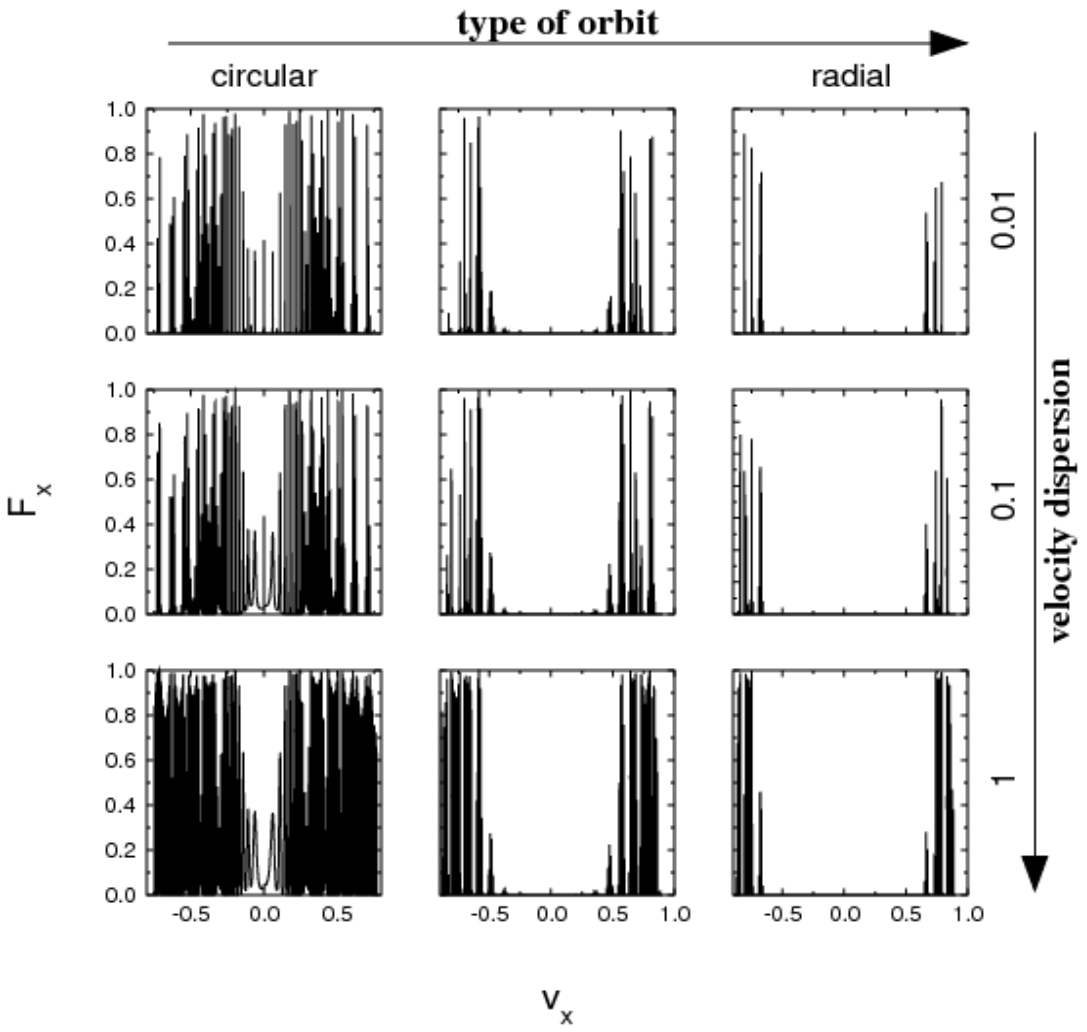

Figure 3.10: The distribution function of the component of the speed in the direction of the merger of a $10^9\,M_\odot$ halo as a function of its velocity dispersion and of the orbit it performs in the Galaxy potential. A velocity dispersion $\sigma_v = 0.01$ corresponds to 6 km s^{-1}, $\sigma_v = 0.1$ to 60 km s^{-1} and $\sigma_v = 1.0$ to 600 km s^{-1}. The nine snapshots depict the system at $t \simeq 13.6\,$Gyr. The orbit of the dark matter halo is varied moving from the left (circular orbit) to the right (radial). On the y-axis an increase (from the top to the bottom) of the velocity dispersions is considered. One velocity-unit corresponds to 570 km s^{-1}.

be disrupted is shorter when the satellite moves on a circular orbit and that in this case the distribution is smoother than the one generated by a satellite which in moving on a radial orbit.

A peculiar feature, pronounced in particular for the systems on radial orbit, is the absence of peaks at low velocities. This can be understood with an analysis of the orbit the satellite is performing. When the subhalo is on a radial orbit, almost all the velocity is concentrated along the x-component because x is the preferential direction for the motion. Consequently, the peaks are in areas where the value of v_x is high. For a circular orbit this argument is not valid anymore. In this case the velocities along y

and z are larger than the one along x, which is mainly due to the internal motion of the satellite. As a consequence the internal region of the plot starts to be populated, as visible in the left column in Figure 3.10.

The main conclusion that we can draw is that even at late times (up to $13.6\,\mathrm{Gyr}$), when the particles have spread out through phase-space, the velocity-space distribution function is still characterised by discrete, concentrated peaks. This demonstrates that the ultra-fine structure of a system takes a long time to become totally disrupted and that the existence of substructures for a system as old as the Milky Way is still a definite possibility. More generally, the analysis of these sorts of features can provide important information about the history and the properties of the merging satellite.

3.3.4 Diagnostic for directional detection

This model is not intended to predict quantitatively the experimental signal that a terrestrial detector would observe, but we can take the qualitative analysis one step further by considering the physical quantities that are most relevant for such experiments, particularly those with directional sensitivity. A useful diagnostic is provided by the speed of dark matter particles as a function of the angle, θ, at which they impinge on the detector, measured relative to the direction of Solar motion in the Milky Way. The cosine of this angle is

$$\cos\theta = \frac{v_y}{v}\,. \tag{3.2}$$

In Figure 3.11 these quantities are plotted at four different stages of the evolution of the system: 1.4 (Figure 3.11a), 7.2 (Figure 3.11b), 13.6 (Figure 3.11c) and 136 Gyr (Figure 3.11d). The plot shows the phase-space density, plotted as a function of the speed and the angle defined in Equation (3.2). In the early stages, represented by Figure 3.11a and 3.11b, clear features are present. They are due to the streams of particles that originate during the first few orbits performed by the subhalo. These four timesteps correspond to 1 and a half, 8, 15, 150 orbits respectively. At a later time (Figure 3.11c) the situation is more complex: although the dark matter particles are quite well spread through the parameter space, it is apparent that even at this late time there is a significant amount of structure. A series of overdensities overlap to

form a sort of "shell" structure. These features may allow the merging subhalo to be detected, and might even ultimately be used to reconstruct its properties. The result is in agreement with what has been deduced in Section 3.3.1 and 3.3.3 through the analysis of the evolution of the satellite in phase-space.

Figure 3.11a: $t \simeq 1.4$ Gyr

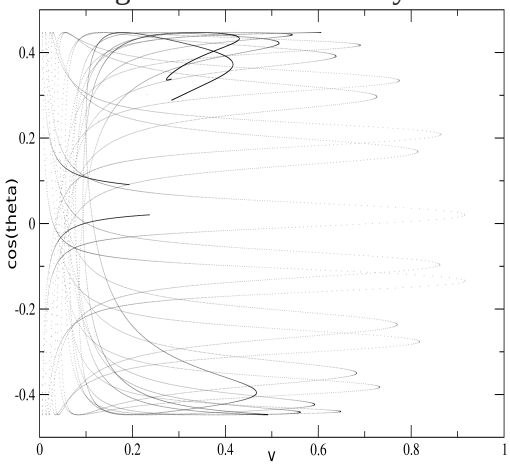

Figure 3.11b: $t \simeq 7.2$ Gyr

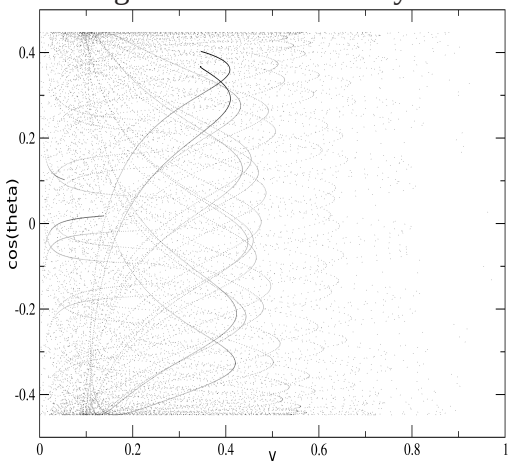

Figure 3.11c: $t \simeq 13.6$ Gyr

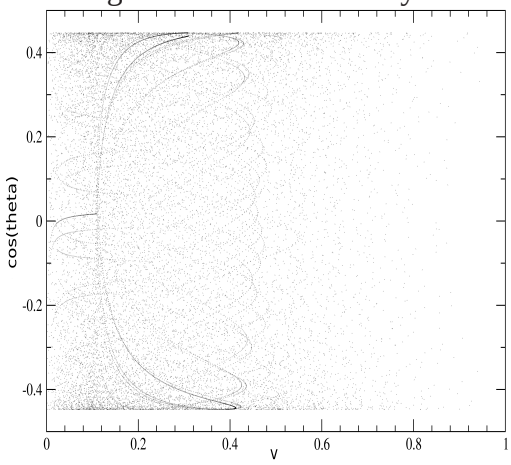

Figure 3.11d: $t \simeq 136$ Gyr

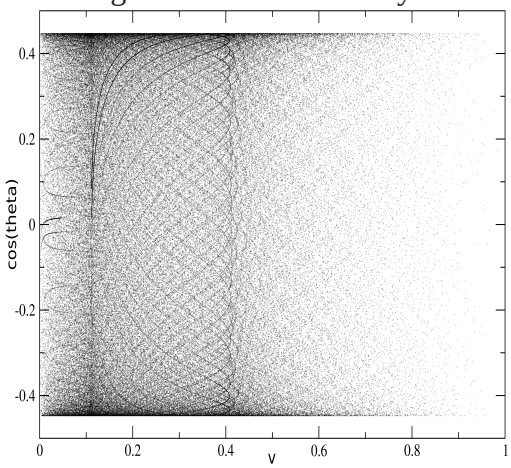

Figure 3.11: The speed and angle (with respect to the direction of Solar motion) of the particles of a satellite impinging on a terrestrial dark matter detector at 1.4 (Figure 3.11a), 7.2 (Figure 3.11b), 13.6 (Figure 3.11c) and 136 Gyr (Figure 3.11d). The initial condition for each of the four simulations are: $\mathbf{r}_{sat} = (-45,\, 0,\, 0)$ kpc, $v_{sat} = 0$ km s^{-1}, $\sigma_v = 60$ km s^{-1}, $\sigma_s \simeq 2.0$ kpc. The satellite is falling into the Galactic halo on radial orbit. $v = 0.1$ corresponds to 57 km s^{-1}.

The situation changes at a late stage of the evolution, as shown in Figure 3.11d. If we consider particles with a certain speed, they will be almost completely spread out. This can be interpreted as the superposition of a considerable number of streams. Nevertheless, although the dark matter particles are spread out through the parameter space, it is evident looking at Figure 3.11d that even at this late time they are inclined to assemble

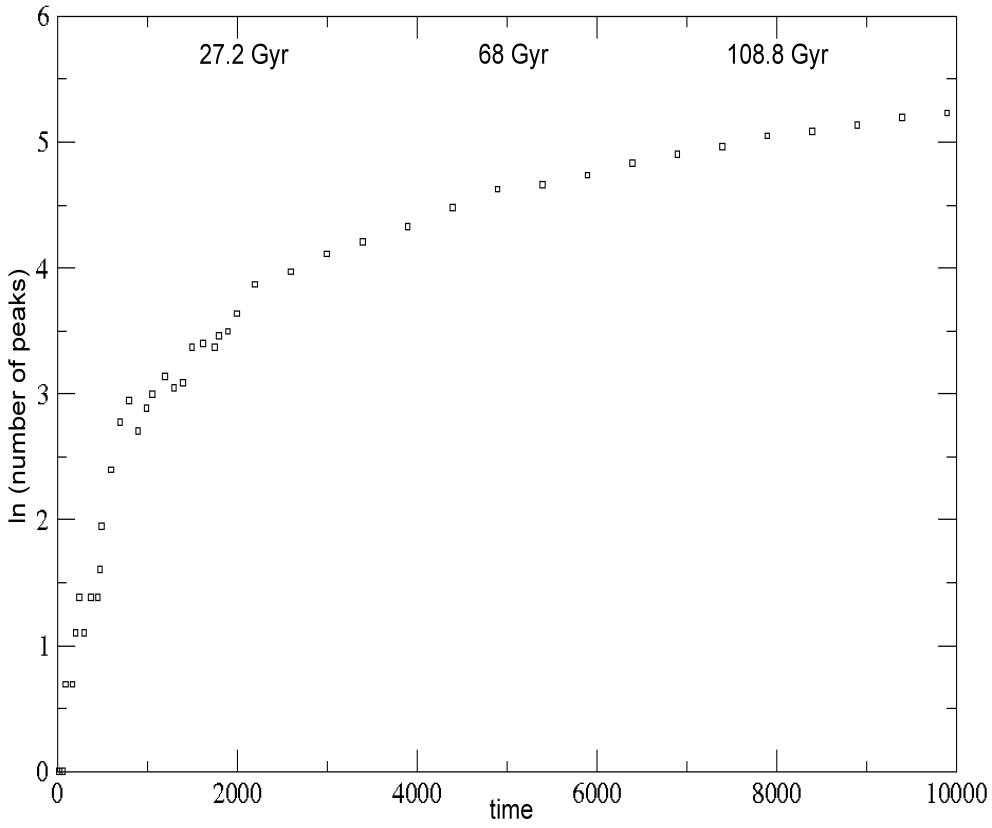

Figure 3.12: The logarithmic evolution of the number of peaks from the merger of a single subhalo. The plot presents the evolution of the system from the beginning of the merger up to 136 Gyr. The initial conditions are the same as Figure 3.11. One time-unit corresponds to 13.6 Myr.

around particular values of the velocity, following a shell configuration. The same type of overdensities is present for a satellite moving on circular orbit around the Galaxy.

3.3.5 Evolution of the number of substructures

In this Section we analyse the evolution of the number of peaks present in the velocity distribution function (Figure 3.12). The simulation was run for a series of timesteps, to cover the whole evolution of a subhalo from the beginning of the merger to a later stage, up to 136 Gyr. Different sets of initial conditions have been considered: varying the velocity dispersion, as well as the type of orbit. The behaviour of this quantity with time is found to be qualitatively the same for all the different configurations that have been considered: changes in the initial conditions do not influence the general progression of the merger process. At the beginning of the evolution the number of peaks grows very quickly after each orbit. It is possible to explain this behaviour in terms of the tidal interactions and the phase mixing which act on the satellite. After

each orbit the satellite is more disrupted. As a consequence more streams start to be present and the number of peaks increases very rapidly. This behaviour continues until the system reaches an age of about 30 Gyr, more than twice the age of the Universe. Finally, if we look at the long term behaviour, when the satellite has been completely disrupted and the system is almost relaxed, it tends, as expected, to a constant value.

3.3.6 Multiple merger systems

In reality the Galactic halo is made up of multiple merger events, and the velocity distribution will look more complex than that shown in Figure 3.11. We will address this issue in more detail in Chapter 4, but as an initial indicator, Figure 3.13 crudely models this effect by adding the results obtained for a series of one hundred single interactions. To increase the realism of the description we assumed that the subhalos were falling into the Milky Way at different random times and on different orbits, from radial, with the subhalo falling from a distance $\mathbf{r}_{sat} = (-45,\, 0,\, 0)$ kpc, to circular. We also assumed different velocity dispersions and spatial extents, to represent subhalos with a wide range of different properties. For the velocity dispersion three values are considered: 6, 60 and 600 km s^{-1}. The infall velocity of the subhalos, v_{sat} is always taken to be zero and the spatial dispersion 2.0 kpc. Although multiple-merger events clearly lead to a configuration with more streams, if we compare this configuration with Figure 3.11 we can still reach the conclusion obtained for a single-event system: dark matter particles are not spread enough through the phase-space to produce a completely smooth velocity distribution. Focusing on the visible features, the presence of strong horizontal structures in this diagnostic figure is very clear. They arise from the constraint imposed by the cut-off at the escape speed on the subhalos composing the simulation. These horizontal features suggests that much information might be gleaned about the merger history of the Milky Way halo from the analysis of these features, once observed by future terrestrial dark matter detectors. The presence of these interesting features in the velocity distribution motivates the next step in this project, which aims to place these mergers in a full cosmological contest. This refinement is fully described in Chapter 4, and the results presented in Chapter 5.

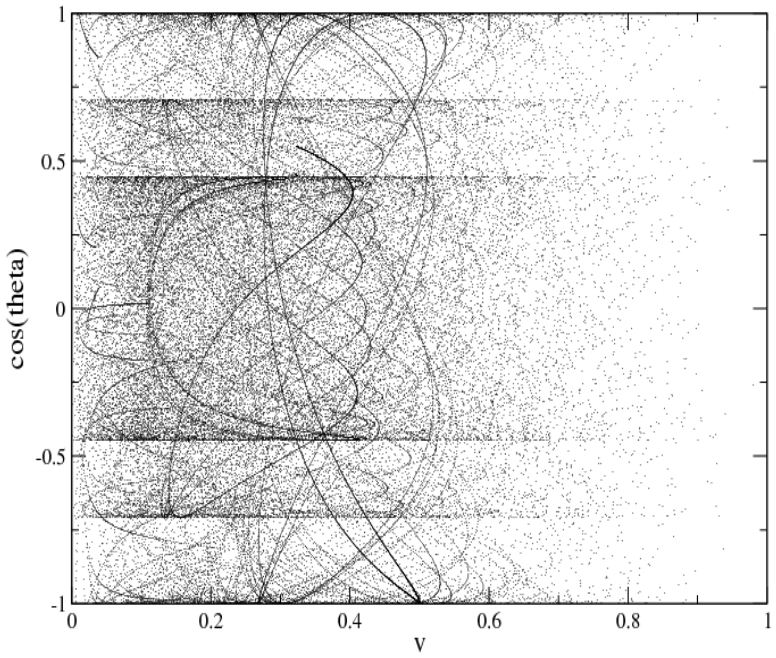

Figure 3.13: The dark matter speed versus angle plot, as in Figure 3.11, showing the consequences of the merger of one hundred subhalos merging into a Milky-Way-like potential well from a range of distances and directions. The initial conditions are the same as in Figure 3.11. One velocity-unit corresponds to 570 km s^{-1}.

3.4 Summary

We have studied the distribution of particles resulting from the merger of a satellite with a parent galaxy described by an isochrone potential. The dynamics of the merger can be calculated remarkably simply, and the satellite can be evolved forwards or backwards in time analytically using action-angle variables. This simplicity allows us to quickly and accurately calculate the velocity distribution at any time at arbitrarily high spatial resolution, which is vital to understand the mpc-scale structure of the Milky Way's halo probed by terrestrial dark matter detectors. We find that, even at late times (up to 13.6 Gyr), when the particles are distributed almost homogeneously through phase-space, the velocity-space distribution function is characterised by discrete peaks (Figure 3.10).

As a diagnostic for dark matter directional detection we have studied the angle at which particles impinge on the detector, measured relative to the direction of Solar motion in the Milky Way [Equation (3.2)]. In agreement with Stiff & Widrow (2003), we find that this diagnostic quantity contains significant structure imprinted by the original merging sub-halo (see Figure 3.11). Stiff & Widrow used a more realistic Milky Way potential

but only integrated the orbits very approximately, while we used a more approximate potential but treated the integration exactly. The fact that the presence of discrete peaks occurs with both approximations adds weight to the tentative conclusion that the features are generic. Although the situation becomes more complex when we consider a halo built up from multiple mergers over the lifetime of the Galaxy, as apparent in Figure 3.13, the evidence suggests that significant amounts of fine-grained structure persist. This could have an impact on the detectability of a particular merging sub-halo, and might even ultimately be used to reconstruct its origins. In conclusion, although the potential is simplified in order to be tractable analytically, the resulting features should be generic in that the number of streams is set by the wrapping of the satellite around the Galaxy, which does not depend in detail on the shape of the potential. Once again, it is the common properties of this ultra-high-resolution simulation in a less realistic potential and lower-resolution simulations in more realistic potentials that gives confidence as to the generic nature of the results.

Chapter 4

Model for the formation of a Milky Way-like dark matter halo

In Chapter 3 we focused our attention on the evolution of the dark matter velocity distribution from a single merger event in an ideal detector. In reality, the formation history of the Milky Way is characterised by the continual infall of a large number of subhalos, which leads to a scenario with a very complex distribution of dark matter, characterised by the presence of many more streams. This motivated us to refine the model described in Chapter 2, assuming a realistic description of the hierarchical growth which leads the formation of a Milky Way-like system.

As both galaxy formation models (Kauffmann et al. 1993; Cole et al. 1994) and N-body simulations (Springel et al. 2005, Boylan-Kolchin et al. 2009) suggest, galaxies formed though a continuous hierarchical process. To take this into account we insert the previous simple model into a cosmological context, combining a merger tree, which describes the formation of a Milky Way-like halo through hierarchical merging, with the model described in Chapter 2. This allows us to produce a complete and more realistic treatment of the merger history of the Galactic halo.

This Chapter is organised as follows. Section 4.1 explains what a merger tree is and what information it provides, while we develop the technique in Section 4.2. The analysis of the choice of the initial conditions of the model is finally described in Section 4.3.

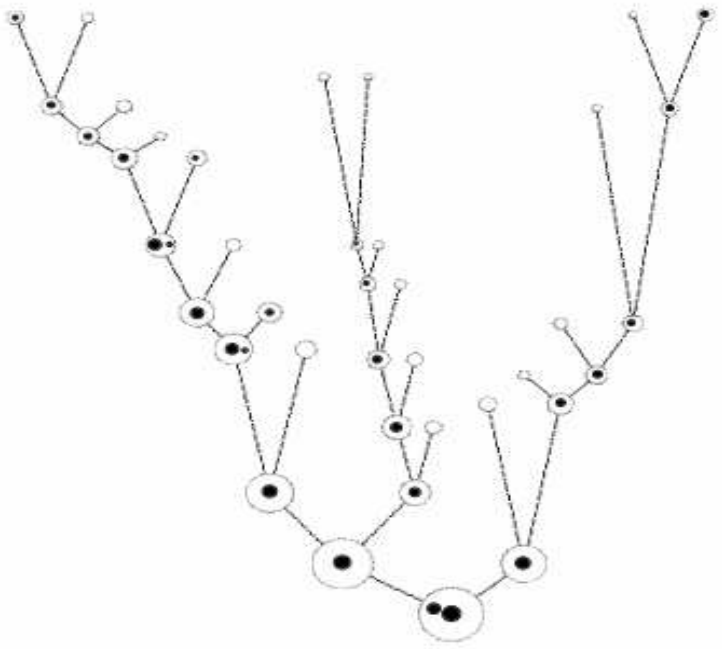

Figure 4.1: An illustration of the merger-tree history of a galaxy in the cold dark matter cosmology. Time increases from top (small branches) to bottom (trunk). A galaxy is formed by the sequential merger of systems (white circles). The different size of the circles represents the range of masses of the merging structures and the black circles represent the presence of a black hole. Credit: Marta Volonteri (University of Michigan).

4.1 Merger tree

In hierarchical models of structure formation, such as ΛCDM, the formation of a dark matter halo through accretion and repeated mergers of smaller structures can be described by a merger tree (Lacey & Cole 1993). It represents the hierarchical growth of the halo and it gives information on its evolution and on the properties of its components. Figure 4.1 shows the visualisation of the merger tree of a generic dark matter halo.

In order to model the Milky Way for this project, Andrew Benson (Caltech) kindly created 100 random merger trees for us. The trees have been generated using a semi-analytic method based on the assumption of the following cosmological parameters: $\Omega_0 = 0.25$, $\Lambda_0 = 0.75$, $\Omega_b = 0.045$, $h_0 = 0.73$ and $\sigma_8 = 0.9$. The details of the Monte-Carlo algorithm that has been used to generate the merger trees, which go beyond the focus of this Thesis, can be found in Cole et al. (2000) and Parkinson et al. (2008). The large number of trees is motivated by the degeneracy of the problem. In fact, a

particular final system can be obtained from different initial configurations and from different evolutions, and the properties of the galaxies that are hosted in the centre of the system presumably depend on the details of the evolution. All merger trees have 100 timesteps in $\log(\mathrm{a})$ from $a_0 = 1$ to $a = 0.05$, where a is the scale factor

$$\frac{a}{a_0} = \frac{1}{1+z}\,, \tag{4.1}$$

with a_0 the scale factor today. The value of the scale factor today, $a_0 = 1$, corresponds to $z_0 = 0$, while $a = 0.05$ corresponds to $z = 19$. All the final halos have mass of $10^{12} M_\odot$ at z_0. The information provided by the merger trees required for this modelling are:

- The mass of each merging subhalo, in units of $M_\odot$. The mass resolution of this set of trees is $10^8 M_\odot$.
- The scale factor a at which each subhalo falls into the main progenitor. The time at which the merger takes place is defined as the instant when the centre of the smaller halo crosses the virial radius of the parent halo.
- The value, at each timestep, of the virial overdensity, Δ_{vir}. This quantity has already been defined in Section 2.5.3.

4.2 The refined version of the model

The principal steps of this full modelling process are:

1. Pick a merger tree that gives a realistic representation of a Milky Way-like system.
2. Calculate the initial conditions for each subhalo in the merger tree.
3. Evaluate the velocity distribution, normalised to the mass of the subhalos, observable within the detector for each subhalo, using the model developed in Chapter 2.
4. Evaluate the total velocity distribution.

The merger tree provides more realistic values of the mass and of the infall time of each subhalo of the tree.

The potential assumed to describe the system in which the progenitors are falling is still the isochrone one, and it does not evolve in time. A crucial point of the model is the fact that the potential would change in time. This can be due either to the presence of recent major mergers or to the fact that the potential changes strongly as soon as the halo becomes more massive. The presence of major merger is excluded because the absence of these phenomena is one of the selection criteria for the choice of the merger tree. Because of the absence of major mergers, the potential evolves slowly in time. As a consequence, the increase of the number of substructures due to the change of the potential would be marginal. Concerning the change of the potential, it would be a relevant problem in the outer part of the Milky Way, while the Solar System is located in the central region of the Galaxy. The initial conditions adopted for each merger are discussed in more detail in Section 4.3. Halos do not have a sharp edges, so it is convention to use the virial radius to define their size. Using Equations (2.49) and (2.50) it is easy to make a direct estimate of the dependence of the virial radius of halo on its virial overdensity and on its mass, which are two of the quantities provided by the merger tree:

$$r_{vir} = \left(\frac{2GM}{\Delta_{vir} H^2(z)} \right)^{1/3} . \tag{4.2}$$

The Hubble parameter is redshift-dependent

$$H^2(z) = H_0^2 [\Omega_m (1+z)^3 + \Omega_\Lambda] \, , \tag{4.3}$$

so Equation (4.2) becomes

$$r_{vir} = \left(\frac{2GM}{\Delta_{vir} H_0^2 [\Omega_m (1+z)^3 + \Omega_\Lambda]} \right)^{1/3} . \tag{4.4}$$

Using Equation (4.1) we can determine the redshift and, as a consequence, r_{vir}. At each timestep the virial radius of the main halo is assumed to be the distance from which the subhalos fall into the Galaxy. This assumption is analysed in more detail in Section 4.3.1. Knowing z, it is straightforward to obtain the corresponding time in years: this quantity has been calculated using a cosmology calculator, developed by Wright (2006). The calculator allows one to input the values of H_0, Ω_m, Ω_Λ and z, and returns the years corresponding to that particular redshift. The cosmological

parameters used to determine t are the same used by Benson to generate the merger trees that we are using in the model.

The evolution of a halo presented in a merger tree can be read either from the redshift corresponding to the beginning of the simulation (in our case $z = 19$) to $z_0 = 0$, or in the opposite "direction", following a "bottom-up" approach (from $z_0 = 0$ to $z = 19$). We decided to use the "bottom-up" approach because it allows us to easily trace backward in time the formation history of the parent halo and because it also allows us to distinguish the contribution of the direct progenitors from the ones of all the other secondary progenitors. Being interested in the formation of a Milky Way-like system, we select a merger tree with no recent major merger events. This assumption is coherent with the idea that the Milky Way has not suffered any major merger in its recent past. Moreover, there is no need of recent major mergers to form a disk system (Binney & Tremaine 2008)

We define a merger as "major" when the two systems have comparable mass (within 50%). To simplify the calculation only the subhalos which are merging directly into the main progenitor of the Galactic halo are considered. A test has been performed to verify that with this assumption we did not ignore an important part of the total mass of the final halo: simulations taking into account both the first and the second order of progenitors of the final halo and its complete merger history have been run, and we have found that the final result of these simulations is not influenced by the fall of the second (or lower) order of satellites into the Galactic halo. We have also checked that the masses of the direct progenitors are already taking into account those of the indirect mergers.

One of the refinements introduced in the model involves in the technique we use to obtain the final (at redshift z_0) ultra-fine velocity distribution. In Chapter 3, we determined $f(\mathbf{v})$ of a system with a multiple merger history simulating this quantity for every component. After this step, a crude approximation of the final velocity distribution was calculated as the superimposition of the individual ones. To obtain a more accurate estimate of the final velocity distribution of the Galactic halo we now organise the values of $f(\mathbf{v})$ of each particle composing each direct progenitor of the main halo in a three-dimensional array. To explain the approach that we adopt, it is useful

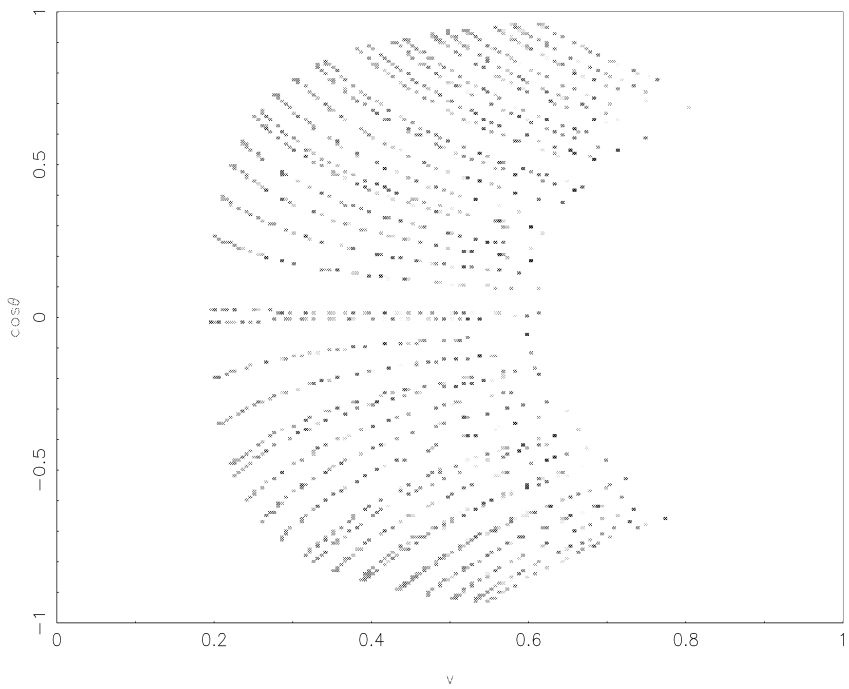

Figure 4.2: Speed and angle distribution (with respect to the direction of the Solar motion) for a subhalo of $10^9\,M_\odot$, which falls into the Milky Way with zero initial velocity from a distance of $\mathbf{r}_{sat} = (-80,\, 0,\, 0)$ kpc. The size of the subhalo is $\simeq 2$ kpc and the velocity dispersion $\simeq 60$ km s^{-1}. The features present in the figure are artifacts.

to consider the plot $(\cos\theta, v)$. To obtain the three-dimensional representation of $f(\mathbf{v})$ we firstly divide the two quantities into n_θ and n_v cells, creating a $n_v \times n_\theta$ grid. Secondly, the contributions of the particles which occupy the same "pixels" are added up and the logarithm of the velocity distribution, $\log f(v)$, is calculated. To represent this velocity distribution we draw a grey-scale of the array, with the shade of each pixel determined by the corresponding array value. This method has the substantial advantage of producing a more realistic estimate of the final velocity distribution of the Galactic halo than the one calculated in Chapter 3, and also of providing a three-dimensional representation of the angle distribution. Moreover, a change in the number of cells of the grid produces an increase (or a decrease) in the resolution of the quantities we are interested in: v and $\cos\theta$. Particular attention has to be paid when fixing this number: if it is of the same order of magnitude as the number of particles composing the system, the array will not be populated enough and artifacts will appear. Figure 4.2 gives an example of these artifacts. We simulate the merger of a subhalo of mass M $= 10^9\,M_\odot$, $\sigma_s \simeq 2$ kpc and $\sigma_v \simeq 60$ km s^{-1}. The evolution time of the system is $t \simeq 13.6\,$Gyr and the falling distance $\mathbf{r}_{sat} = (-80,\, 0,\, 0)$ kpc, with zero initial velocity. The curves

that populate the plot are not real structures but only artifacts. Their origin is caused by the fact that the number of particles composing the falling subhalos is similar to the number of pixels composing the grid. The result is that only some areas are populated, producing a value of $f(v)$ large enough to be visible. There are two possible solutions for this problem: to increase the number of particles composing the satellite or to reduce the number of cells of the array. The second solution has as an impact on the resolution of v and $\cos\theta$, which can be drastically reduced.

Some tests have been performed to verify the correctness of the method we have developed. To verify the absence of other artifacts we firstly merged a system assuming the contribution of each particle to the final velocity distribution as a constant. This allowed us to verify the absence of empty areas, which could be caused by an incorrect division of the array. In a second test two merger trees have been considered: the first one was describing a system without any major merger activity, the second one with the presence of two major mergers. The test consisted in adding the major mergers present in the second tree to the first one and in verifying the similarity of the distribution function of these two systems.

Until now, we have not yet discussed the dimension of the cells composing the array. To calculate the resolution of each cell we need to know the limits of the two quantities that we are considering. Assuming $v_{esc} = 544$ km s^{-1} as the value of the escape speed from the Milky Way (Smith et al. 2007), we assume as highest limit for the speed a value slightly larger: $v_{max} = 570$ km s^{-1}. The lowest limit is $v_{min} = 0$ km s^{-1}. It is straightforward to obtain the dimension of a velocity cell in km s^{-1}:

$$v_{cell} = \frac{v_{max} - v_{min}}{n_v} = \frac{570}{n_v}\,\mathrm{km\,s^{-1}}\ . \tag{4.5}$$

If we fix $n_v = 100$, each cell will contain particles with a velocity within a range of $\simeq 5.7$ km s^{-1}, while a v-cell width of $\simeq 3.8$ km s^{-1} is obtained if $n_v = 150$. Finally, if we divide the range of speed in 200 pixels, the dimension of each division increases to $\simeq 2.9$ km s^{-1}. Concerning the angle resolution, the limits of the cosine of the angle are by definition: $\cos\theta = \pm 1$. Moreover, the relation between $\cos\theta$ and θ is not linear. This implies that the cells do not represent the same angle resolution. For a cell corresponding to values of $\cos\theta \simeq \pm 1$ (angles close to 0° and 180°), the resolution is almost ten times larger compared to that obtained when $\cos\theta \simeq 0$. If we set $n_\theta = 100$,

the resolution of a cell for small (and large) angles is $\simeq 11^\circ\,30'$, while for angles of about $\simeq 90^\circ$ the resolution increases to $\simeq 45'$. Increasing the number of divisions ($n_\theta = 120$), the dimension of a cell for large angles decreases to $\simeq 10^\circ\,30'$, while a resolution of 1° is reached for small values of $\cos\theta$. The possibility of changing the number of divisions, both in the angle and in speed, gives flexibility to mimic a wide range of resolutions. For example we compare an angle $\sim 10^\circ$, that represents a good approximation of the resolution of current directional detectors (Dujmic et al. 2008 and Ahlen et al. 2010 for a complete review) to the resolution necessary to resolve the signatures possibly produced by mergers. Different choices for the values of n_v and n_θ have been tested. A good compromise that we adopt for most of our analysis is to set $n_v = 150$ and $n_\theta = 120$.

4.3 Satellite's initial conditions

4.3.1 Initial position in the phase space

A rough estimate of the satellite's initial position, r_{sat}, is given by considering a value between the virial radius of the Galactic halo and the free-fall distance. The free-fall distance is the distance from which a body, subject only to the gravitational force of the Galactic halo, would fall to the centre of the system in a time t_{ff}, once it is released from rest. If we consider a body which falls radially into the gravitational well of a point source mass M in a time t_{ff}, the free-fall distance can be derived from Kepler's third law:

$$r_{ff} \propto \left(\frac{2\sqrt{2GM}t_{ff}}{\pi} \right)^{\frac{2}{3}} . \tag{4.6}$$

Once we pick a value for t_{ff}, the free-fall distance sets a upper limit on r_{sat}. Figures 4.3 - 4.4 show the values of the virial radius (black) and of the free-fall distance (red) for subhalos of different masses (from $10^6\,M_\odot$ to $10^{11}\,M_\odot$) at different redshifts ($z = 0.1,\,5$). For the calculation of r_{ff} the two redshifts are assumed as values for the free-fall time.

At high z the virial overdensity, defined relative to the mean density of the Universe at that redshift, is almost constant, while at lower z it starts to increase rapidly because

the density parameter Ω_m decreases with time. This change induces a decrease in the virial radius. The free-fall distance has a similar behaviour: considering a subhalo of a certain mass, at high redshift r_{ff} is larger than for a system at low redshift. At a fixed time, a more massive halo falls into the potential well from a larger distance, compared to a less massive halo. This leads us to set the falling distance equal to the virial radius of the main halo at the previous timestep.

Moreover, each subhalo falls into the parent galaxy from a random position on a sphere of radius $r_{sat} = r_{vir}$, following a radial orbit. The assumption of subhalos falling on radial orbits from random angles is a realistic representation of the hierarchical formation of a halo. This has been also confirmed by various simulations (Read et al. 2006, Diemand et al. 2007).

We also need a value for the second phase space coordinate, the initial velocity v_{sat}. A good approximation is to assume the velocity that a body, which started to fall into the host system from an infinite distance, has at the virial radius. This assumption is also physically motivated because most of the velocity will be due to the infall of the satellite into the potential well of the Milky Way. Applying conservation of energy to the system we obtain

$$v_{sat} = \sqrt{\frac{2GM}{r_{vir}}} \, . \tag{4.7}$$

4.3.2 Internal structure

The initial dark matter phase space distribution of each halo is assumed to be the bivariate Gaussian discussed in Section 2.5.1. Good approximation for the initial velocity dispersion and the spatial extent of the satellites are provided by the definitions of virial mass and the virial theorem. These two initial conditions have already been fully discussed in Section 2.5.3. Assuming $c = 10$ (Bullock et al. 2001), $\rho_c = 1.9 \times 10^{-26} h^2$ kg m^{-3} and using for the mass M_{vir} and the virial overdensity Δ_{vir} the values provided by the merger tree, it is possible to obtain an estimate of these two quantities from Equations (2.48) and (2.48).

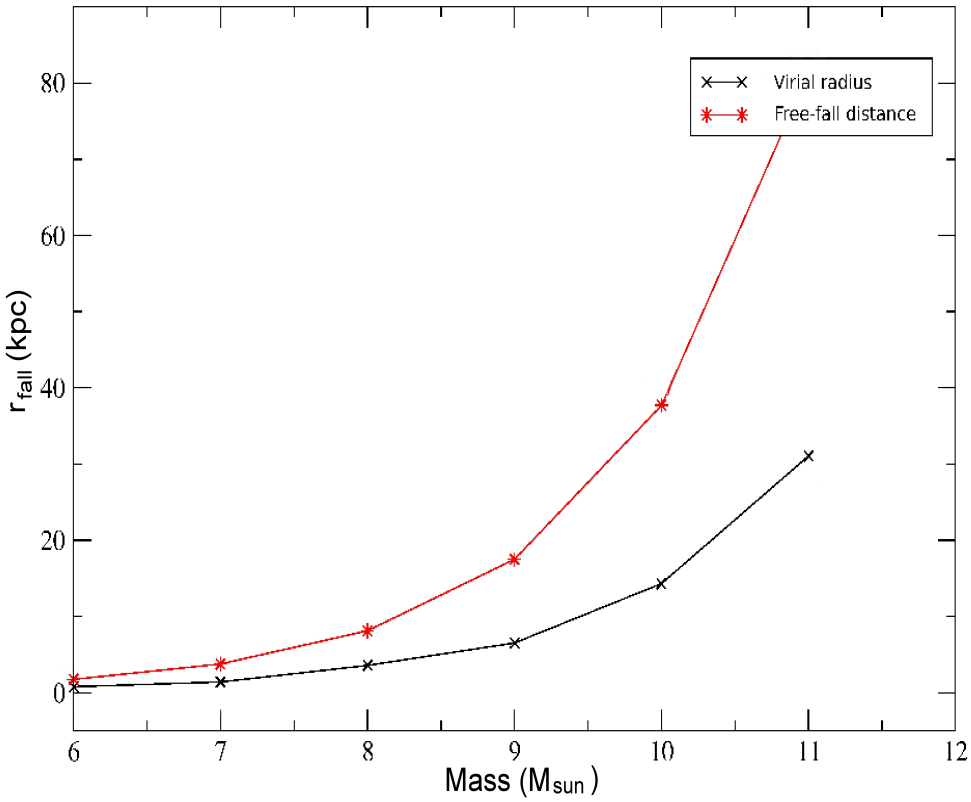

Figure 4.3: Free fall (red line) and virial radius (black line) for halos of masses in the range $10^6 - 10^{11} M_\odot$ that start to merge at $z = 0.1$.

4.3.3 Falling time

The time when the satellite starts to fall into the potential well of the halo is given by the scale factor. As already explained in Section 4.1, in a merger tree the infall time is defined as the moment at which the centre of the subhalo crosses the virial radius of the main halo. One further subtlety in the choice of the initial condition can be brought considering that observationally it is more interesting to look at the time at which the merging halos arrive at the detector's position. This time can be reasonably approximated by the moment in which the merging subhalo first reaches the centre of the host system. For this reason, for the last set of simulations (Section 5.3) we assume that at the time given by the merger tree the subhalos are already at the centre of the Galaxy. To take into account this temporal offset we anticipate the infall time of the subhalos. The distance from which the subhalos start to fall does not change (it is still the virial radius), but their evolution starts at time t'

$$t' = t + t_{\rm inf} \ , \tag{4.8}$$

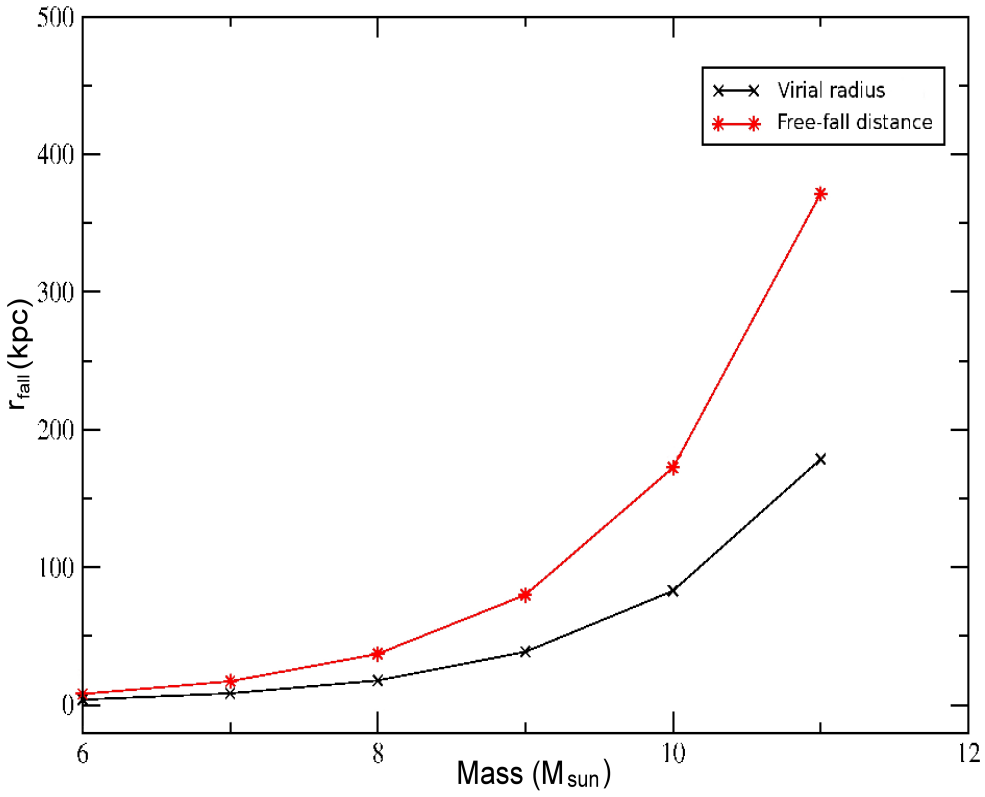

Figure 4.4: Free fall (red line) and virial radius (black line) for halos of masses in the range $10^6 - 10^{11} M_\odot$ that start to merge at $z = 5$.

where $t_{\rm inf}$ is the offset in time. In other words, it is the time necessary to cover the distance between the sphere of radius r_{sat} from which the satellites start to fall and the centre of the Galaxy. This change allows them to be in the centre of the dark halo at the time provided by the merger tree.

Chapter 5

Results for the formation of a Milky Way-like dark matter halo

In Chapter 4 we explained the procedure of combining the model developed in Chapter 2 with the merger tree of a Milky Way-like dark matter halo. The information provided by a merger tree (mass of the progenitors of the parent halo, redshift at which they fall into the host galaxy and virial overdensity) allows us to completely reconstruct the history of the halo. This refinement enables us to describe realistically the formation history of a Milky Way-like system. After assigning the initial conditions, the model calculates the velocity distribution from each branch of the tree, adds up all the contributions and finds the final phase-space distribution in the Solar neighbourhood, focusing in particular on the velocity distribution. The new version of the method can be applied to any merger tree, and not only to a system with a history resembling that of our galaxy. This in principle enables us to analyse the phase-space distribution of a wide range of systems.

This Chapter, which presents the final results of this project, is structured as follows: in Section 5.1 we briefly describe the velocity distribution and the fractional departure of the velocity-squared of a single subhalo from a smooth distribution. Section 5.2 contains the analysis of the results obtained simulating a Milky Way-like halo. Finally, Section 5.3 presents the contribution produced by the addition of a new progenitor to the Milky Way-like halo simulated in Section 5.2, in order to determine if late-arriving merging subhalos might be detectable.

5.1 Results for a single merger interaction

5.1.1 Diagnostic for directional detection

One of the goals of this project is to provide a prediction for the signal expected by directional detectors. Eq. (3.2) introduces a useful diagnostic for directional detection experiments: the angle at which the particles enter in the detector, measured relatively to the direction of the Solar motion in the Milky Way. To test the refined version of the model presented in Chapter 4, we simulate the velocity distribution for a series of single mergers. Figure 5.1 shows $\cos\theta$ as a function of the speed of the particles. Every cell on the x-axis corresponds to $\simeq 3.8$ km s^{-1}, while the angular resolution on the y-axis varies between $10^\circ\,30'$ (for small angles) and $\simeq 1^\circ$ (for large angles). The grey-scale of the plot, with the shade of each pixel determined by the corresponding array of the distribution function $f(\mathbf{r}, \mathbf{v})$, covers six orders of magnitude. Black corresponds to the upper limit and light grey to the lower one.

Compared to the simulations that have already been performed in Section 3.3.4, here we assume more realistic initial conditions for the initial position of the subhalo in the phase-space, its size and its velocity dispersion. In these simulations we assume cold and concentrated satellites (as expected in reality), merging into the parent galaxy on radial orbit from a position of $r_{\rm sat} = (-60,\, 0,\, 0)$ kpc. Their initial velocity is given by Equation (4.7) and their initial phase-space distribution function is given by Equation (2.46). The mass of the objects increases moving from the first row ($M = 10^8\, M_\odot$) to the second one ($M = 10^{10}\, M_\odot$). The $10^8 M_\odot$ satellite has initial spatial dispersion $\sigma_s \simeq 800$ pc and velocity dispersion $\sigma_v \simeq 25$ km s^{-1}, while for the more massive one $\sigma_s \simeq 4$ kpc and $\sigma_v \simeq 120$ km s^{-1}. Two evolution stages have been considered: an early one ($t \simeq 1.4$ Gyr, left column), which corresponds to few orbits of the subhalo around the Galactic centre, and a later one ($t \simeq 13.6$ Gyr, right column), describing a system with the same age as the Universe, which has travelled $\simeq 10$ orbits.

In comparing Figure 5.1a,b to Figure 3.11, it is important to note that the mass of the two subhalos that have been considered differs of one order of magnitude: $10^8\, M_\odot$ in the first case, $10^9\, M_\odot$ in the second. The plots are completely different. They demonstrate that the assumption of physically motivated initial conditions for

Fig. 5.1a: M $= 10^8\, M_\odot$, $t \simeq 1.4$ Gyr

Fig. 5.1b: M $= 10^8\, M_\odot$, $t \simeq 13.6$ Gyr

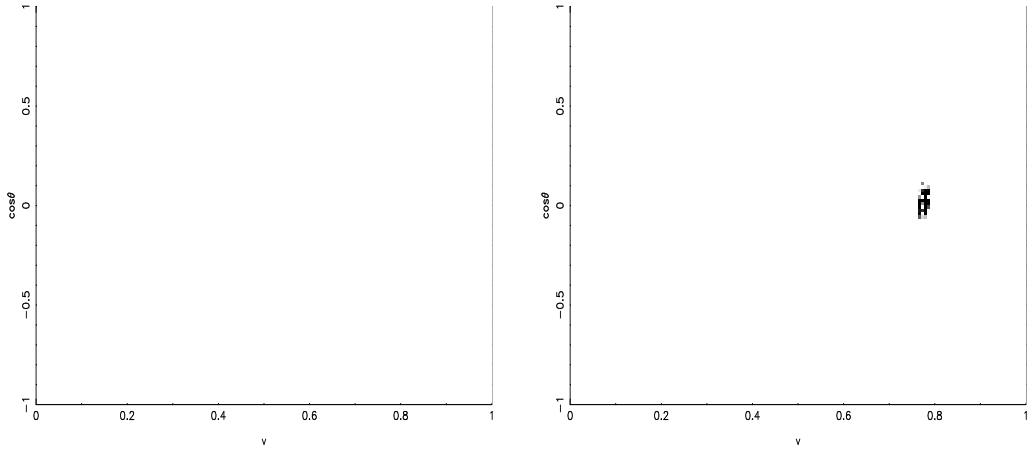

Fig. 5.1c: M $= 10^{10}\, M_\odot$, $t \simeq 1.4$ Gyr

Fig. 5.1d: M $= 10^{10}\, M_\odot$, $t \simeq 13.6$ Gyr

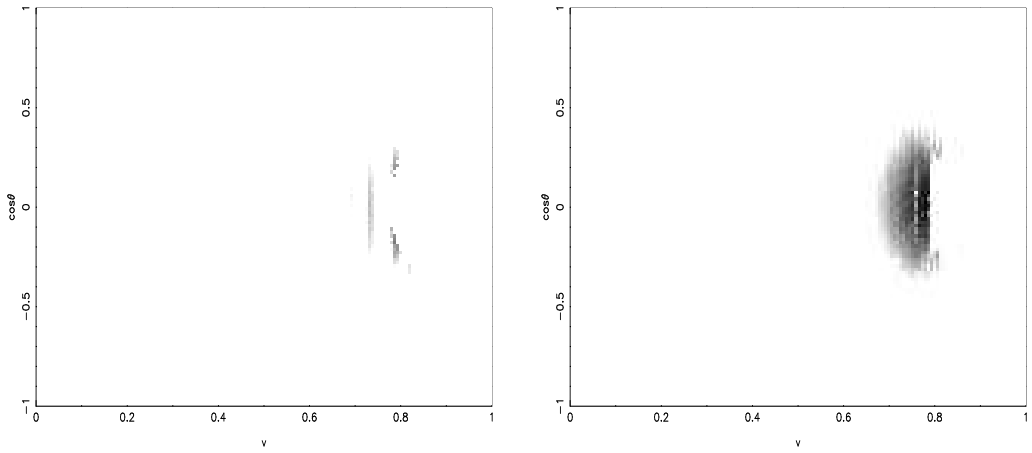

Figure 5.1: Four snapshots of the velocity distribution of subhalos of mass $10^8 M_\odot$ (top row) and $10^{10} M_\odot$ (bottom one) as a function of the speed and $\cos\theta$. Two evolution times are considered: $t \simeq 1.4$ Gyr (first column) and $t \simeq 13.6$ Gyr (second column). Both satellites are initially located at $r_{\rm sat} = (-60,\, 0,\, 0)$ kpc, with velocity $v_{\rm sat}$ given by Equation (4.7) and initial phase-space distribution function is given by Equation (2.46). They merge into the host halo on radial orbits. The $10^8 M_\odot$ satellite has size $\sigma_s \simeq 800$ pc and velocity dispersion $\sigma_v \simeq 25$ km s^{-1}, the $10^{10} M_\odot$ one $\sigma_s \simeq 4$ kpc and velocity dispersion $\sigma_v \simeq 120$ km s^{-1}. The spatial and velocity dispersion for both systems are given in Table 3.2. The plots have dimensions $n_v, n_\theta = (150 \times 120)$: every cell on the x-axis corresponds to $\simeq 3.8$ km s^{-1}, while the angular resolution on the y-axis varies between $10^\circ\, 30'$ (for small angles) and $\simeq 1^\circ$ (for large angles). One velocity-unit corresponds to 570 km s^{-1}.

Moreover, the grid of velocities at the Solar neighbourhood, useful to map out the full velocity distribution observable within the detector, was set only along the x-axis, while now it is three-dimensional.

The figures confirm that the mass of the satellite plays an important role in the dynamics of the system. From Figures 5.1a and 5.1b we can deduce that the merger of the smallest satellite ($10^8\ M_\odot$) into the host system does not generate visible features in the early stage of the evolution. The reason is that the satellite is still relatively intact and nether it nor the streams it is composed by are passing through the detector at this time. Once the system evolves, reaching an age of $\simeq 13.6$ Gyr, small features start to appear. In Figures 5.1c and 5.1d a more massive system ($10^{10}\ M_\odot$) is considered. From Figure 5.1c we deduce that the signature produced by streams of particles passing through the detector are clearly visible, even if the satellite has completed only few orbits. In fact, after an evolution time of $\simeq 1.4$ Gyr two vertical stripes, characterised by narrow ranges of velocities, populate the angle distribution. At each passage the satellite gets stripped, new streams form, starting to produce a more homogeneous configuration. At the late stage (Figure 5.1d) the angle distribution becomes more complex and the signature produced at each passage overlaps, resulting in the creation of a continuous arc feature.

For reasons of completeness we also investigated the velocity distribution of less massive objects, but neither 10^6 nor $10^7\ M_\odot$ subhalos show any visible fine-grain feature. We can thus conclude that the contribution of a single satellite with mass smaller than $10^8\ M_\odot$ is negligible when compared with that of a more massive system. This result is not surprising because we are considering very dense, compact objects (the velocity dispersion decreases once the mass decreases, as shown in Equation [3.1]), with long disruption times.

5.1.2 The energy spectrum

To investigate the evolution history of a system we can analyse its energy spectrum. The interest in this quantity, that describes the energy distribution of the particles composing the system, is motivated by the fact that it is observable. Figure 5.2 shows the energy spectrum of a dark matter halo of $10^{10} M_\odot$ after an evolution time of $\simeq 1.4$ Gyr.

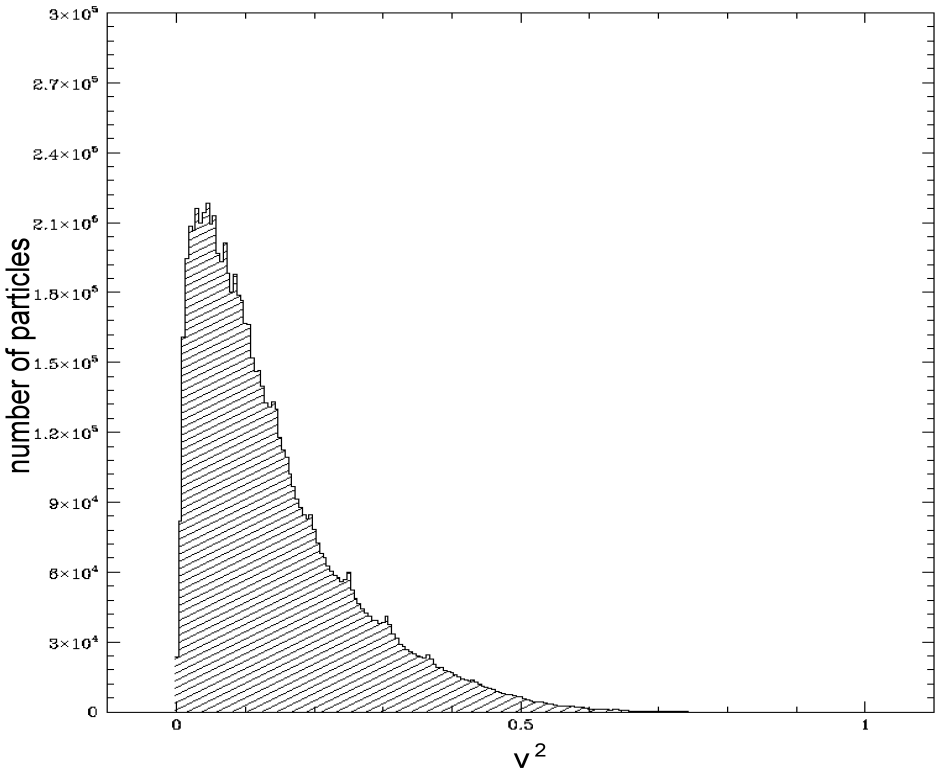

Figure 5.2: Energy spectrum of dark matter particles from a subhalo of mass $10^{10} M_{\odot}$ and evolution time of $\simeq 1.4$ Gyr, obtained using the forwards interaction technique. The satellite has size $\sigma_s \simeq 4$ kpc and velocity dispersion $\sigma_v \simeq 120$ km s^{-1}. It falls from a distance $r_{\rm sat} = (-60,\, 0,\, 0)$ kpc, with initial velocity $v_{\rm sat}$ given by Equation (4.7). One velocity-unit corresponds to 570 km s^{-1}.

This simulation has been performed using the forward interaction technique. This halo starts to fall into the Galaxy from a position $r_{\rm sat} = (-60,\, 0,\, 0)$ kpc and with velocity $v_{\rm sat}$ given by Equation (4.7). The initial phase-space distribution function is given by Equation (2.46), while its initial spatial and velocity dispersion have already been defined in Section 5.1.1. In the figure it is possible to infer the presence of a number of peaks, which are caused by the passage through the detector's location of the main body of the satellite.

To highlight the bumps present in the energy spectrum it is more appropriate to consider the fractional departure of the square of the velocity of the system from a smooth distribution, η, rather than its energy spectrum. The fractional departure is defined as the estimate (as a fraction) of how much the square of the velocity of a system differs from the smooth distribution, obtained when the satellite is almost completely relaxed. This quantity is particularly appropriate to analyse the evolution of an object because it highlights the presence of local overdensities and allows us to estimate how signif-

Fig. 5.3a: M $= 10^{10}\,M_{\odot}$, $t \simeq 1.4$ Gyr Fig. 5.3b: M $= 10^{10}\,M_{\odot}$, $t \simeq 13.6$ Gyr

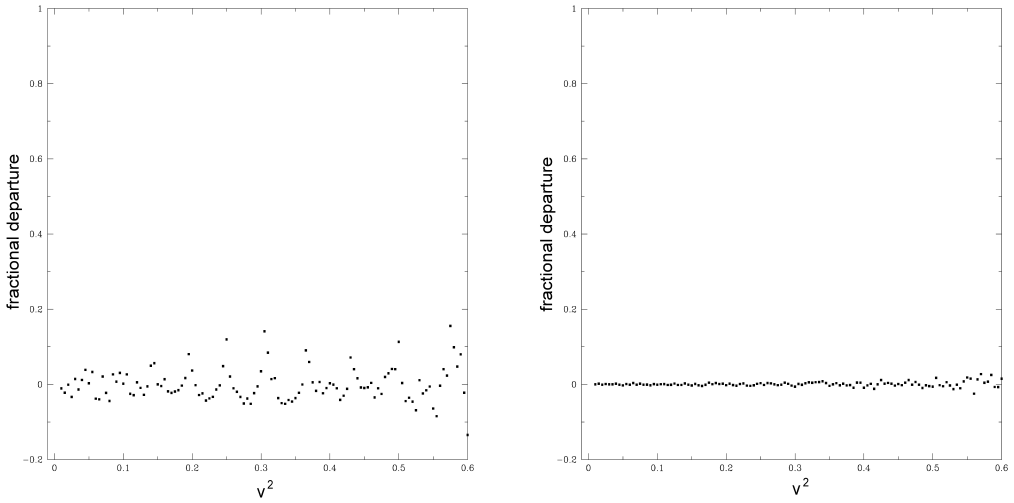

Figure 5.3: Fractional departure of v^2 from a smooth distribution for a subhalo of mass $10^{10} M_{\odot}$. Two stages of the evolution of the subhalo are presented: $t \simeq 1.4$ Gyr (Figure 5.3a) and $t \simeq 13.6$ Gyr (Figure 5.3b). The initial conditions are the same as assumed in Figure 5.1. We consider a time $t \sim 1400$ Gyr when the subhalo is expected to be relaxed and smooth. One velocity-unit corresponds to 570 km s^{-1}.

icant they are compared to the relaxed configuration of the system. It is calculated as the difference between the number of particles in a range of velocities at time t, N_e, and the number of objects in the same range once the system is relaxed, N_{rel}. This difference is then normalised by N_{rel}:

$$\eta = \frac{N_e - N_{rel}}{N_{rel}} \, . \tag{5.1}$$

We consider a system as being relaxed when η is equal to zero, which for a satellite of mass $10^{10} M_{\odot}$ happens when the evolution time t is much larger (~ 1400 Gyr) than the age of the Universe.

In the two snapshots of Figure 5.3 it is possible to notice that the features that were just visible in the energy spectrum are now evident. We consider only the subhalo of mass $10^{10} M_{\odot}$ because it is the only one which presents evident features in its velocity distribution. The plots of the fractional departure are obtained performing simulations with the same initial conditions as Figure 5.1. It is interesting to note that after an evolution time of $\simeq 1.4$ Gyr (Figure 5.3a) the fractional departure of the system presents clear peaks, that are 10% to 20% larger than the deviation produced by the system in its relaxed configuration. Each peak represents the passage of a stream of particles, and every stream is characterised by a specific value of v^2, and consequently of the energy, which identifies the orbit that the stream is following. This result is not sur-

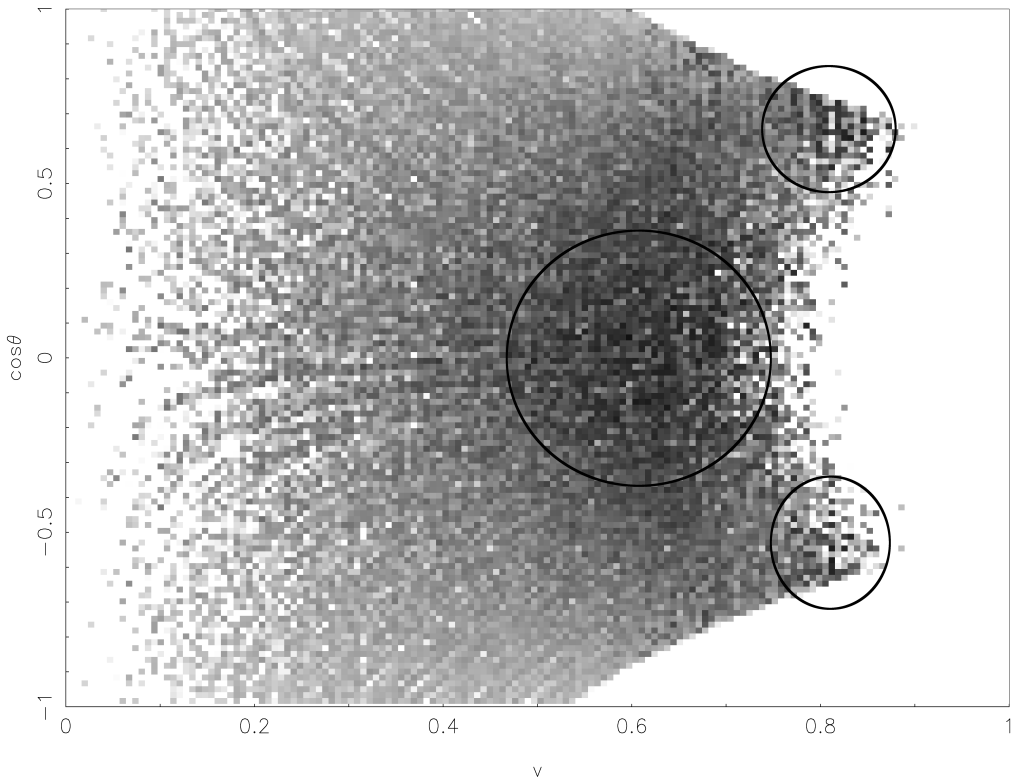

Figure 5.4: The velocity distribution of a Milky Way-like dark matter halo of mass $10^{12} M_{\odot}$ as a function of $\cos\theta$ and speed. The detector is located at a position $r_0 = (8.5,\, 0,\, 0)$ kpc. We use an array of dimensions $n_v, n_\theta = (150 \times 120)$. The dimension of a pixel on the x-axis is $\simeq 3.8$ km s^{-1}, while the angular resolution on the y-axis varies between $10^\circ\, 30'$ (for small angles) and $\simeq 1^\circ$ (for large angles). The three black circles pinpoints the regions where overdensities are present. One velocity-unit corresponds to 570 km s^{-1}.

prising: the satellite does not have sufficient time to get significantly disrupted by the potential of the host halo, due to the fact that it has completed only a few orbits around the Galactic centre. If we look at the same quantity after $\simeq 13.6$ Gyr (Figure 5.3b), we see that the fractional departure at this evolution time is not very different from the one of the system at its smooth configuration. This suggests that the mixing process is at an advanced stage. Moreover, the analysis of these peaks can help to shed light on the evolutionary history of the satellite.

5.2 Results for a Milky Way-like system

5.2.1 Diagnostic for directional detection

The Galactic halo is made up of multiple merger events and its velocity distribution is very complex. To represent this scenario in Figure 5.4 we present the angle distribution of a Milky Way-like halo of mass $10^{12}\,M_{\odot}$. The first point to note is that in the case of a complex system such as our galaxy no clear features are present. Nevertheless, the distribution is not completely homogeneous and the presence of darker areas demonstrates the existence of some overdensities. It is possible to identify three of them: the first overdensity is pinpointed by a large black circle, that identifies the particles with velocities in the range $285 < v < 400$ km s^{-1} and angles $65^{\circ} < \theta < 115^{\circ}$. This means that their direction is nearly perpendicular to the motion of the Sun in the Milky Way. The other two overdensities are less evident that the main one, and they appear at $\theta \simeq 55^{\circ}$ (top circle) and $\theta \simeq 125^{\circ}$ (bottom one) and they are composed by particles with very high velocity (~ 455 km s^{-1}), not far from the escape velocity of the system (~ 544 km s^{-1}). The possibility that these overdensities are artifacts cannot be ruled out, and it will be analysed in more detail in Section 5.2.2. To investigate the origin of these overdensities, we group together the contributions of progenitors with mass in the same order of magnitude and we study their contributions to the final velocity distribution. The merger tree we adopt for this simulation is composed of subhalos with masses in the range 10^{8} - $10^{12}\,M_{\odot}$, so the four groups are: $10^{8} - 10^{9}\,M_{\odot}$ (Figure 5.5a), $10^{9} - 10^{10}\,M_{\odot}$ (Figure 5.5b), $10^{10} - 10^{11}\,M_{\odot}$ (Figure 5.5c) and $10^{11} - 10^{12}\,M_{\odot}$ (Figure 5.5d). The four snapshots show that the contributions from these four groups of subhalos are very heterogeneous.

In Section 5.1.1 we concluded that the contribution of a single object of mass $10^{8}\,M_{\odot}$ was negligible, but when we add together the contributions of all the progenitors with mass of this order of magnitude (Figure 5.5a) we note that the situation is completely different. The number of direct progenitors in the range of mass $10^{8} - 10^{9}\,M_{\odot}$ is large and now their contribution to the final velocity-space distribution is not negligible anymore. The main contribution seems to come from particles which are moving mainly perpendicular to the plane of the Solar motion ($75^{\circ} < \theta < 105^{\circ}$), but there is no ev-

idence for a preferential range of velocity. This fact suggests that the particles which compose the satellites with mass of the order of $10^8\,M_\odot$ are not distributed homogeneously in the velocity space. This is probably due to the fact that they are compact: the timescale on which they get disrupted is longer than that of more massive systems and so even after an evolution time equal to the Milky Way's age they are not completely disrupted.

The contribution to the velocity distribution of the most massive subhalos, with mass in the range $10^{11-12}\,M_\odot$ (Figure 5.5d), is small if compared to the other three cases. This can be interpreted as a confirmation that the merger tree we have chosen to represent the Galactic halo has not suffered any major merger event in the recent past.

Finally, looking at the last two groups of progenitors (Figures 5.5b and 5.5c) we note that the contributions produced by subhalos of mass $10^{9-10}\,M_\odot$ and $10^{10-11}\,M_\odot$ are very similar. Nevertheless, an important difference can be highlighted: the contribution produced by $10^9\,M_\odot$ subhalos is almost smooth, while in the velocity distribution of $10^{10}\,M_\odot$ satellites there is a large and overdensity, which peaks in the centre of the plot and does not present any visible substructure. This overdensity covers every other small difference in the velocity distribution that may exists, but it suggests that the most pronounced overdensity of Figure 5.4 is mostly produced by satellite with masses in the range $10^{10-11}\,M_\odot$.

Figure 5.4 also tells us that some areas of the parameter space are inaccessible. Two restrictions are responsible for the creation of this inaccessible area. The first one is the presence of an escape speed, v_{esc}, from the Milky Way: if a particle has speed larger than this, it will leave the system without contributing to the angle distribution. This generates the two peaks present at $\cos\theta \simeq \pm 0.6$. The second restriction is related to the definition of $\cos\theta$, given in Eq. (3.2), and to the fact that $\mid \cos\theta \mid \leq 1$. These two conditions imply limits for each of the three components of the velocity. The presence of these limits, together with the existence of an escape velocity, explains the presence of the irregular shape of the inaccessible area: the value of each of the three components can only vary in a range which is limited by the values of the other two and by the definition of $\cos\theta$.

As mentioned above, some overdensities are present in Figure 5.4. Nevertheless, we

Fig. 5.5a: $10^8\,M_\odot \leq M < 10^9\,M_\odot$

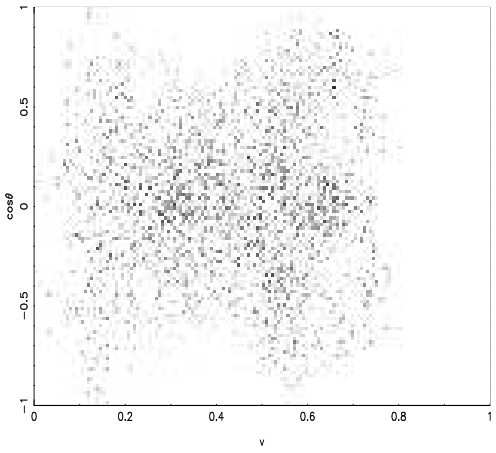

Fig. 5.5b: $10^9\,M_\odot \leq M < 10^{10}\,M_\odot$

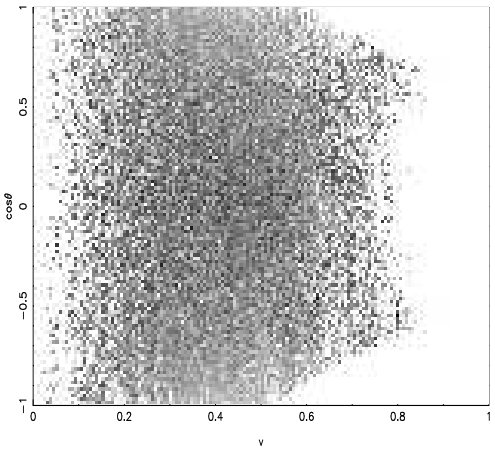

Fig. 5.5c: $10^{10}\,M_\odot \leq M < 10^{11}\,M_\odot$

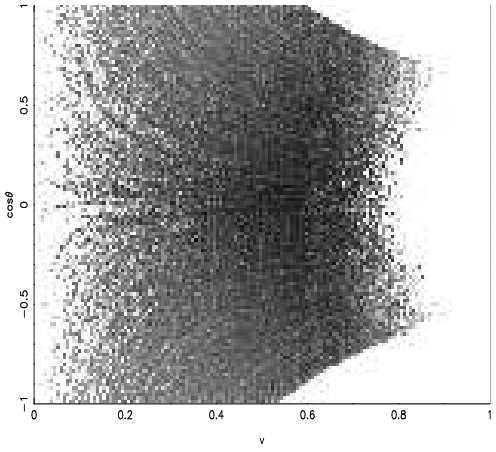

Fig. 5.5d: $10^{11}\,M_\odot \leq M < 10^{12}\,M_\odot$

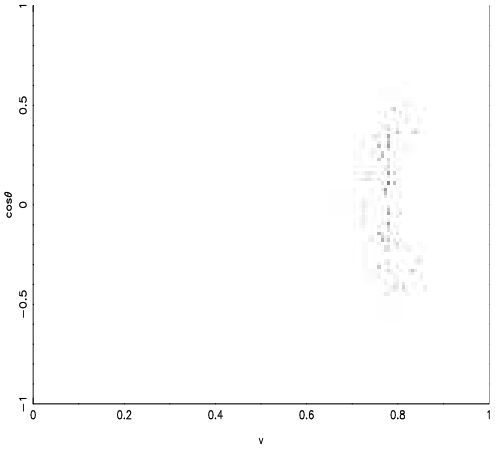

Figure 5.5: Series of snapshots showing the contributions to the Milky Way-like halo angle distribution, simulated in Figure 5.4, from four different groups of satellites. The satellites are divided depending on their mass: $10^8\,M_\odot \leq M < 10^9\,M_\odot$ (Figure 5.5a), $10^9\,M_\odot \leq M < 10^{10}\,M_\odot$ (Figure 5.5b), $10^{10}\,M_\odot \leq M < 10^{11}\,M_\odot$ (Figure 5.5c) and $10^{11}\,M_\odot \leq M < 10^{12}\,M_\odot$ (Figure 5.5d). The dimension of a pixel on the x-axis is $\simeq 3.8$ km s^{-1}, while the angular resolution on the y-axis varies between $10^\circ\,30'$ (for small angles) and $\simeq 1^\circ$ (for large angles). One velocity-unit corresponds to 570 km s^{-1}.

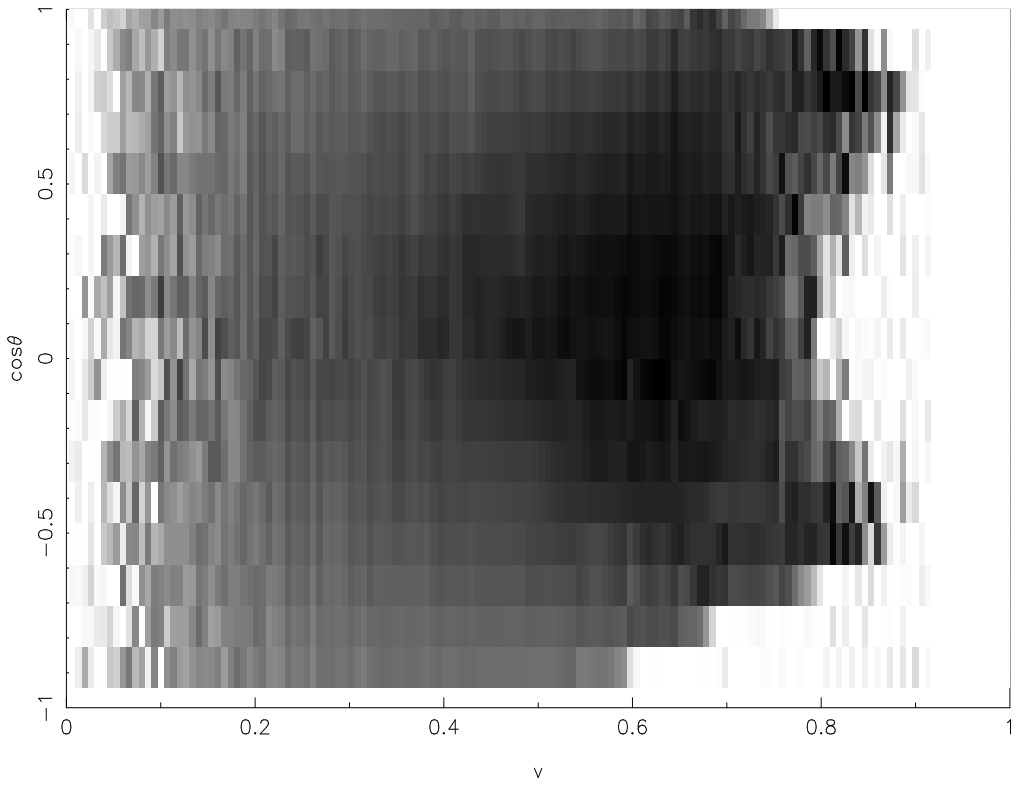

Figure 5.6: As Figure 5.4, but composed of a smaller number of cells: $n_v, n_\theta = (150 \times 18)$. The dimension of each cell along the y-axis is now $\simeq 10°$, resembling the resolution of current directional detectors. The velocity resolution remains constant at $\simeq 3.8$ km s^{-1}. One velocity-unit corresponds to 570 km s^{-1}.

should remember that in that plot the dimension of each pixel is $\simeq 1°$. These small angles are not accessible to ongoing experiments, that have angular resolution of $\simeq 10°$ (Dujmic et al. 2008, Ahlen et al. 2010 for a complete review). Figure 5.6 presents the velocity distribution for a resolution comparable to that of current directional detectors. The resolution is $\simeq 27°$ for the two cells for which $\cos\theta \simeq \pm 1$, but it increases to $\simeq 10°$ for $\cos\theta \simeq \pm 0$. Looking at the figure it is obvious that the features present in Figure 5.4 are indiscernible once we decrease the resolution of our "ideal" detector. The small, local overdensities are completely washed out, but the main one, which was centred in the range $65° < \theta < 115°$, is not. Nevertheless, we can conclude that the detectors currently available do not have the possibility to detect the features present in the velocity-space distribution of Figure 5.4 because the boundary between the overdensity and the smooth "background" distribution is not clear. The angular resolution required for their detection is at least $\simeq 1°$.

5.2.2 Smoothed angle distribution

To investigate the presence of overdensities in the angle distribution we apply a standard "boxcar" smoothing technique. The assumption of this technique is meant to both remove the possible presence of artifacts and to highlight the overdensities that might be present in the angle distribution. This procedure assumes as the value for each cell composing the array the average of the data points over a selected area. The area we assume is a square of sides n_v and n_θ. The smoothed distribution function of each cell, $f_{\rm cell}(v)$, is

$$f_{\rm cell}(v) = \frac{\sum_{i=1}^{n_v}\sum_{j=1}^{n_\theta} f_{i,j}(v)}{n_v n_\theta} \,, \tag{5.2}$$

where $f_{i,j}(v)$ is the value of the distribution function of each pixel belonging to the box. The advantage of using this technique is that the results become smoother as the size of the box increases, highlighting the presence of overdensities in the velocity distribution of the system. However, important details may be lost, in particular when the data points are averaged over large areas.

It is possible to use a more sophisticated version of the boxcar technique through a refinement in the calculation of $f_{\rm cell}(v)$. The idea is to weight the contribution of the pixels depending on their positions in the box. In the refined technique that we adopt here

$$f_{\rm cell}(v) = \frac{f_{\rm centre}(v)/2 + \sum_{i=1}^{n_v}\sum_{j=1}^{n_\theta}(f_{i,j}(v)/2)}{1+\frac{1}{2}(n_v n_\theta - 1)} \,. \tag{5.3}$$

Figure 5.7 presents four different smoothed versions of the velocity distribution already performed in Figure 5.4. In the first row we apply the technique defined in Eq. (5.2). The difference between the two plots is given by the size assumed for the box: (3×3) in the left corner, (5×5) in the right one. In the second row we considered the same configurations, but we apply the refined technique [Eq. (5.3)].

Looking at the four plots of Figure 5.7, the "original" versions of the boxcar smoothing technique (Figure 5.7a-b) and the "refined" one in a (3×3) box (Figure 5.7c) do not produce any notable improvement if compared to the original distribution (Figure 5.4). On the other hand, a significant improvement is evident when we analyse Figure 5.7d. This plot corresponds to the "refined" version of the smoothing technique over a (5×5) box. The application of this technique has the advantage of removing all the

Fig. 5.7a: "Original" boxcar technique, (3×3) box

Fig. 5.7b: "Original" boxcar technique, (5×5) box

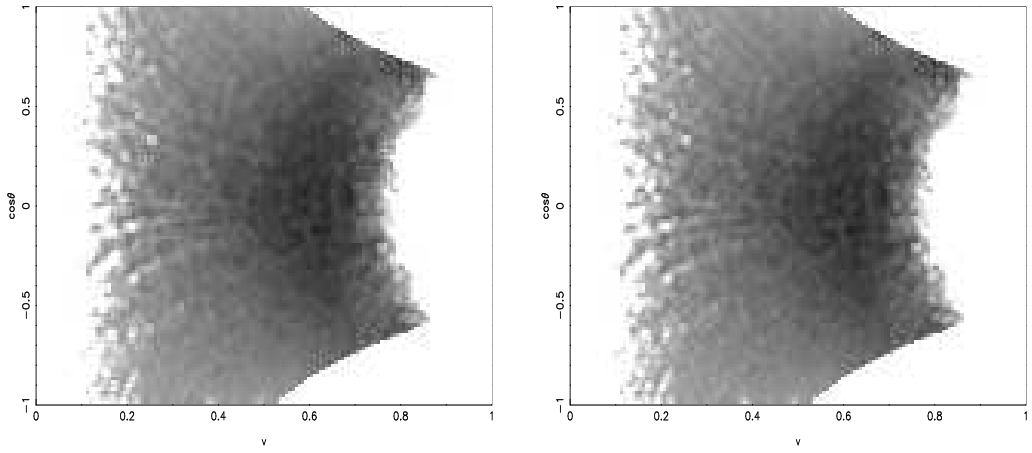

Fig. 5.7c: "Refined" boxcar technique, (3×3) box

Fig. 5.7d: "Refined" boxcar technique, (5×5) box

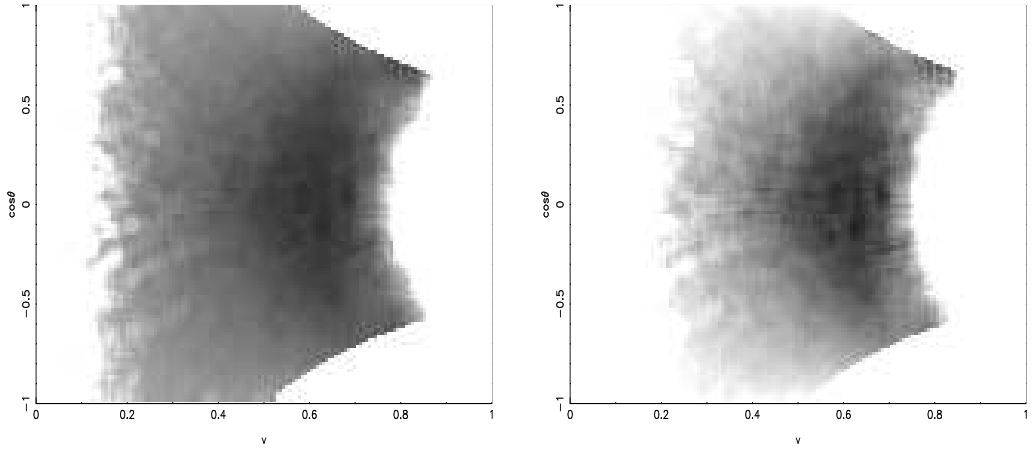

Figure 5.7: Smoothed velocity distribution of the Milky Way-like halo presented in Figure 5.4. The four plots are calculated using the boxcar technique described in Section 5.2.2. In the first row the velocity distribution is smoothed using the "basic" technique, that averages the data points over an area (3×3) (Figure 5.7a, left column) and (5×5) (Figure 5.7b, right column). In the second row we refine the smoothing technique. The contribution of every pixel is now weighted, depending on its position in the area that we consider: 100% for the central pixel, 50% for all the others constituting the selected area. In Figure 5.7c the angle distribution is smoothed over an area (3×3), while in Figure 5.7d we consider a (5×5) box. The four plots have constant cell-dimensions: $n_v = 150$, $n_\theta = 120$. One velocity-unit corresponds to 570 km s^{-1}.

small differences present in the velocity-space distribution, that are mainly due to the presence of pixelation artifacts. For this reason in the following sections we will use only the (5×5) "refined" version of the boxcar technique to investigate the presence of overdensities in the velocity distribution.

The application of a smoothing technique confirms the presence of an overdensity in the angle distribution of the Galactic halo. As mentioned above, the smoothing procedure has also the effect of spreading out the features present in the plot, in particular when a large area is considered. This effect explains why the central overdensity is now more clear, but it also covers a broader range of angles, extending from $\theta \simeq 60^\circ$ to $\theta \simeq 120^\circ$. A second level of overdensities seem to be present, though it is difficult to separate them from the main one. On the other hand, when we look for the two overdensities composed by particles with speed close to the escape limit, they have vanished completely, raising the hypothesis that they were artifacts. The presence of features which are highlighted also by the application of the smoothing technique, raises the possibility of disentangling at least the recent merger history of the halo. This could be achieved by directional detectors with angle and velocity resolution of $\simeq 1^\circ$ and $\simeq 3.8$ km s^{-1}. Unfortunately, as we have already mentioned, this required angular resolution is an order of magnitude better than that of current detectors (Dujmic et al. 2008, Ahlen et al. 2010).

In the simulations described to this point, each progenitor starts to fall into the Milky Way from a distance equal to the virial radius of the main progenitor at time t_i. Figure 5.8 presents the velocity-space distribution of the same Milky Way halo considered in Section 5.2.1, but assuming that at t_i the subhalos are already in the centre of the host halo. In other words, we anticipate the moment in which the subhalos start to fall into the potential well of the Galaxy. This change, discussed in Section 4.3.1, is introduced to analyse the effects produced by an increase of the evolution time of the Galaxy and also to assume a definition of a merger between two systems closer to the one relevant to observations. The velocity distribution still peaks in the speed range 285 km s$^{-1} \lesssim v \lesssim 400$ km s^{-1}, but the most interesting difference is that in Figure 5.8 this overdensity is not as evident as in Figure 5.4. This means that a small increase of the evolution time of the direct progenitors leads to a remarkable decrease in the

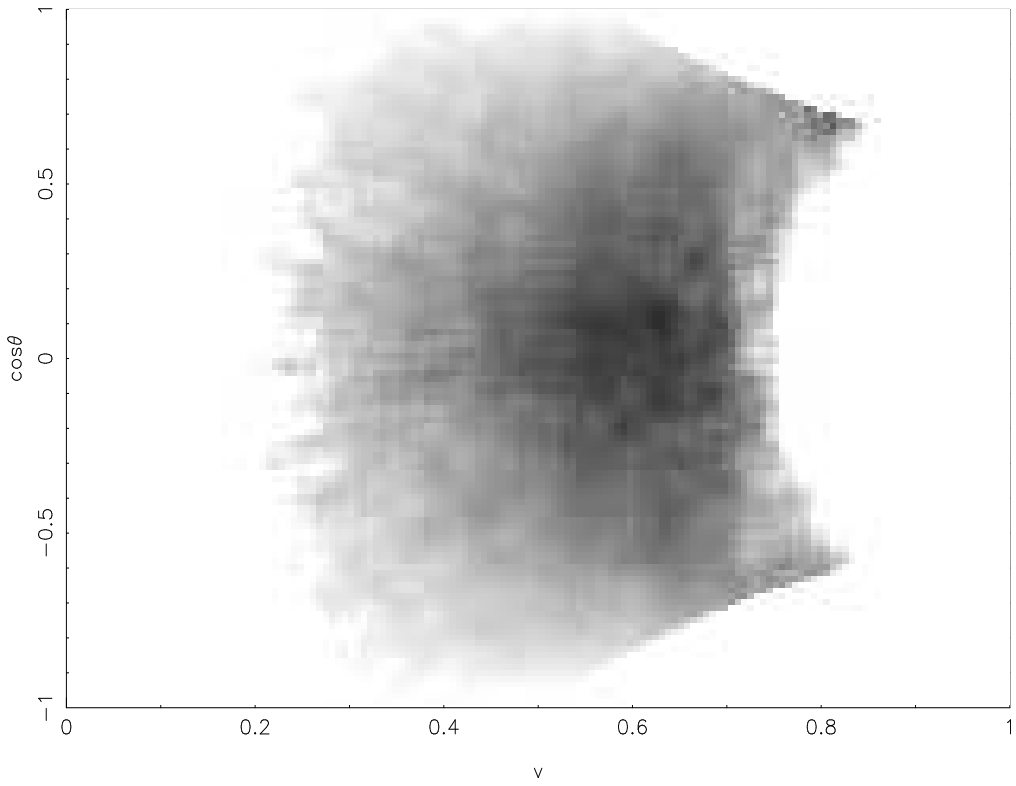

Figure 5.8: The same (v, $\cos\theta$) plot presented in Figure 5.4, but assuming that at the infall time provided by the merger tree the progenitors are already in the centre of the Galaxy. The image is smoothed using the (5×5) "refined" technique, to highlight the overdensities present in the velocity distribution of the system. One velocity-unit corresponds to 570 km s^{-1}.

granularity of the velocity-space distribution.

5.2.3 Fractional departure of the Galactic halo from a smooth distribution

In Section 5.1.2 we have defined the fractional departure of the velocity-squared of a halo from a smooth distribution, an alternative diagnostic to investigate the evolution history of a system and to highlight the traces left by the passage of streams of dark matter through an ideal detector. In that Section we also saw that the merger of a single subhalo can produce clear velocity peaks. Given those interesting results, in Figure 5.9 we present the same quantity, for the Galactic halo that we are currently analysing. The system we consider has a mass of $10^{12}\,M_{\odot}$ and an age of $\simeq 13.2$ Gyr.

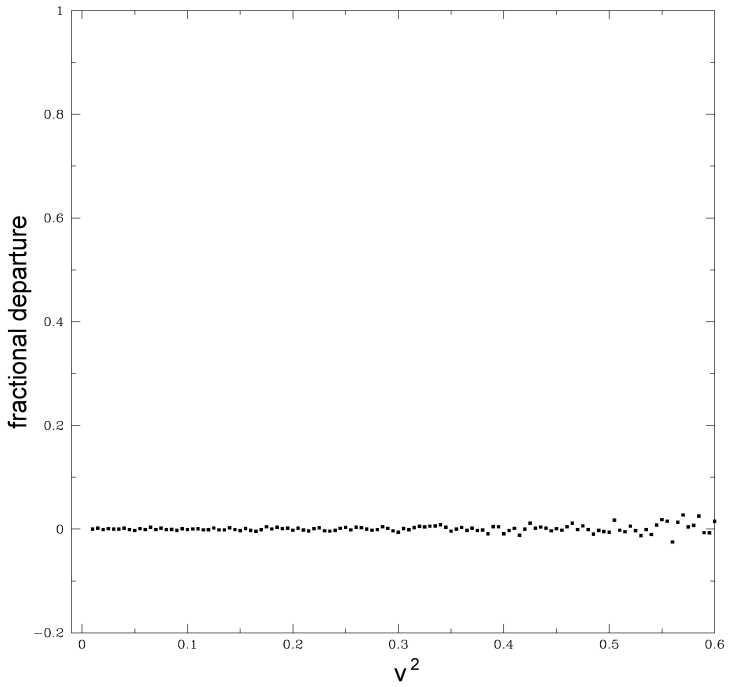

Figure 5.9: Fractional departure of the velocity-squared of the Galactic halo (simulated in Section 5.1.1 and presented in Figure 5.4) from a smooth distribution for an evolution time $t \simeq 13.2$ Gyr. The merger history of this halo does not include any major merger. We consider a time $t \simeq 1400$ Gyr when the system is expected to be relaxed and smooth. One velocity-unit corresponds to 570 km s^{-1}.

The fractional departure of this halo, which resembles that of the Milky Way in terms of age, mass and formation history, is indiscernible from the distribution that the halo assumes when completely relaxed. The absence of any feature leads to the conclusion that the ultra-fine dark matter distribution in the Solar neighbourhood of a halo evolved for 13.2 Gyr is composed of a huge amount of streams that produce an entirely featureless energy spectrum. The result is in agreement with the recent work by Vogelsberger & White (2010), in which they conclude that the velocity distribution in the Solar System should be very smooth.

5.3 Contribution of single merger events to the ultra-fine distribution of a Milky Way-like system

The fractional departure of the velocity-squared of the Milky Way-like system from a smooth distribution, simulated in Section 5.2.3, suggests that nowadays the dark matter

distribution in the Solar neighbourhood is overall almost smooth. However, Figure 5.4 suggests that the dark matter distribution may not be completely smooth, particularly if there has been a relatively recent merger. The idea behind the last part of the project is to combine the work developed in the previous Sections of this Chapter, analysing the contribution from single mergers. We are interested in answering the following questions: what is the contribution to the final velocity distribution of a single merger? Will it lead to a detectable signature in the global distribution?

The method we adopt consists of adding a dark matter satellite to the Galactic halo and of analysing its contribution to the final velocity-space distribution. This analysis is done for subhalos of different mass and for various evolution times. The evolution history of the host system is provided by the same merger tree that was used in Section 5.2, but in these simulations we assume that at the time provided by the merger tree the progenitors of the Galactic halo are already in the centre of the dark halo. We make the same assumption for the subhalos of different masses that we adopt as additional progenitors. Every extra progenitor fall into the parent galaxy from a random position on a sphere of radius $r_{\rm sat} = r_{\rm vir}$, following a radial orbit. Consequently, there is the possibility that these extra progenitors have already performed a passage in the Solar neighbourhood in the time necessary to reach the Galactic centre. The reasons for this modification of t_i have been already discussed in Section 4.3.1 and at the end of Section 5.2.2.

As mentioned above, the two properties of the additional progenitor that we vary are the mass and the time at which it falls into the Galaxy. Concerning the mass, we consider four different cases: $M_1 = 10^7\,M_\odot$, $M_2 = 10^8\,M_\odot$, $M_3 = 10^9\,M_\odot$ and $M_4 = 10^{10}\,M_\odot$. The absence of major mergers in the recent history of the Milky Way, together with the fact that massive systems can strongly perturb the potential of the Galactic halo, motivates the exclusion of subhalos more massive than M_4. To get a complete overview of the evolution of the mergers we select four times in the past at which the progenitor falls into the host halo:

- $t_1 \simeq 1.75\,$Gyr ago ($z = 0.14$): this time is chosen so that the subhalo is making its first passage through the detector today at redshift $z = 0$.
- $t_2 \simeq 2.0\,$Gyr ago ($z = 0.17$): early stage of the evolution, chosen so that the

Mass $M_\odot$ / Infall Time (Gyr ago)	1.75	2.0	7.5	13
10^7	$\times$	$\times$	$\times$	$\times$
10^8	$\times$	$\times$	$\times$	$\times$
10^9	✓	$\times$	✓	✓
10^{10}	✓	✓	✓	✓

Table 5.1: Table showing the presence (or absence) of differences between the velocity distribution of a system composed of the Milky Way-like halo plus the contribution of a single subhalo and the Milky Way-like halo only. Different masses are considered for the new progenitor, as well as different infall times. The symbol ✓is used when there is at least the value of one pixel that differs in the six orders of magnitude considered for the two velocity distributions (Galactic halo and Galactic halo plus progenitor). On the other hand, if the values of all the pixels composing of the two $f(\mathbf{r}, \mathbf{v})$ are identical in the six orders of magnitude defined above, the symbol $\times$ is used.

satellite is not passing through the detector today.

- $t_3 \simeq 7.5\,$Gyr ago ($z = 1.0$): this timestep is chosen so that the merger is at an intermediate stage of its evolution today.

- $t_4 \simeq 13\,$Gyr ago ($z = 8.5$): a satellite which merged at an early stage of the formation of the Milky Way.

These timesteps take into account the time necessary for the subhalo to reach the centre of the Galaxy. All the results we are going to present describe properties of a Milky Way-like halo at redshift $z_0 = 0$.

5.3.1 Diagnostic for directional detection

In Figures 5.10 - 5.13 we plot in the $(\cos\theta, v)$ space the velocity distribution of the systems composed by the Milky Way-like halo and the four different satellites that we have selected. Each Figure is composed of four plots that show the changes produced by the four infall times of the satellite. Each plot is smoothed using the "refined" boxcar technique over a (5×5) box. To optimise the analysis of the results we group them according to the mass of the subhalo: the angle distributions of M_1 at the four selected timesteps are grouped together in Figure 5.10, while Figure 5.11, 5.12 and 5.13 present the same quantity for the satellites M_2, M_3 and M_4 respectively.

It is interesting to compare the results presented in these figures to the velocity distribution of the "original" Milky Way halo (Figure 5.8). This comparison is presented in Table 5.1, which shows the presence (or the absence) of differences between the veloc-

ity distribution of a system composed of the Milky Way-like halo plus the contribution of one of the extra progenitors and the Milky Way-like halo only. The comparison is done by subtracting the value of the distribution function of the Milky Way halo in each cell of the grid from the corresponding value for the set-up in which the extra progenitor is added. The shade of each pixel of the plot is determined by the corresponding array value and it covers six orders of magnitude in the value of the velocity distribution $f(\mathbf{r}, \mathbf{v})$. The black colour corresponds to the upper limit and the light grey to the lower one. The symbol ✓is used when there is at least the value of one pixel that differs in the six orders of magnitude considered for the two velocity distributions (Galactic halo and Galactic halo plus progenitor). On the other hand, if the values of all the pixels composing of the two $f(\mathbf{r}, \mathbf{v})$ are identical in the six orders of magnitude defined above, the symbol $\times$ is used.

The table tells us that the addition of either M_1 or M_2 to the Galactic halo does not have any impact on the ultra-local velocity distribution at z_0. In other words, the effect of the addition of an extra progenitor of mass between $10^7\, M_\odot$ and $10^8\, M_\odot$ to the merger tree of the Galactic halo is negligible. This is valid for all the evolution times that we consider: t_1, t_2, t_3 and t_4. The contribution of a single progenitor starts to be relevant when the mass of the new merging subhalo is equal or larger than $10^9\, M_\odot$.

Some of the conclusions of Table 5.1 seem in conflict with the analysis of the results presented in Figures 5.10 - 5.13. In fact they reveal that the angle distribution of some of the new systems is almost identical. This is the case for the systems composed of the Milky Way-like halo plus the subhalo M_1 (Figure 5.10) , M_2 (Figure 5.11) and M_3 (Figure 5.12), and it is valid for all the timesteps: t_1, t_2, t_3 and t_4. For example, the table indicates the presence of differences between the velocity distribution of the system composed by the Milky Way plus M_3 and the one of the Milky Way halo-only at t_1, t_3 and t_4. On the other hand, a comparison between Figure 5.12 and Figure 5.8 does not show any clear sign left by the presence of an extra progenitor. Nevertheless, the information provided by Table 5.1 and by Figures 5.10 - 5.13 are complementary rather than contradictory. As already explained above, the table provides information on the contribution generated by the addition of a satellite to the velocity distribution of the Milky Way-like halo, but it does not provide any information about the strength

Fig. 5.10a: $t_1 \simeq 1.75$ Gyr

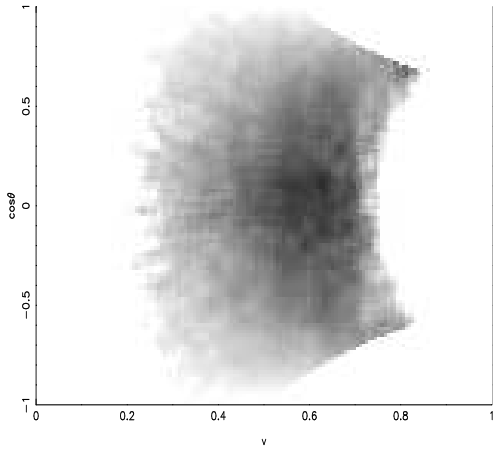

Fig. 5.10b: $t_2 \simeq 2.0$ Gyr

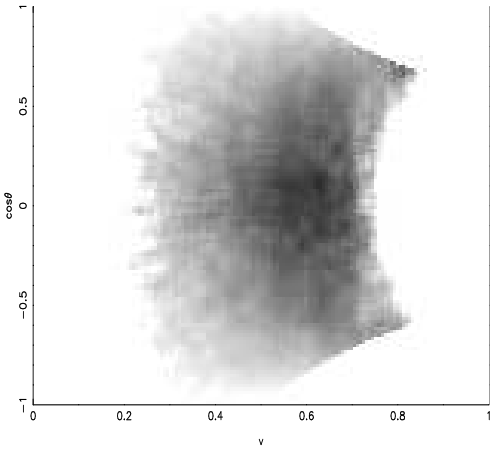

Fig. 5.10c: $t_3 \simeq 7.5$ Gyr

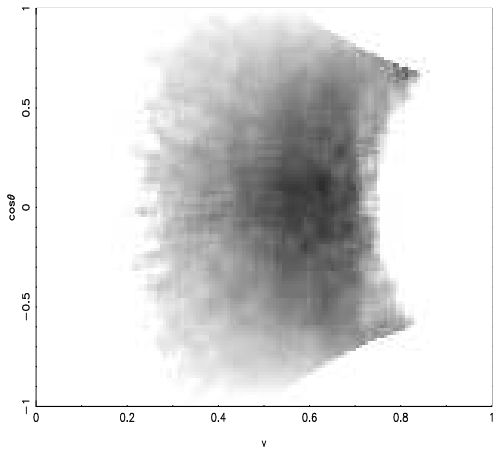

Fig. 5.10d: $t_4 \simeq 13$ Gyr

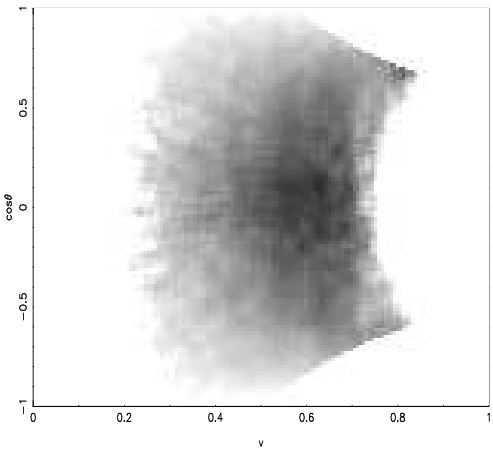

Figure 5.10: Series of snapshots presenting the angle-velocity plot at z_0 of a system composed by the Milky Way-like halo already simulated in Figure 5.8 and a subhalo of mass $10^7\, M_\odot$. The distribution is smoothed using the "refined" boxcar technique described in Section 5.2.2, selecting a (5×5)box. The four plots describe configurations in which the progenitor falls into the host halo at different times. In Figure 5.10a it fell $\simeq 1.75$ Gyr ago. This time is chosen so that the subhalo is making its first passage through the detector today at redshift $z = 0$. Figure 5.10b corresponds to a infall time of $\simeq 2.0$ Gyr ago, chosen so that the satellite is not passing through the detector today. Figure 5.10c ($\simeq 7.5$ Gyr ago) is chosen so that the merger is at an intermediate stage of its evolution today. Finally, in Figure 5.10d the satellite merged $\simeq 13$ Gyr ago, at an early stage of the formation of the Milky Way. The dimensions of each pixel of the four snapshots is the same as Figure 5.4. One velocity-unit corresponds to 570 km s^{-1}.

Fig. 5.11a: $t_1 \simeq 1.75$ Gyr

Fig. 5.11b: $t_2 \simeq 2.0$ Gyr

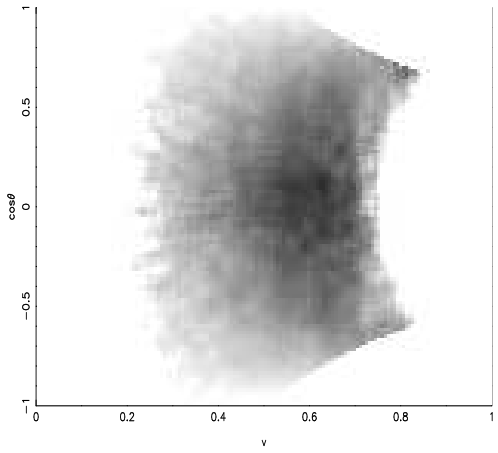

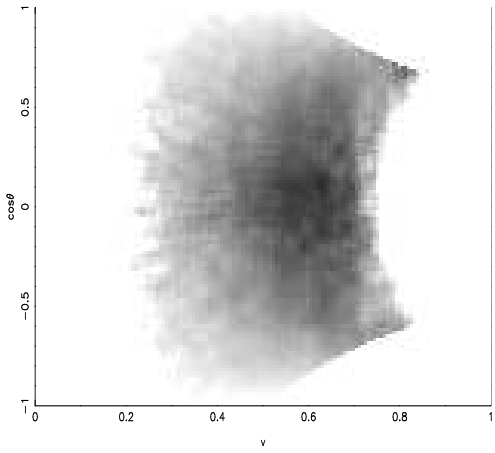

Fig. 5.11c: $t_3 \simeq 7.5$ Gyr

Fig. 5.11d: $t_4 \simeq 13$ Gyr

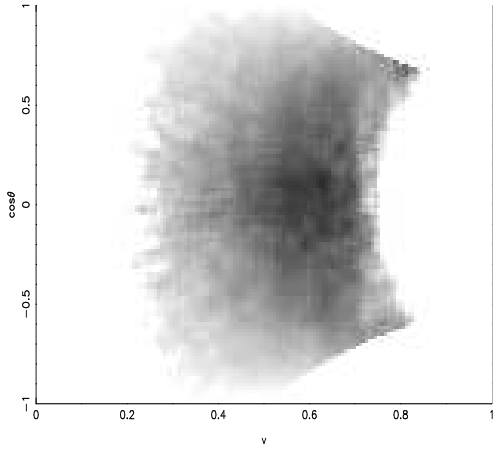

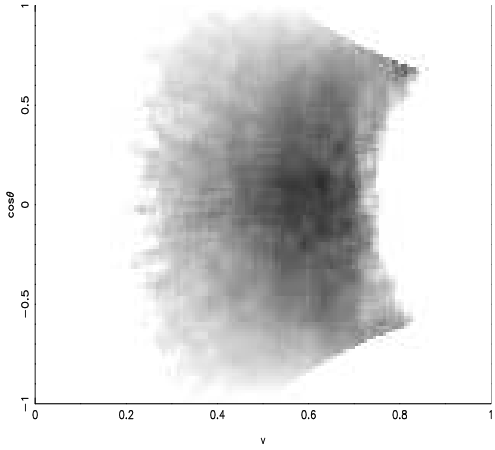

Figure 5.11: As Figure 5.10, for a subhalo of mass $10^8\ M_\odot$.

of the contribution. For example, it is possible that the contribution of $f(\mathbf{r}, \mathbf{v})$ in the three-dimensional $(\cos\theta, v)$ array is very low and therefore completely "obscured" by the "background " distribution produced by the Galactic halo. In fact, comparing carefully the four plots of Figure 5.12 to the $f(\mathbf{r}, \mathbf{v})$ of the "original" Milky Way-like halo (Figure 5.8), the weak contribution of M_3 can be noted. It is visible when we consider long evolution times, such as t_3 and t_4. In Figure 5.12d a black circle pinpoints the region corresponding to the presence of this contribution: it is populated by particles with high speed (400 km s$^{-1} \lesssim v \lesssim 460$ km s^{-1}) and angle $\theta \simeq 90°$.

The only case in which the merger of an extra progenitor generates clear features in the angle distribution of the Milky Way at redshift z_0 is when the mass of the subhalo is

Fig. 5.12a: $t_1 \simeq 1.75$ Gyr

Fig. 5.12b: $t_2 \simeq 2.0$ Gyr

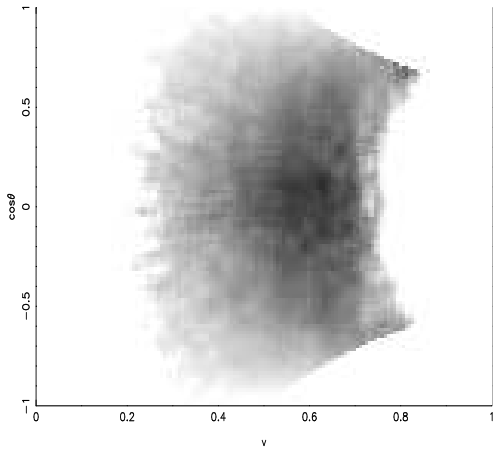

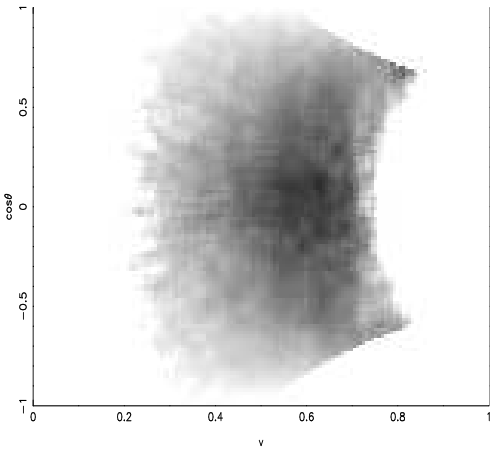

Fig. 5.12c: $t_3 \simeq 7.5$ Gyr

Fig. 5.12d: $t_4 \simeq 13$ Gyr

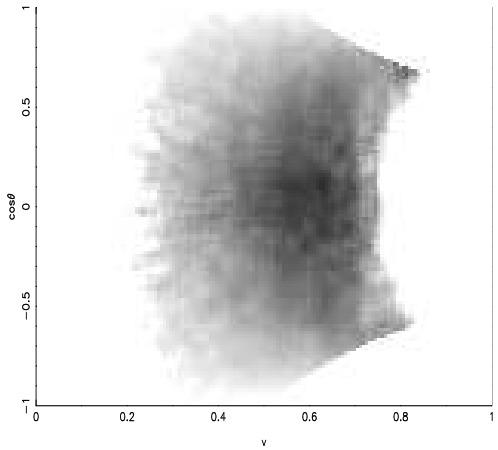

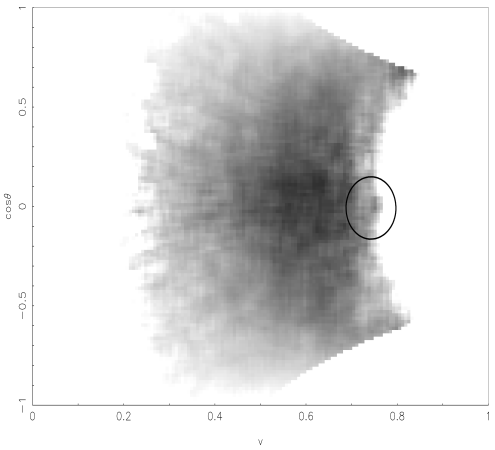

Figure 5.12: As Figure 5.10, for a subhalo of mass $10^9\, M_\odot$. The black circle identifies the region of the space where the contribution of the satellite is more relevant.

equal to $10^{10}\, M_\odot$. Looking at the four plots Figure 5.13 is composed of, it is possible to note the presence of relevant differences between every timestep and the "original" configuration, and also between one timestep and another. Figure 5.13a represents the fall of M_4 into the Galaxy approximately 1.75 Gyr ago. Two vertical, narrow stripes are clearly visible in the plot. They are localised in a small region of the angle distribution and they are associated with very precise values of the velocity: the first one to $v \simeq 400$ km s^{-1}, the second one to $v \simeq 430$ km s^{-1}. They both have an angular width of approximately $15° - 20°$: the first is not well defined, not allowing a precise measurement of its borders, while the second is more defined and it is centred in the range $79° \lesssim \theta \lesssim 96°$. This means that their direction is nearly perpendicular the

motion of the Sun in the Milky Way.

The features are localised in a small region of the parameter space because t_1 was chosen to match one of the first passages of the subhalo through the detector position. At this early stage of its evolution, the satellite does not have sufficient time to get significantly disrupted by the gravitational field of the host system. Nevertheless, the presence of the two stripes shows that the subhalo is beginning to get stripped and that streams start to form. The angular spread of the features are accessible to ongoing experiments (we have already seen that the current angular resolution is $\simeq 10^{\circ}$), raising the possibility to detect these peculiar features. This possibility obviously depends on the probabilities of finding the remnant of a $10^{10}\, M_{\odot}$ subhalo in the Solar neighbourhood and that this subhalo merged into the Galactic halo in the very recent past.

We can be sure that the two stripes are generated by the merger of M_4 firstly because they are completely absent in Figure 5.8, that represents the velocity distribution of the "original" Milky Way-like halo. A second, indirect confirmation of their origin comes from the comparison between the velocity distribution at t_1 and Figure 5.13b, in which $f(\mathbf{r}, \mathbf{v})$ is calculated at t_2. At this timestep the two vertical stripes, that were evident at t_1, have almost completely disappeared. This behaviour is expected because t_2 describes the system in a phase of its evolution in which the main body of the satellite is not located anywhere nearby the location of the detector. The fact that the contribution of M_4 to the velocity distribution at t_2, which describes an early stage in the evolution history of the system, is negligible suggests that the subhalo is still coherent.

The timestep t_3 corresponds to a system in which M_4 fell into the Galactic halo approximately 7.5 Gyr ago, a time long enough to perform several orbits around the Galactic centre. This scenario is represented in Figure 5.13c. At each orbit the amount of streams and debris into which the subhalo is disrupted increases, due to the phase mixing that acts on the satellite. An increase of the number of streams in the space translates in an increase of the stripes in the plot $(v, \cos\theta)$. Each of them is characterised by a similar, but slightly different, value of the velocity, which is related to the orbit performed by the stream. If the number of stripes is large, as in this case, they

Fig. 5.13a: $t_1 \simeq 1.75$ Gyr

Fig. 5.13b: $t_2 \simeq 2.0$ Gyr

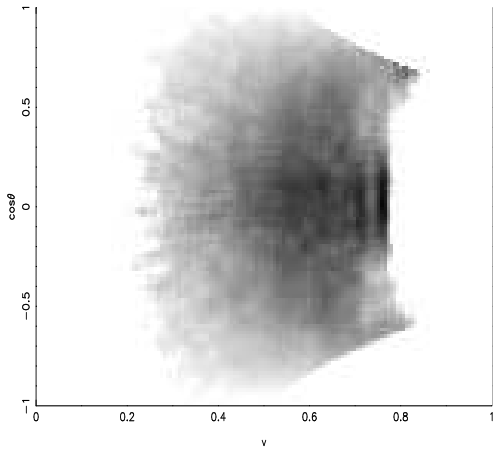

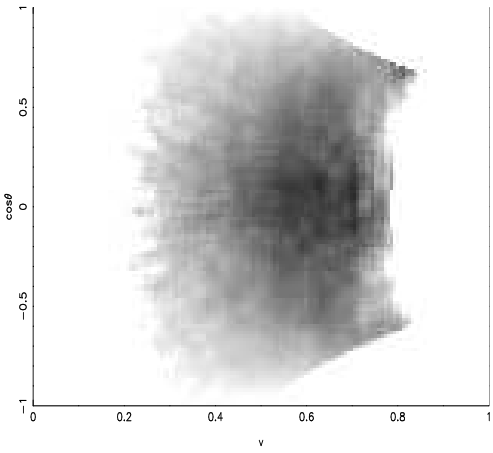

Fig. 5.13c: $t_3 \simeq 7.5$ Gyr

Fig. 5.13d: $t_4 \simeq 13$ Gyr

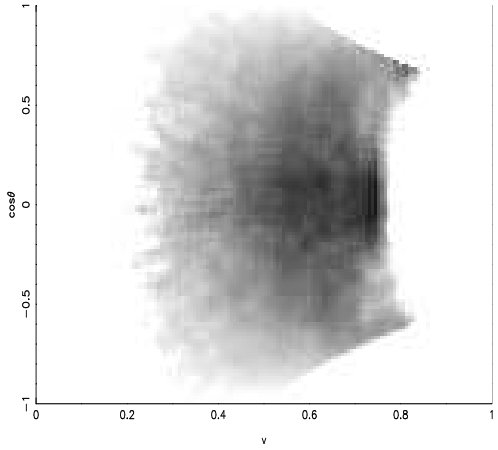

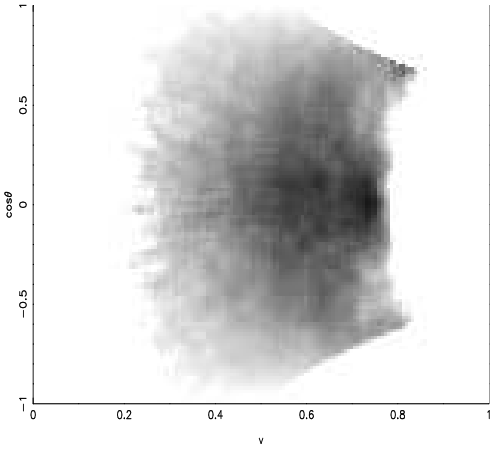

Figure 5.13: As Figure 5.10, for a subhalo of mass $10^{10}\,M_{\odot}$.

overlap and the velocity distribution of the subhalo starts to become smooth and uniform. Nevertheless, the presence of a vertical stripe at velocity $\simeq 430$ km s^{-1} and with an angular spread of $\simeq 20°$, with the angle centred in the range $79° \lesssim \cos\theta \lesssim 96°$, can be interpreted as the trace left by a dense, massive stream composed by particles originally part of M_4. Another possibility is that the stripe indicates the passage of the central region of the satellite. Both these interpretations suggest that the disruption of M_4 is not complete. If the stripe is generated by the core of the satellite, it also implies that this region is still compact and dense.

Figure 5.13d presents the same quantity for the configuration in which the merger of M_4 happened 13 Gyr ago. We can see that at z_0 the stripes are completely washed

out. This is interpreted as the superimposition of a very large number of streams which overlap and form an almost homogeneous distribution. Nevertheless, it is possible to identify an overdensity: it is located in the speed range 400 km s$^{-1} \lesssim v \lesssim 430$ km s^{-1}, and it has an angular width of about $\simeq 5^\circ$, in the range $87^\circ \lesssim \theta \lesssim 92^\circ$. The presence of this overdensity suggests that the progenitor M_4 is not completely disrupted even after an evolution time of 13 Gyr. It has been stripped and distorted by the gravitational field of the Galaxy, but the remnant of the central part of the satellite is not completely disrupted and it still shows up in the observable $(\cos\theta, v)$ space as an overdensity. The probability of detecting such a phenomenon with ongoing experiments is however low, due to the lack of strong features, together with the inadequate angular resolution of the current generation of instruments.

To summarise, this discussion leads to a main conclusion: only the merger of a $10^{10}\, M_\odot$ subhalo generates significant features in the ultra-local velocity distribution. The angular width of these features is larger than 10°, a resolution accessible to ongoing experiments. On the other hand, the contribution to the velocity distribution of the Milky Way produced by satellites with a mass in the range between $10^7\, M_\odot$ and $10^9\, M_\odot$ is completely undetectable. This is due to the presence of the velocity distribution of the Milky Way halo, which "obscures" that produced by the new progenitors.

5.3.2 Contribution of the subhalos to the global velocity distribution

The results of Section 5.3.1 have shown that only the most massive satellite M_4 generates features that are visible in the angle distribution of a Milky Way-like halo. Nevertheless, this fact does not imply that the contributions of M_1, M_2 and M_3 are completely negligible. As already explained above, it is possible that the contribution of these three subhalos is partially or totally "covered" by the velocity distribution of the Milky Way-like halo. To investigate this point we need to isolate the velocity distribution of the additional progenitors defined above from the one of the host halo. We do this by subtracting $f(\mathbf{r}, \mathbf{v})$ of the Milky Way-like halo from each of the systems composed by the Milky Way-like halo plus one of the extra progenitors considered in Section 5.3. The contributions produced by the subhalos M_3 and M_4 in the space

$(\cos\theta, v)$ are presented in Figures 5.14 - 5.15. As in Section 5.3.1, every figure is composed of four plots, which describe $f(\mathbf{r}, \mathbf{v})$ at the timesteps t_1, t_2, t_3 and t_4. They correspond to infall times of about 1.75 Gyr, 2.0 Gyr, 7.5 Gyr and 14 Gyr ago. The limits of the grey-scale of the plot are the same of the previous figures, covering six orders of magnitude in the value of the distribution function. We also investigate the velocity distributions of M_1 and M_2, but they are not plotted because none of them shows visible fine-grained features. This absence can be easily explained: at each timestep the velocity-space distribution of the system varies, but it is "invisible" because it is below the resolution limit. We can thus conclude that the contribution of a single satellite with mass smaller or equal to $10^8\, M_\odot$ is negligible.

The four plots of Figure 5.14 show that M_3 provides a non-negligible contribution to the ultra-local velocity distribution of the Milky Way-like halo. The fall into the Milky Way-like halo of a subhalo of mass $10^9\, M_\odot$ approximately 1.75 Gyr ago generates a singe stripe in the space $(\cos\theta, v)$. It has a speed $v \simeq 430$ km s^{-1} and it is centred in the range $79° \lesssim \theta \lesssim 93°$. As already explained in Section 5.3, t_1 represents the passage of the system through the detector position, and the stripe is the signature produced by the presence of the subhalo, that is still coherent, at the detector position. Observing Figure 5.14a it is possible to note that the contribution of M_3 at t_1, even if present, is too low for being visible in the final velocity distribution of the system composed by the Milky Way-like halo and M_3.

Figure 5.14b shows the contribution of M_3 at t_2, a time at which the satellite is not passing through the Solar neighbourhood. The lack of features suggests that M_3 is still coherent and it has not been severely stripped by the gravitational field of the Milky Way. Its streams are not passing through the detector at this timestep, consequently $f(\mathbf{r}, \mathbf{v})$ is null.

Figure 5.14c displays the velocity distribution of M_3 in the case in which it merged into the host halo 7.5 Gyr ago. The plot shows an overdensity located in the speed range 400 km s$^{-1} \lesssim v \lesssim 430$ km s^{-1}. Its angular width is $\simeq 20°$, in the range $80° \lesssim \theta \lesssim 100°$. This overdensity seems to be composed of a small number of overlapping stripes and is located in the same region in which the contribution of the subhalo M_3 to final velocity distribution was identified by a black circle in Figure 5.13c.

Fig. 5.14a: $t_1 \simeq 1.75$ Gyr

Fig. 5.14b: $t_2 \simeq 2.0$ Gyr

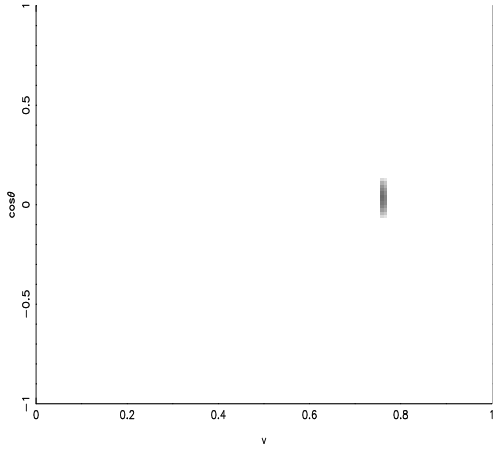

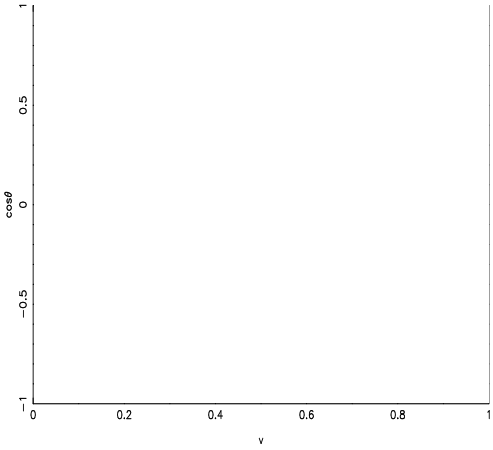

Fig. 5.14c: $t_3 \simeq 7.5$ Gyr

Fig. 5.14d: $t_4 \simeq 13$ Gyr

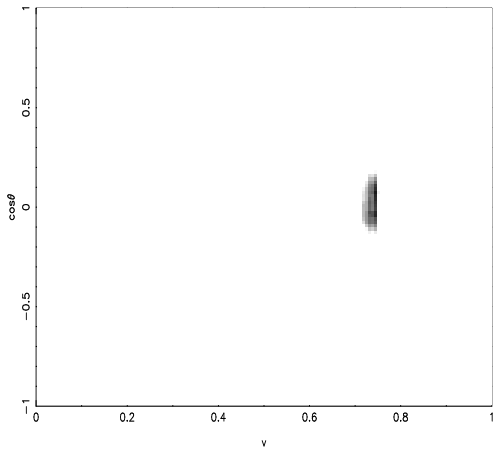

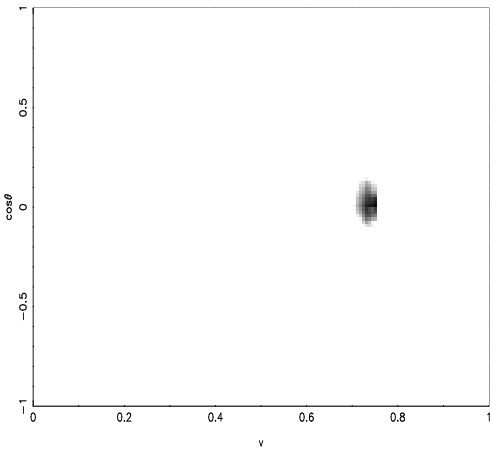

Figure 5.14: Contribution of the satellite M_3 ($= 10^9\, M_\odot$) to the velocity distribution of the Galactic halo at redshift z_0. The four plots describe configurations in which the progenitor falls into the host halo at different times: $\simeq 1.75$ Gyr ago (Figure 5.14a), $\simeq 2.0$ Gyr (Figure 5.14b), $\simeq 7.5$ Gyr (Figure 5.14c) and $\simeq 13$ Gyr (Figure 5.14d). The four plots have constant spread ($n_v = 150$, $n_\theta = 120$) and are smoothed using the "refined" boxcar technique described in Section 5.2.2, selecting a (5×5)box. The dimension of a pixel on the x-axis is $\simeq 3.8$ km s^{-1}, while the angular resolution on the y-axis varies between $10^\circ\, 30'$ (for small angles) and $\simeq 1^\circ$ (for large angles). One velocity-unit corresponds to 570 km s^{-1}.

Finally, the adoption of the timestep t_4 (Figure 5.14d) does not produce any major variation in the velocity distribution of M_3, compared to the situation at t_3. The angle distribution of the satellite is still localised in the same small region of the space $(\cos\theta, v)$ and it still does not appear smooth and homogeneous. This suggests that the disruption process is still ongoing after an evolution time of 13 Gyr.

Concerning the satellite M_4, its evolution is very similar to that of M_3, confirming the analysis already discussed in Section 5.3.1. The plots of Figure 5.15 highlight the presence of stripes when the subhalo falls in the Galactic halo at the timestep t_1. When longer timesteps are considered, such as t_3 and t_4, these features overlap and start to generate a uniform velocity distribution. The reason why the contribution of M_4 to the ultra-local velocity distribution is smoother than that one of M_3 is due to the properties of the two progenitors. As explained in Section 3.2, the initial spatial extent of the subhalo, identified with the quantity σ_s, and its initial velocity dispersion σ_v are related to the mass of the system. The relations between these three quantities are expressed in Equation (3.1). An increase of the mass of the progenitor generates an increase in the values of these two quantities, making M_4 less concentrated and "hotter" than M_3. These changes in the internal properties of the subhalo lead to a decrease in the time necessary to disrupt the system and an increase in the number of streams present at a certain time.

Finally it is interesting to compare the velocity distribution of M_4 to the results presented in Section 5.1.1. Figures 5.1c - 5.1d describe the velocity distribution of M_4 as a function of the speed and of $\cos\theta$ after evolution times $t \simeq 1.4$ Gyr and $t \simeq 13.6$ Gyr. They are simulated using the same version of the model used in this section, but selecting a set of arbitrary initial conditions rather than using the more realistic ones provided by a merger tree. The two plots can be compared to the simulations performed at t_1 and t_4 because these two timesteps are similar to the evolution times considered above. The comparison between Figure 5.1c and Figure 5.15b highlights a underestimation of $f(\mathbf{r}, \mathbf{v})$ when the initial conditions of the satellite are arbitrarily fixed. This is demonstrated by the fact that the stripes in Figure 5.1c are less remarkable than in Figure 5.15b. For a longer evolution, represented respectively by $\simeq 13.6$ Gyr and t_4, the differences between the two velocity distributions tend to disappear, as

it is possible to see comparing Figure 5.1d and Figure 5.15d. From these two comparisons it is possible to conclude that the use of the merger tree for the merger history of a Milky Way-like halo improves the precision of the results.

Fig. 5.15a: $t_1 \simeq 1.75$ Gyr

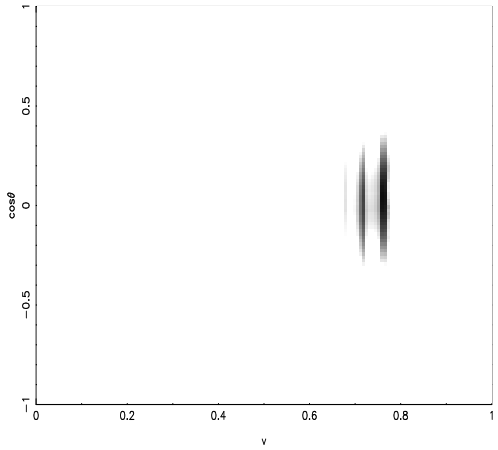

Fig. 5.15b: $t_2 \simeq 2.0$ Gyr

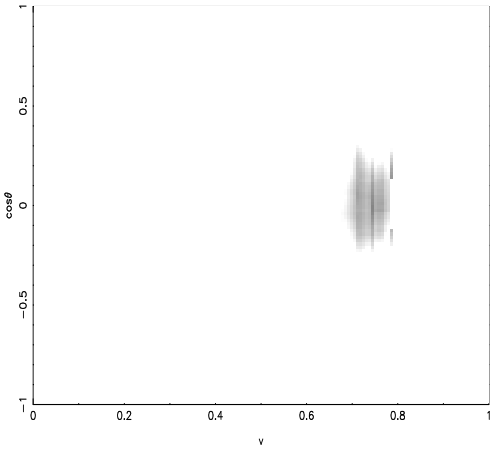

Fig. 5.15c: $t_3 \simeq 7.5$ Gyr

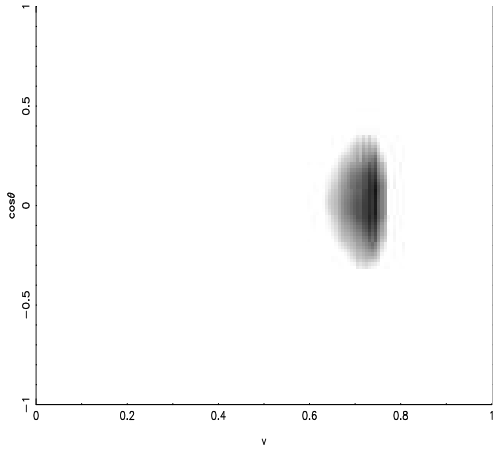

Fig. 5.15d: $t_4 \simeq 13$ Gyr

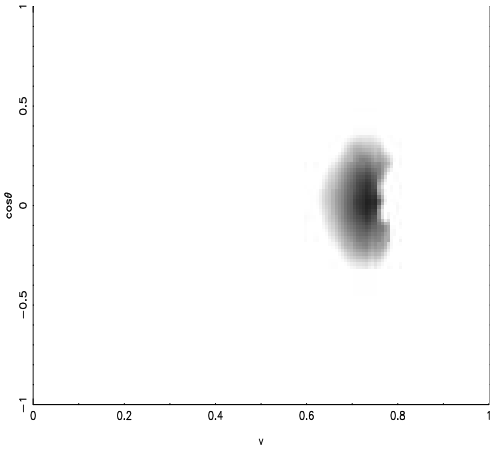

Figure 5.15: As Figure 5.14, for a subhalo of mass $M_4 = 10^{10}\, M_\odot$

Chapter 6

Summary

Very recently, large simulations of the formation of Milky Way-like dark matter halos have made predictions on the amount of substructure present at the Solar position, and on their contribution to the local dark matter distribution down to a resolution of 100 pc (Stadel et al. 2009, Diemand et al. 2008, Springel et al. 2008). They have resolved a incredibly large number of substructures, both gravitationally bound (halos) and unbound (streams). Unfortunately, they cannot resolve the ultra-fine dark matter distribution on scales relevant for terrestrial instruments. These scales are of the order of one tenth of a milliparsec, so six orders of magnitude smaller than 100 pc. To solve this problem alternative approaches have to be designed.

In this project, we have developed a model which allows us to quickly calculate the velocity distribution resulting from the merger of a unbound system of particles with a parent galaxy at a single point in space. For our purpose this single point was associated with a detector in the Solar neighbourhood. Using this model the velocity distribution can be calculated at arbitrarily high spatial resolution at any time during the evolution of the system. Once the present-day detector spatial location $\mathbf{x}$, and a velocity $\mathbf{v}$ of interest are defined, the method consists of analytically evolving these phase-space coordinates backward-in-time to determine their initial location.

We can then calculate the amount of material in a merging satellite that originated from these initial phase-space coordinates, and hence will end up at the selected velocity in a terrestrial detector today. As a result, we can map out the present-day phase-space

structure of the disrupted merging satellite on an ultra-fine spatial scale, obtaining qualitative but useful insights into the likely signature of a halo merger in a small terrestrial dark matter detector. Unlike a conventional N-body approach, the gravitational force does not have to be artificially softened, and the phase-space can be explored rapidly and accurately, without the computational overhead of numerical integration. The parent galaxy is described by an isochrone potential (Hénon 1959) because this is one of the few forms of potential that allows the calculation of analytic expressions for the angular frequencies. This property allows the very rapid ultra-high-resolution calculations performed here. The initial phase-space distribution of the merging halo is represented by a bivariate Gaussian (Evans et al. 2000, Helmi et al. 2002), which is also simplified but has both spatial and velocity scales that can be tuned to match the properties of the real halos.

In this model the dynamics of the merger can be calculated remarkably simply, and the satellite can be evolved analytically forwards or backwards in time. By scanning the velocity-space, we can map out the sub-mpc-scale structure of the Milky Way's halo and obtain unique insights into the likely signature of a halo merger event in a small terrestrial dark matter detector. As such, this study is complementary to others, in that it uses a less realistic potential but has a unprecedentedly high resolution.

The velocity-space distribution function is characterised by discrete peaks, even at late times (up to 13.6 Gyr), when the particles are distributed almost homogeneously through phase-space. As a diagnostic for dark matter directional detection we have studied the angle at which particles impinge on the detector, measured relative to the direction of Solar motion in the Milky Way. In agreement with Stiff & Widrow (2003) we have found that this diagnostic contains significant structures imprinted by the original merging sub-halo (Figure 3.11). Stiff & Widrow used a more realistic Milky Way potential but only integrated the orbits very approximately, while we have used a more approximate potential but treated the integration exactly, so the agreement of the two techniques suggests that the results are fairly robust.

When applied in a cosmological context, this method becomes a powerful instrument to calculate the velocity distribution in the Solar neighbourhood. We have combined a merger tree, which describes the hierarchical growth of a Milky Way-like halo, with

the model described in Chapter 2. This allowed us to produce a complete and more realistic treatment of the merger history of the Galactic halo. After assigning the initial conditions, the model calculates the velocity distribution for each branch of the tree, adds up all the contributions and calculates the final phase-space distribution in the Solar neighbourhood. The new version of the method can be applied to any merger tree but, being interested in the formation of a Milky Way-like system, we have selected a halo with a history broadly resembling that of our galaxy.

A second observable quantity is the energy spectrum of the system, which describes the energy distribution of the particles composing the system. In Figure 5.2 it is possible to infer the presence of a number of peaks, which are caused by the passage through the detector's location of the main body of the satellite. To highlight these small bumps we introduced a second diagnostic quantity: the fractional departure of the system from a smooth distribution. It is defined as the estimate (as a function) of how much the square of the velocity of a system differs from the smooth distribution, obtained when the satellite is almost completely relaxed. We have calculated it for the merger of two systems of mass $10^8 M_\odot$ and $10^{10} M_\odot$, considering a time $t \sim 1400$ Gyr when the subhalo is expected to be relaxed and smooth. In an early stage of the evolution ($t \simeq 1.4\,$Gyr) the fractional departure of both systems presents clear peaks (Figure 5.3), that are 10% to 20% larger than the deviation produced by the system in its relaxed configuration. Each peak represents the passage of a stream of particles and the detection of these features could help to shed light on the evolutionary history of the satellite. After $13.6\,$Gyr the features are almost indiscernible from the smooth configuration, suggesting that the mixing process is almost complete.

The velocity distribution of a Milky Way-like halo does not present any clear features (Figure 5.7). Nevertheless some overdensities appear. These overdensities are mostly produced by progenitors with mass $\simeq 10^{10} M_\odot$. The contribution of $\simeq 10^9 M_\odot$ objects is completely smooth, while most of the particles which compose progenitors with mass of $\simeq 10^8 M_\odot$ are moving with speed in the range 285 km s$^{-1} \lesssim v \lesssim 400$ km s^{-1}. These progenitors are less massive, but their number is large and consequently their contribution is not negligible. Thus, we can conclude that multiple mergers complicate the net angle distribution. Nevertheless, a few structures persist, raising the possibility

of disentangling at least the recent sub-halo merger history. This can be achieved by using directional detectors with angle and velocity resolution of $\simeq 1^\circ$ and 3.8 km s^{-1} respectively. Unfortunately at the current instrumental angle resolution, which is $\simeq 10^\circ$ (Dujmic et al. 2008, Ahlen et al. 2010), all the overdensities are washed away.

The analysis of the fractional departure of the Galactic halo form a smooth distribution (Figure 5.9) shows that it is indiscernible from a smooth distribution, leading to the conclusion that the ultra-fine dark matter distribution in the Solar neighbourhood is composed of a huge number of streams. These overdense structures overlap, generating a uniform and smooth velocity distribution. Figure 5.9 shows clearly that it is not possible to discern the presence of these structures using this particular quantity. The result is in agreement with recent work by Vogelsberger & White (2010).

We have also added an additional dark matter satellite to the Galactic halo, assuming that at the time given by the merger tree the subhalos are already in the centre of the Galaxy. A summary of the results is shown in Table 5.1. Only the addiction of a massive $10^{10}\,M_\odot$ subhalo to the Galactic halo has a visible impact on the angle distribution and on the direction from which the particles enter the detector. The angular dimension of these features is larger than 10°, which is the resolution limit of ongoing experiments, so it would be detectable. On the other hand, the contribution to the velocity distribution of the Milky Way produced by individual satellites with a mass in the range between $10^7\,M_\odot$ and $10^9\,M_\odot$ is negligible. This is due to the presence of the velocity distribution of the host halo, which "obscures" that produced by the new progenitors. Nevertheless, the final velocity distribution has overdensities for all the cases that has been analysed. These overdensities have been studied in Section 5.2.1, reaching the conclusion that they are generated by a very large number of merger events and that the current generation of detectors does not have the angular resolution required to observe these features. However, a future generation of detectors with a resolution of $\sim 1^\circ$ would start to resolve these features, allowing the merger history of the Milky Way to begin to be unravelled using this diagnostic

Bibliography

Ahlen S., et al., 2010. *International Journal of Modern Physics A*, **25**, 1.

Begeman K. G., Broeils A. H., Sanders R. H., 1991. MNRAS, **249**, 523.

Benson A. J., 2005a. MNRAS, **358**, 551.

Benson A. J., 2005b. MNRAS, **364**, 1104.

Bergström L., Hooper D., 2006. Phys. Rev. D, **73(6)**, 063510.

Bergström L., Ullio P., Buckley J. H., 1998. *Astroparticle Physics*, **9**, 137.

Bernabei R., Belli P., Cappella F., Cerulli R., Dai C. J., D'Angelo A., He H. L., Incicchitti A., Kuang H. H., Ma J. M., Montecchia F., Nozzoli F., Prosperi D., Sheng X. D., Ye Z. P., 2008. *European Physical Journal C*.

Bertone G., Hooper D., Silk J., 2005. Phys. Rep., **405**, 279.

Binney J., Tremaine S., 2008. *Galactic Dynamics: Second Edition*, Princeton University Press.

Bosma A., 1981. AJ, **86**, 1791.

Boylan-Kolchin M., Springel V., White S. D. M., Jenkins A., Lemson G., 2009. MNRAS, **398**, 1150.

Bryan G. L., Norman M. L., 1998. ApJ, **495**, 80.

Bullock J. S., Kolatt T. S., Sigad Y., Somerville R. S., Kravtsov A. V., Klypin A. A., Primack J. R., Dekel A., 2001. MNRAS, **321**, 559.

Burles S., Tytler D., 1998. ApJ, **499**, 699.

Cenarro A. J., Trujillo I., 2009. ApJ, **696**, L43.

Clowe D., Bradač M., Gonzalez A. H., Markevitch M., Randall S. W., Jones C., Zaritsky D., 2006. ApJ, **648**, L109.

Clowe D., Gonzalez A., Markevitch M., 2004. ApJ, **604**, 596.

Cole S., Aragon-Salamanca A., Frenk C. S., Navarro J. F., Zepf S. E., 1994. MNRAS, **271**, 781.

Cole S., Lacey C. G., Baugh C. M., Frenk C. S., 2000. MNRAS, **319**, 168.

Colless M., Dalton G., Maddox S., Sutherland W., Norberg P., Cole S., Bland-Hawthorn J., Bridges T., Cannon R., Collins C., Couch W., Cross N., Deeley K., De Propris R., Driver S. P., Efstathiou G., Ellis R. S., Frenk C. S., Glazebrook K., Jackson C., Lahav O., Lewis I., Lumsden S., Madgwick D., Peacock J. A., Peterson B. A., Price I., Seaborne M., Taylor K., 2001. MNRAS, **328**, 1039.

Cowsik R., McClelland J., 1973. ApJ, **180**, 7.

D'Amico G., Kamionkowski M., Sigurdson K., 2009. *ArXiv e-prints, 0907.1912*.

Diemand J., Kuhlen M., Madau P., Zemp M., Moore B., Potter D., Stadel J., 2008. Nature, **454**, 735.

Diemand J., Kuhlen M., Madau P., 2007. ApJ, **657**, 262.

Dodelson S., 2003. *Modern cosmology*.

Drukier A. K., Freese K., Spergel D. N., 1986. Phys. Rev. D, **33**, 3495.

Dujmic D., Fisher P., Sciolla G., Ahlen S., Dutta V., Henderson S., Kaboth A., Kohse G., Lanza R., Monroe J., Roccaro A., Skvorodnev N., Tomita H., Vanderspek R., Wellenstein H., Yamamoto R., 2008. *Astroparticle Physics*, **30**, 58.

Einasto J., Kaasik A., Saar E., 1974. Nature, **250**, 309.

Ellis J., Flores R. A., Lewin J. D., 1988. *Physics Letters B*, **212**, 375.

Evans N. W., Carollo C. M., de Zeeuw P. T., 2000. MNRAS, **318**, 1131.

Evans N. W., Ferrer F., Sarkar S., 2004. Phys. Rev. D, **69(12)**, 123501.

Fantin D. S. M., Merrifield M. R., Green A. M., 2008. MNRAS, **390**, 1055.

Fields B., Sarkar S., 2006. *Review of Particle Physics*, **33**, 1.

Freeman K. C., 1970. ApJ, **160**, 811.

Freese K., Frieman J., Gould A., 1988. Phys. Rev. D, **37**, 3388.

Freese K., Gondolo P., Stodolsky L., 2001. Phys. Rev. D, **64(12)**, 123502.

Frenk C. S., White S. D. M., Efstathiou G., Davis M., 1985. Nature, **317**, 595.

Gelmini G., Gondolo P., 2001. Phys. Rev. D, **64(2)**, 023504.

Gerhard O. E., Saha P., 1991. MNRAS, **251**, 449.

Ghigna S., Moore B., Governato F., Lake G., Quinn T., Stadel J., 1998. MNRAS, **300**, 146.

Ghigna S., Moore B., Governato F., Lake G., Quinn T., Stadel J., 1999. In: *Observational Cosmology: The Development of Galaxy Systems*, p. 140, ed. G. Giuricin, M. Mezzetti, & P. Salucci.

Goodman M. W., Witten E., 1985. Phys. Rev. D, **31**, 3059.

Green A. M., Morgan B., 2010. Phys. Rev. D, **81(6)**, 061301.

Green A. M., Hofmann S., Schwarz D. J., 2004. MNRAS, **353**, L23.

Groenewegen M. A. T., Blommaert J. A. D. L., 2005. A&A, **443**, 143.

Groenewegen M. A. T., Udalski A., Bono G., 2008. A&A, **481**, 441.

Helmi A., White S. D., Springel V., 2002. Phys. Rev. D, **66(6)**, 063502.

Henon M., 1959. *Annales d'Astrophysique*, **22**, 126.

Hénon M., 1969. A&A, **2**, 151.

Jungman G., Kamionkowski M., Griest K., 1996. Phys. Rep., **267**, 195.

Kamionkowski M., Turner M. S., 1991. Phys. Rev. D, **43**, 1774.

Kauffmann G., White S. D. M., Guiderdoni B., 1993. MNRAS, **264**, 201.

Kerr F. J., Lynden-Bell D., 1986. MNRAS, **221**.

Klypin A., Kravtsov A. V., Valenzuela O., Prada F., 1999. ApJ, **522**, 82.

Kolb E. W., Turner M. S., 1990. S&T, **80**, 381.

Komatsu E., Dunkley J., Nolta M. R., Bennett C. L., Gold B., Hinshaw G., Jarosik N., Larson D., Limon M., Page L., Spergel D. N., Halpern M., Hill R. S., Kogut A., Meyer S. S., Tucker G. S., Weiland J. L., Wollack E., Wright E. L., 2009. ApJS, **180**, 330.

Komatsu E., Smith K. M., Dunkley J., Bennett C. L., Gold B., Hinshaw G., Jarosik N., Larson D., Nolta M. R., Page L., Spergel D. N., Halpern M., Hill R. S., Kogut A., Limon M., Meyer S. S., Odegard N., Tucker G. S., Weiland J. L., Wollack E., Wright E. L., 2010. *ArXiv e-prints*, *1001.4538*.

Krauss L. M., Srednicki M., Wilczek F., 1986. Phys. Rev. D, **33**, 2079.

Lacey C., Cole S., 1993. MNRAS, **262**, 627.

Larson D., Dunkley J., Hinshaw G., Komatsu E., Nolta M. R., Bennett C. L., Gold B., Halpern M., Hill R. S., Jarosik N., Kogut A., Limon M., Meyer S. S., Odegard N., Page L., Smith K. M., Spergel D. N., Tucker G. S., Weiland J. L., Wollack E., Wright E. L., 2010. *ArXiv e-prints*, *1001.4635*.

Lemaître G., 1931. MNRAS, **91**, 490.

Lewin J. D., Smith P. F., 1996. *Astroparticle Physics*, **6**, 87.

McGill C., Binney J., 1990. MNRAS, **244**, 634.

Milgrom M., 1983. ApJ, **270**, 365.

Moore B., Calcáneo-Roldán C., Stadel J., Quinn T., Lake G., Ghigna S., Governato F., 2001. Phys. Rev. D, **64(6)**, 063508.

Morgan B., Green A. M., Spooner N. J., 2005. Phys. Rev. D, **71(10)**, 103507.

Nishiyama S., Nagata T., Sato S., Kato D., Nagayama T., Kusakabe N., Matsunaga N., Naoi T., Sugitani K., Tamura M., 2006. ApJ, **647**, 1093.

Olive K. A., Steigman G., Walker T. P., 2000. Phys. Rep., **333**, 389.

Oort J. H., 1932. Bull. Astron. Inst. Netherlands, **6**, 249.

Oort J. H., 1940. ApJ, **91**, 273.

Ostriker J. P., Peebles P. J. E., 1973. ApJ, **186**, 467.

Parkinson H., Cole S., Helly J., 2008. MNRAS, **383**, 557.

Peñarrubia J., McConnachie A. W., Navarro J. F., 2008. ApJ, **672**, 904.

Pease F. G., 1918. *Proceedings of the National Academy of Science*, **4**, 21.

Peebles P. J. E., 1982. ApJ, **263**, L1.

Read J. I., Wilkinson M. I., Evans N. W., Gilmore G., Kleyna J. T., 2006. MNRAS, **367**, 387.

Rogstad D. H., Shostak G. S., 1972. ApJ, **176**, 315.

Rubin V. C., Ford, Jr. W. K., 1970. ApJ, **159**, 379.

Rubin V. C., Ford, Jr. W. K., Thonnard N., Burstein D., 1982. ApJ, **261**, 439.

Rubin V. C., Burstein D., Ford, Jr. W. K., Thonnard N., 1985. ApJ, **289**, 81.

Rubin V. C., Ford W. K. J., . Thonnard N., 1980. ApJ, **238**, 471.

Rubin V. C., Thonnard N., Ford, Jr. W. K., 1978. ApJ, **225**, L107.

Sandick P., 2010. *ASP conference proceedings of the "Frank N. Bash Symposium 2009: New Horizons in Astronomy", 18-20 Oct. 2009, eds. L. Stanford, ArXiv e-prints, 1001.0942*.

Schramm D. N., Turner M. S., 1998. *Reviews of Modern Physics*, **70**, 303.

Silk J., Srednicki M., 1984. *Physical Review Letters*, **53**, 624.

Slipher V. M., 1914. *Lowell Observatory Bulletin*, **2**, 66.

Smith M. C., Ruchti G. R., Helmi A., Wyse R. F. G., Fulbright J. P., Freeman K. C., Navarro J. F., Seabroke G. M., Steinmetz M., Williams M., Bienaymé O., Binney J., Bland-Hawthorn J., Dehnen W., Gibson B. K., Gilmore G., Grebel E. K., Munari U., Parker Q. A., Scholz R., Siebert A., Watson F. G., Zwitter T., 2007. MNRAS, **379**, 755.

Smith S., 1936. ApJ, **83**, 23.

Sofue Y., Honma M., Omodaka T., 2009. PASJ, **61**, 227.

Springel V., White S. D. M., Jenkins A., Frenk C. S., Yoshida N., Gao L., Navarro J., Thacker R., Croton D., Helly J., Peacock J. A., Cole S., Thomas P., Couchman H., Evrard A., Colberg J., Pearce F., 2005. Nature, **435**, 629.

Springel V., Wang J., Vogelsberger M., Ludlow A., Jenkins A., Helmi A., Navarro J. F., Frenk C. S., White S. D. M., 2008. MNRAS, **391**, 1685.

Srednicki M., Olive K. A., Silk J., 1987. *Nuclear Physics B*, **279**, 804.

Stadel J., Potter D., Moore B., Diemand J., Madau P., Zemp M., Kuhlen M., Quilis V., 2009. MNRAS, **398**, L21.

Stiff D., Widrow L. M., 2003. *Physical Review Letters*, **90(21)**, 211301.

Stiff D., Widrow L. M., Frieman J., 2001. Phys. Rev. D, **64(8)**, 083516.

Szalay A. S., Marx G., 1976. A&A, **49**, 437.

Tegmark, et al., 2006. Phys. Rev. D, **74(12)**, 123507.

Turner M. S., Wilczek F., 1990. Phys. Rev. D, **42**, 1001.

Tytler D., O'Meara J. M., Suzuki N., Lubin D., 2000. *Physica Scripta Volume T*, **85**, 12.

Vogelsberger M., White S. D. M., 2010. *ArXiv e-prints, 1002.3162*.

Vogelsberger M., White S. D. M., Helmi A., Springel V., 2008. MNRAS, **385**, 236.

Vogelsberger M., Helmi A., Springel V., White S. D. M., Wang J., Frenk C. S., Jenkins A., Ludlow A., Navarro J. F., 2009. MNRAS, **395**, 797.

Weber M., de Boer W., 2010. A&A, **509**, A25+.

White S. D. M., Frenk C. S., 1991. ApJ, **379**, 52.

Wright E. L., 2006. PASP, **118**, 1711.

Zemp M., Diemand J., Kuhlen M., Madau P., Moore B., Potter D., Stadel J., Widrow L., 2009. MNRAS, **394**, 641.

Zwicky F., 1933. *Helvetica Physica Acta*, **6**, 110.